Superconductivity Program for Electric Systems
Annual Progress Report for Fiscal Year 2003

Superconductivity Technology Center
Los Alamos National Laboratory

Dean E. Peterson, Center Director and Program Manager

Jeffrey O. Willis, Principal Team Leader and Editor

Contributors:

M. Archuleta	T.A. Jankowski	D.E. Peterson
P.N. Arendt	S. Hong[OST]	F.C. Prenger
S.P. Ashworth	Q.X. Jia	A. Razani[UNM]
A. Ayala	M. Johnson[NMSU]	J. Reeves[SP]
J.G. Bernard[DP]	J.A. Kennison	C. Rey[DP]
R.N. Bhattacharya[NREL]	S. Kreiskott	M. Rupich[AMSC]
L.E. Bronisz	D.C. Larbalestier[UW]	V. Selvamanickam[SP]
X. Cai[UW]	X.Z. Liao	A. Serquis
J. Campuzano[UIC]	Y. Li	C.J. Sheehan
L. Civale	Y. Lin	L. Stan
J.Y. Coulter	J.MacManus-Driscoll[UC]	J.A. Stewart
R.F. DePaula	B. Maiorov	P. te Riele
P.C. Dowden	M.P. Maley	I. Usov
A.T. Findikoglu	A. Malozemoff[AMSC]	J. Vasquez-Dominguez
S.R. Foltyn	K. Marken[OST]	H. Wang
J. Gallegos	V. Maroni[ANL]	J.A. Waynert
B.J. Gibbons	V. Matias	C.J. Wetteland
J.R. Groves	H.P. Miao[OST]	J.O. Willis
M.E. Hawley	M. Meinesz[OST]	R.M. Wingo
E.E. Hellstrom[UW]	F.M. Mueller	L.A. Worl
T.G. Holesinger	A. Otto[AMSC]	T.Y. Ying
Y. Huang[AMSC]	P.J. Pellegrino[SP]	Y.T. Zhu

Los Alamos
NATIONAL LABORATORY
— EST. 1943 —

The World's Greatest Science Protecting America

Table of Contents

Table of Figures

5

6

10

Glossary of Acronyms

ANL	Argonne National Laboratory
AMSC	American Superconductor Corporation
BEI	Backscatter Electron Imaging
Bi-2212	$Bi_2Sr_2CaCu_2O_8$
Bi-2223	$(Bi,Pb)_2Sr_2Ca_2Cu_3O_8$
BSCCO	Bi-2212 or Bi-2223
CRADA	Cooperative Research and Development Agreement
EBSD	Electron Back-Scattered Diffraction
EDS	Energy Dispersive Spectroscopy
FCC	Fault Current Controller
FCL	Fault Current Limiter
HGMS	High-Gradient Magnetic Separator
HTS	High-Temperature Superconductivity
IBAD	Ion Beam-Assisted Deposition
IMP	Isothermal Melt Processing
I_c	Critical current of a superconductor, A
J_c	Critical current density of a superconductor, A/cm^2
LANL	Los Alamos National Laboratory
LARP	Los Alamos Research Park
MgO	Magnesium Oxide
MRI	Magnetic Resonance Imaging
NHMFL	National High-Magnetic Field Laboratory
ORNL	Oak Ridge National Laboratory
OSTI	Oxford Superconductivity Technology, Inc.
PLD	Pulsed-Laser Deposition
PMC	Prototype Multi-Strand Cable
RBS	Rutherford Backscattering Spectroscopy
RHEED	Reflection High-Energy Electron Diffraction
SAD	Selected Area Diffraction
SCE	Southern California Edison
SEM	Scanning Electron Microscopy
Sm-123	$SmBa_2Cu_3O_{7-\delta}$
SPI	Superconductivity Partnerships with Industry
STC	Superconductivity Technology Center (Los Alamos)
T_c	Critical temperature for superconductivity, K
TEM	Transmission Electron Microscopy
XRD	X-Ray Diffraction
YBCO	$YBa_2Cu_3O_{7-\delta}$
YSZ	Yttria-Stabilized Zirconia

Introduction

The rate of progress towards practical applications of high temperature superconductors (HTS) continues to be very rapid. BSCCO tapes are now commercially available for use in the Superconductivity Partnership Initiative (SPI) projects and other prototype power demonstrations. Second-generation coated conductors continue to display very high critical currents in long lengths when cooled with liquid nitrogen indicative of the future potential for wide spread use in power applications. The SPI projects including the three transmission cable initiatives, fault current limiter, generator, flywheel, motor, MRI, magnetic separator, and transformer are all exciting. The national laboratories are proud to have played important roles in advancing these technical successes.

LANL continued to be a CRADA partner with American Superconductor in the Wire Development Group focused on advancing further improvement of properties of BSCCO tapes. All current SPI projects rely on production of Bi2223 tapes with superconducting properties appropriate for the application. Our contributions in tape processing combined with both microscopic and superconducting characterizations have been critical to continued technical advancements in this area.

LANL continued to demonstrate leadership in coated conductor development by achieving world records for the highest critical currents achieved at liquid nitrogen temperature. New, unique tape processing and characterization capabilities have been developed at the Research Park that are now available to other national labs, universities, and industrial collaborators.

LANL continued strong partnerships with Superpower and American Superconductor in second-generation wire development focusing on the IBAD MgO technology. These collaborations have been extremely beneficial in accelerating their progress towards commercialization of coated conductors. Our expertise in evaluating vortex pinning in superconductor tapes as a function of magnetic field and angle was shown to be very valuable. LANL contributions towards characterizing and minimizing ac losses in coated conductors have been substantial.

LANL continued in a strong partnership with General Electric focused on a 100 MVA HTS SPI generator. Another SPI partnership with DuPont involving a HTS magnetic separator demonstrated efficient separation. A SPI collaboration with Oxford directed towards a HTS MRI system demonstrated substantial progress.

Research and development activities at LANL related to the HTS program for FY03 are collected in this report. Technical highlights are listed in Section 1 and individual project summaries appear in Section 2. Section 3 lists the 45 journal articles and the 40 other publications and conference abstracts for the year. Section 4 summarizes the total patent and license activity, and Section 5 lists the various agreements completed or underway.

Dean E. Peterson, Leader
Superconductivity Technology Center

1. Highlights of Fiscal Year 2003

• *Alumina was determined to be a very effective cation diffusion barrier layer beneath the IBAD-MgO template layer.*
• *Yttria (Y_2O_3) was determined to be a good replacement for amorphous Si_3N_4 as the nucleation layer for IBAD MgO. A major advantage of yttria is that the best texture of the IBAD MgO is less sensitive to the thickness of that layer .*
• *Improvements in polishing and ion beam divergence reduced in plane texture FWHM by ~1.5º.*
• *Thick YBCO films on IBAD MgO are now of as high quality as those on single-crystal MgO.*
• *Thick films show a variation in microstructure with thickness by XRD and RBS. Both as deposited and ion milled films follow the same J_c vs. thickness dependence.*
• *Porosity problems found in YBCO on IBAD-YSZ are not present in films on IBAD-MgO, presumably because of the smoother surface of the latter.*
• *Thick film bridge samples typically have I_c > 300 A/cm width (best result: 720 A/cm, 4.5 μm, 1.6 MA/cm^2) at 75 K and self field.*
• *Continuously processed 1 cm wide, 10 cm long tapes were produced with I_cs of 265-319 A. Longer tapes (~70 cm) had I_cs of ~170 A.*
• *Contributions to the vortex pinning in PLD YBCO films on single crystal and IBAD MgO substrates have been identified. Random defects give rise to a smooth angular dependence with a J_c maximum at the ab plane. The c-axis peak in J_c is due to correlated extended defects, such as those at twin and grain boundaries. An additional sharp peak in J_c at the ab plane is due to intrinsic pinning and is always seen. Films on IBAD-MgO have higher J_c values over most of the angular range compared to those on single crystal substrates.*
• *Continuously processed electropolished substrates have been produced with surface finish <1 nm RMS in lengths over 100 m in the bipolar electropolishing system.*
• *Continuously processed IBAD-MgO has been produced in >5 m lengths at speeds to 36 m/h with typical in plane texture of 6-7º FWHM.*
• *Continuously processed YBCO conductors have been produced with short sample values of >170 A/cm and 50 A/cm in >1 m lengths. In plane texture of the YBCO is typically <3º FWHM.*
• *A continuous measurement system has measured the I_c of tapes to 2 m length with selectable step size down to 0.25 mm and in magnetic fields of 0.3 ~ 0.7 T to prevent sample damage from current heating.*
• *AC losses as a function of magnetic field amplitude, transport current amplitude, and relative phase have been obtained on coated conductors with both RABiTS-based and IBAD-MgO-based template layers. A method to reduce losses has been demonstrated for short samples and for conductors with a ferromagnetic layer.*
• *Bi-2212 intergrowths in Bi-2223 grains away from the silver interface and residual other phases in the filament cores are present early in the processing of Bi-2223 tapes and are present in even very high performance commercial tapes and those with an overpressure post*

anneal. The trapped Bi-2212 prevents complete reaction of the "excess" material.

• *LANL has provided GE with required data on outgassing and gettering of materials required for long-term vacuum maintenance of the 100 MVA HTS generator. LANL has also supplied a heat pipe concept for cooling the HTS rotor.*

• *High gradient magnetic separation has proven effective in laboratory scale experiments for cleaning heavy metals from mine drainage. The metals are first synthesized into a ferrite. This can then be magnetically separated and finally discarded as a nonhazardous, stable compound.*

• *Bi-2212 conductors for a HTS MRI system magnet have been characterized microstructurally and electrically to develop design data for a prototype system.*

• *Thirty journal articles were published, fifteen others were submitted for publication, and more than 40 other non journal or conference abstracts were submitted during the year.*

• *Twelve patent disclosures and filings were made and five patents were issued during the year.*

• *One CRADA agreement was renewed during the year.*

2. Technical Activities

2.1 Wire Technology

2.1.1 MgO template development for coated conductors using ion beam assisted deposition

P.N. Arendt, S.R. Foltyn, R. DePaula, J.R. Groves, T.G. Holesinger, Q.X. Jia, S. Kreiskott, V. Matias, L. Stan, I. Usov, and H. Wang

A. Substrate cation diffusion barrier

The thickness, and therefore time, requirements to produce a high quality template film of YSZ by ion beam assisted deposition (IBAD), first led our program to investigate IBAD MgO. The rate-limiting step for the development of a template layer for YBCO coated conductor deposition is dominated by the IBAD process. For YSZ, a typical IBAD layer thickness is 610 nm, but for MgO, it is only 10 nm; this represents a nearly 2 orders of magnitude improvement in this step. The other layers in the sequence, shown in TEM images in Fig. 1, provide chemical barriers, lattice matching, and other functions. Changing to IBAD MgO has allowed a reduction in this stack thickness from 650 nm down to 155 nm.
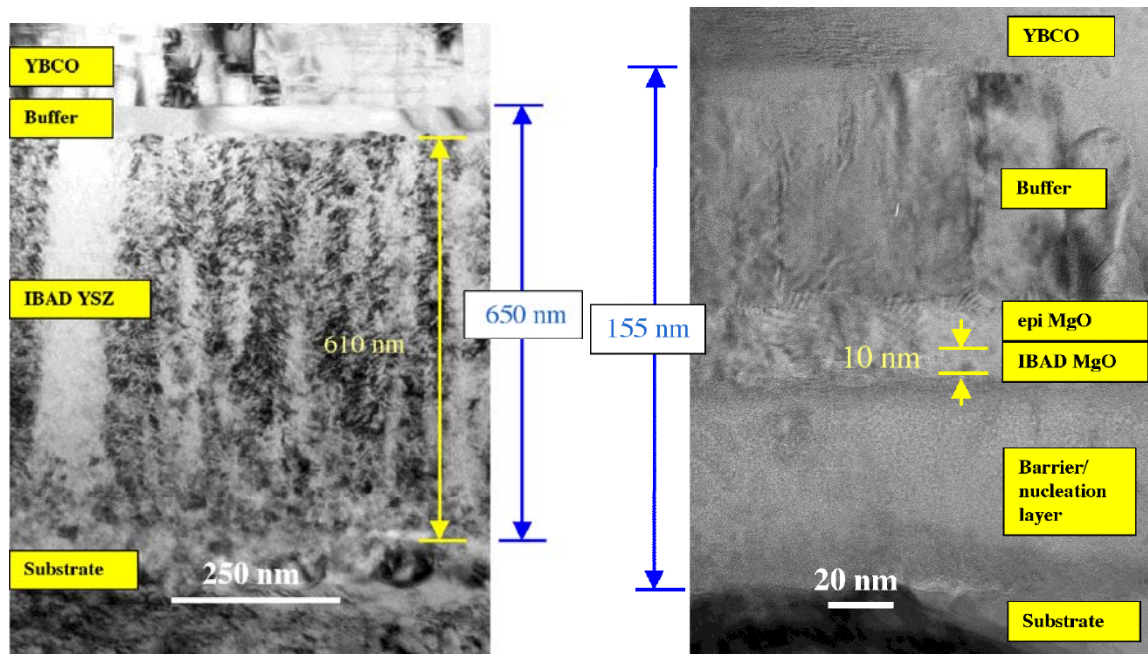
Fig. 1. TEM images comparing the stacking sequence of the template and buffer layers for IBAD YSZ (left) and IBAD MgO (right).

A barrier layer beneath the MgO layer is very important to prevent diffusion of cations from the substrate into the YBCO layer and poisoning that material. Fig. 2a shows an example stacking sequence without a barrier layer. The Y_2O_3 layer serves as a nucleation layer for the IBAD MgO. Secondary emission mass spectroscopy (SIMS) on this type of sample shows significant diffusion of Ni, Cr, and Mo from the substrate into the YBCO layer. Samples with this architecture have T_c values less than 75 K, i.e., the cation diffusion is very detrimental for the superconducting properties.
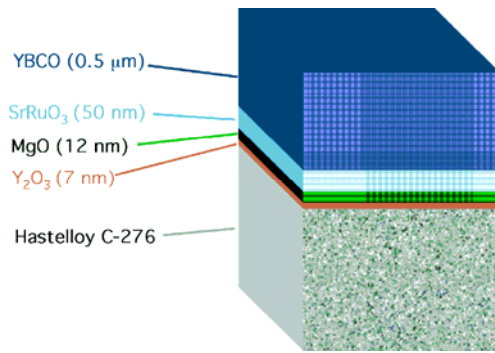
Fig. 2a. Stacking sequence for a coated conductor with no barrier layer.
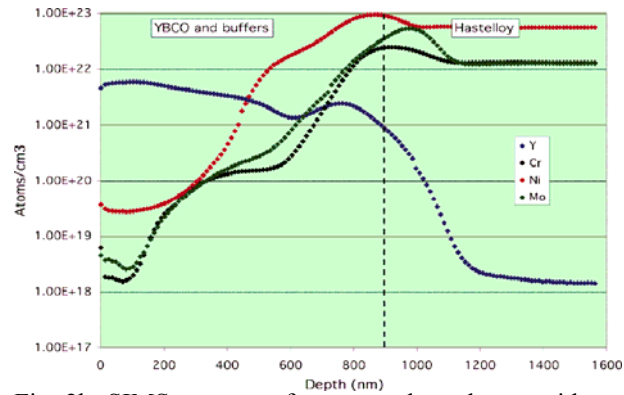
Fig. 2b. SIMS spectrum for a coated conductor with no barrier layer. Note the diffusion of the substrate cations Ni, Cr, and Mo into the YBCO layer.

YBCO coated conductors using IBAD YSZ are thought not to have a cation diffusion problem because of the thickness of the IBAD layer. For the IBAD MgO process, it should be possible to add or use thicker epitaxial layers above the MgO. Another possible solution is to employ a barrier layer below the MgO. For example, cation and oxygen diffusion through Al_2O_3 at normal YBCO processing temperatures is much lower than for other common oxide materials. Fig. 3a shows a stacking sequence using a thin (80 nm) Al_2O_3 barrier, and Fig. 3b shows the SIMS profiles for Y, Al, and Cr. The alumina layer acts as an effective barrier for all of these species. In fact, Fig. 3c shows that all cation species of interest present in the substrate have low diffusion rates into the YBCO. The T_c of a sample with this architecture is ~86 K.
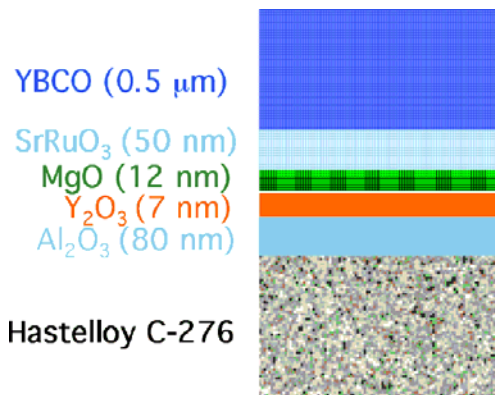
Fig. 3a. Stacking sequence for a coated conductor with a thick alumina barrier layer.
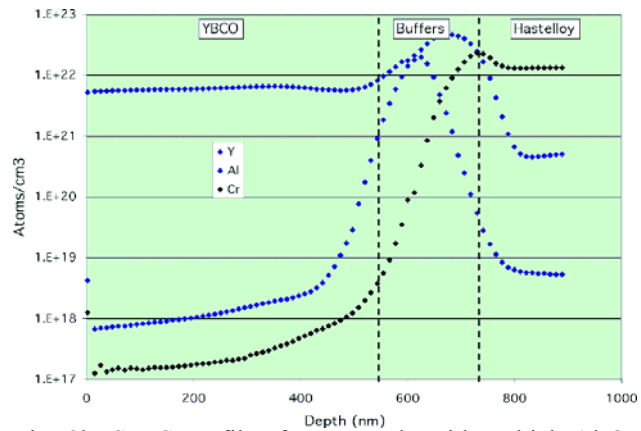
Fig. 3b. SIMS profiles for a sample with a thick Al_2O_3 barrier layer.

Fig 3c. SIMS profiles of substrate cations showing the very low rate of diffusion through the Al_2O_3 and into the YBCO.
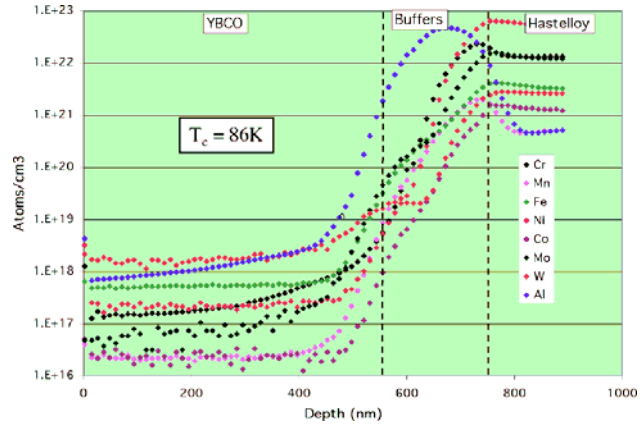
Another option to prevent cation diffusion is to combine the barrier layer with the nucleation layer. This can be done using a ~20 nm thick layer of Er_2O_3. A coated conductor produced with this layer sequence had very good properties: a T_c of 89.5 K and a critical current density J_c of 2.3 MA/cm^2 for a YBCO film thickness of 1.7 μm.
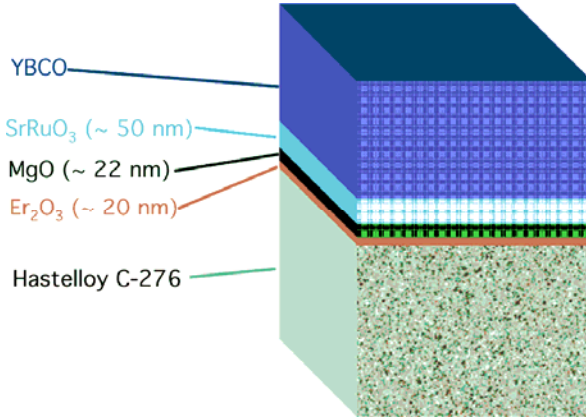
Fig. 4. Stacking sequence for a coating conductor with a combined nucleation/barrier layer of Er_2O_3. Samples with this architecture have very good superconducting properties.

B. IBAD MgO layer texture optimization: nucleation layer

One of the most important advantages of changing from an amorphous silicon nitride (a-Si_3N_4) to an yttria nucleation layer is the reduction in process sensitivity to the IBAD MgO film thickness. For the a-Si_3N_4, the best properties (in-plane texture) are achieved for the narrow range of ~7-10 nm, as shown in Fig. 5a. On the other hand, using yttria, good texture can be achieved from 5 nm to over 30 nm, Fig. 5b shows data on the c-axis tilt of the MgO crystals that may explain this phenomenon. For MgO films thicker than about 10 nm, the c axis begins to tilt away from the tape normal; this makes it more difficult to achieve in-plane texture, and may lead to surface roughening and degraded superconductor properties. In contrast, an yttria nucleation layer leads to no out of plane texture development for MgO films up to 30 nm, the thickest ones studied.
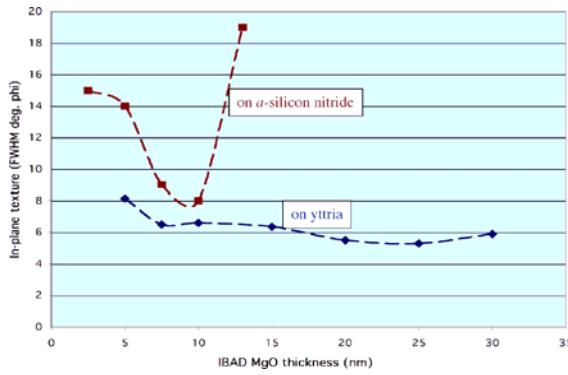
Fig. 5a. In plane texture as a function of IBAD MgO layer thickness for different nucleation layers.
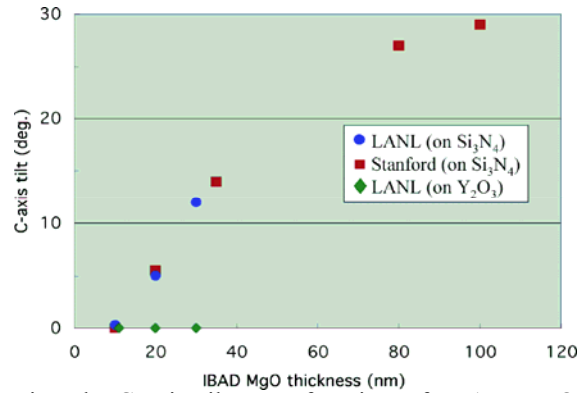
Fig. 5b. C-axis tilt as a function of IBAD MgO layer thickness for different nucleation layers.

In a transmission electron microscope study of the yttria layer, it was found to be nanocrystalline with random orientation, as shown in Figs. 6a and 6b.
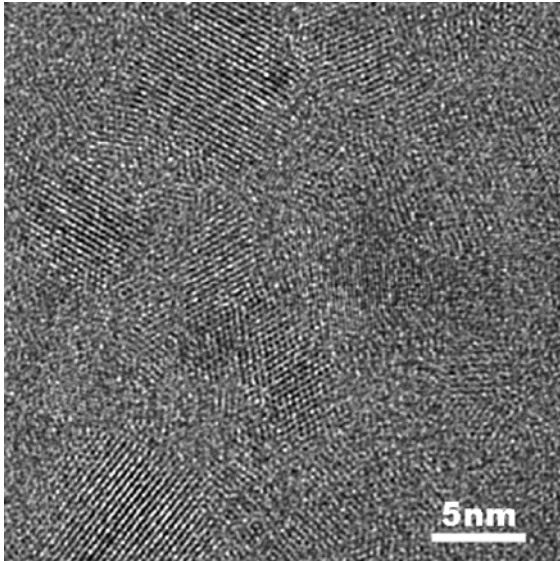
Fig. 6a. Plan view high resolution TEM image shows that the 10 nm thick yttria nucleation layer is nanocrystalline.
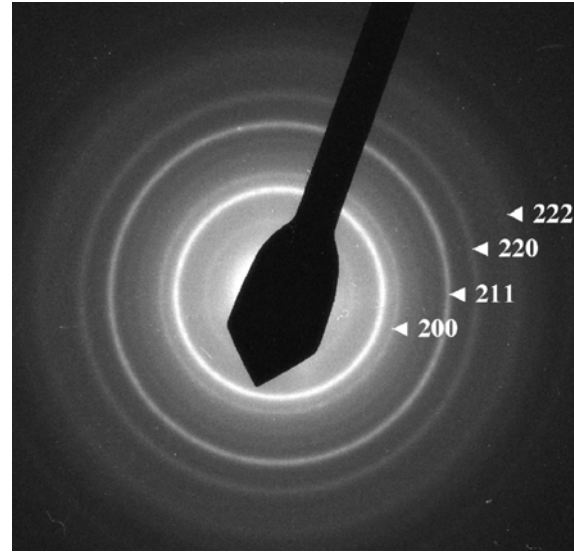
Fig. 6b. Selected area diffraction pattern of yttria nucleation layer.

TEM cross-section images (Figs. 7a and 7b) show that the growth morphology of the MgO on the two different nucleation layers studied has different character. Careful examination of the micrographs reveals the difference in the lattice tilt between the two. In the case of Fig. 7a, the IBAD MgO film is tilted with respect to the substrate surface. Although this film is only ~5 nm thick, as this film would continue to grow, the tilt would become more exaggerated and reduce the number of grains aligned with the assist beam. This change in alignment would result in more damage accumulation in the film and is a possible explanation for the quick degradation of IBAD MgO films grown on the Si_3N_4 nucleation layer. No effective tilting is observed in Fig. 7b where the IBAD MgO is deposited on Y_2O_3. The ability of the MgO to remain aligned to the ion beam as the film continues to grow beyond the thickness limit of IBAD MgO films grown on Si_3N_4 is a major advantage of the yttria layer.

20
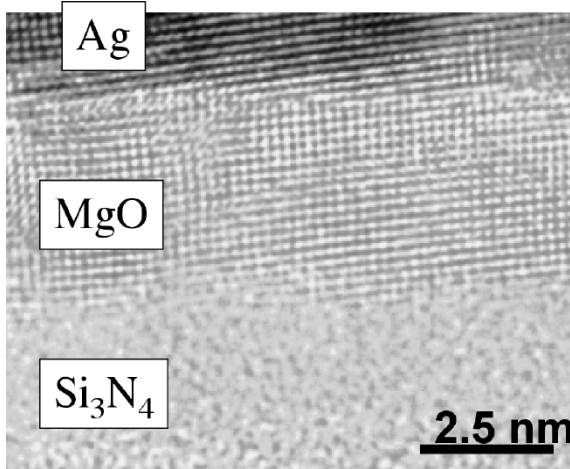
Fig. 7a. TEM cross-section image showing the character of the a-Si$_3$N$_4$ – MgO interface.
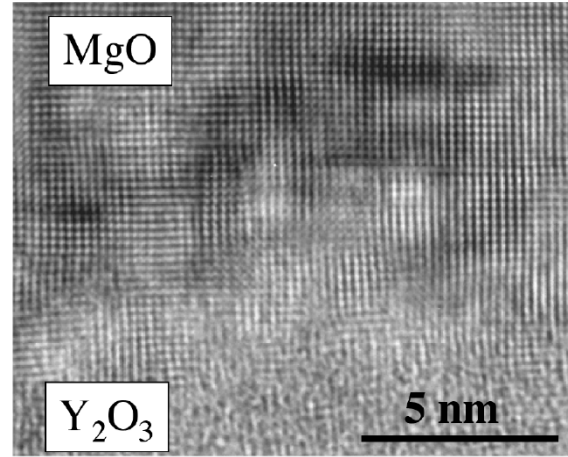
Fig. 7b. TEM cross-sectional image of the yttria – MgO interface.

C. IBAD MgO layer texture optimization: assist ion beam divergence

Improvements in the assist ion beam divergence have resulted in better texture in the template layer. Fig. 8a shows the clear correlation between assist ion beam divergence and the in plane texture of the MgO. Fig. 8b shows the angular dependence in the x-ray intensity with the beam divergence optimized for both phi and omega angle scans, measuring the in plane and out of plane texture, respectively.
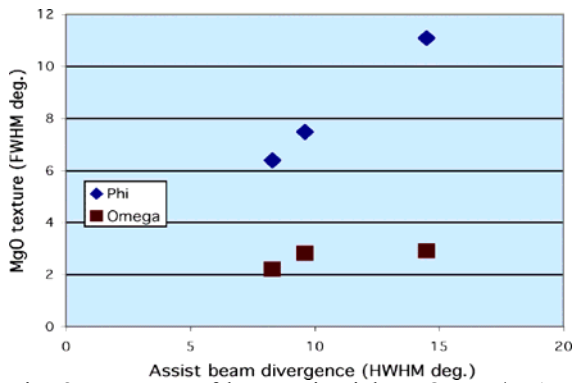
Fig. 8a. Texture of homoepitaxial MgO on /IBAD MgO/yttria/Si. Phi characterizes the out of plane and omega, the in plane texture.
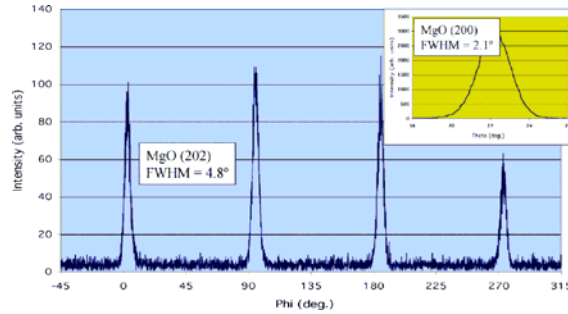
Fig. 8b. Improved texture in IBAD MgO templates is achieved with reduced assist ion beam divergence.

Fig. 9a shows the improvement from July 2002 to July 2003 in in-plane texture for IBAD MgO meter length tapes on an yttria nucleation layer with an alumina barrier layer on a metallic substrate. There is a clear decrease in the median value and significantly lower values than were achieved earlier. Fig. 9b indicates some of the possible reasons for the trend to better texture. Better mechanical polishing (3.5 nm rms) led to a reduction in the phi FWHM from previous values to a little greater than 8 degrees. At that point, electropolishing was introduced into the process and the substrate roughness was reduced to ~0.5 nm rms. At the same time, improvements were made in the assist ion beam divergence. A combination of these two improvements leads to the present FWHM values of slightly under 7 degrees.
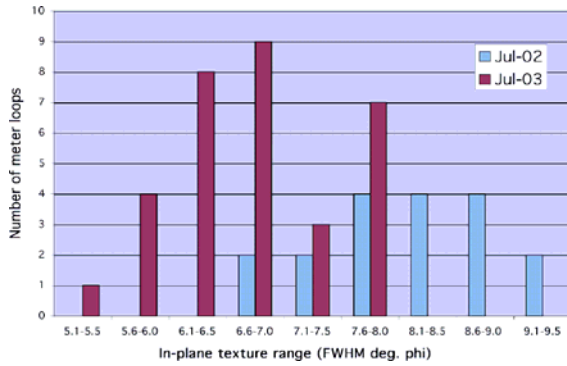
Fig. 9a. Improvement of the inplane texture for IBAD MgO meters on Hastelloy substrate.
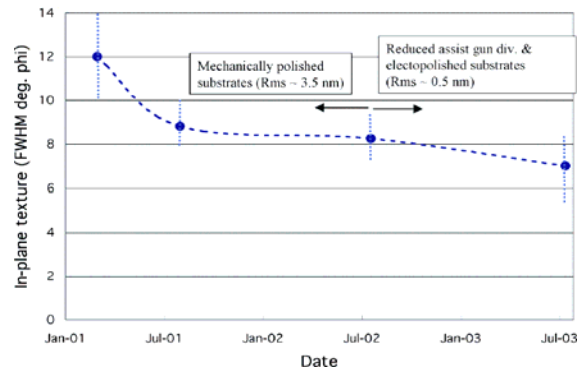
Fig. 9b. Improvements in IBAD MgO texture as a function of time.

To summarize progress made this year in IBAD MgO template development, a study of barrier layers, which prevent cation diffusion from the substrate into the YBCO during the high temperature processing stage, show that alumina acts as a very strong diffusion barrier. This was determined by use of SIMS to measure the cation concentrations as a function of distance from the substrate surface. It was also determined that yttria could be used as a nucleation layer, instead of a-Si$_3$N$_4$, and that it has a major advantage. With yttria the IBAD MgO layer thickness for good texture is much less sensitive to thickness than it was for a-Si$_3$N$_4$. This is thought to be caused by a c-axis tilt of the MgO when films thicker than 10 nm are deposited on a-Si$_3$N$_4$. In contrast, no c-axis tilt is observed for IBAD MgO films on yttria as thick as 30 nm. This is sufficiently thick for all coated conductor applications. It was found that erbia could function both as a barrier layer and as a nucleation layer. Improvements in polishing and in assist ion beam divergence led to a decrease in the average in plane texture FWHM peak width of about 1.5 degrees.

Future work will be to use ion-milling and SIMS to determine the quantitative tolerance of YBCO to diffusing substrate materials, and use this information to minimize the nonsuperconducting layer thickness. Additionally, the development of a single material that can serve as both a barrier and nucleation layer with the goal to reduce the number of layers by one, and reduce the barrier/nucleation layer thickness by 20 nm, with no reduction in performance.

2.1.2 Microstructural factors affecting critical currents in coated conductors
Q.X. Jia, S.R. Foltyn, P.N. Arendt, H. Wang, Y. Lin, L. Civale, M. Hawley, C.J. Wetteland, and J. MacManus-Driscoll

The goal of this activity is to explore the fundamental correlation between structural and transport properties of coated conductors through a comparative study of YBCO films on single crystal and IBAD MgO substrates. This should lead to development of a more controllable and reproducible process to fabricate high performance coated conductors.

The LANL process for coated conductors uses ion beam assisted deposition (IBAD) of MgO on commercial polycrystalline metal substrates. For a single crystal substrate, the texture is derived from homo- and/or hetero-epitaxial growth at elevated temperatures. On a polycrystalline substrate, a textured template must be provided before growth of the epitaxial layers is possible. The stacking sequence is shown in Fig. 10.
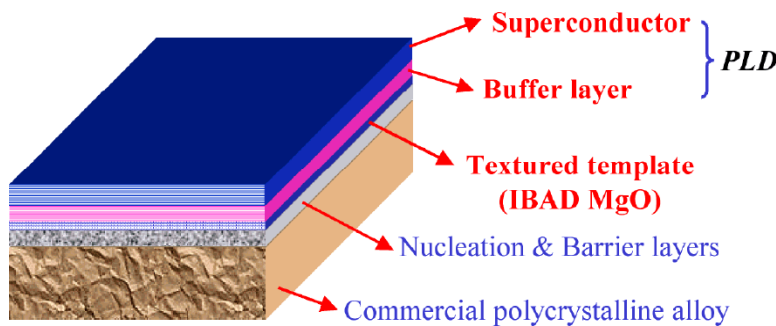
Fig. 10. Schematic of coated conductor architecture through the superconductor layer.

A smooth and highly crystalline IBAD MgO surface makes it possible for subsequent epitaxial growth of the buffers and HTS films. The surface smoothness is largely a result of the surface finish of the Hastelloy substrate. Continuing improvements (Fig. 11a) in polishing techniques, including the switch to electropolishing, have led to substrate surface roughnesses of only 0.5 nm RMS. X-ray reflectivity measurements show that the surface roughness of the IBAD MgO is only slightly worse than that of MgO on a single crystal substrate, 1.0 nm vs. 0.6 nm RMS, respectively.

This improvement in surface condition now makes it possible to achieve better in-plane texture (Figs. 11a and 11b). This in turn allows the use of any of three buffer materials with comparable results for in-plane texture. Fig. 12a indicates that for poor IBAD MgO in-plane alignment ($\sim$>10°), $SrRuO_3$ results in the best in-plane texture in the YBCO. However, for IBAD-MgO better than this, the differences in the YBCO texture for the three different buffer layer materials is very small. Thus, it is possible to use $SrTiO_3$, $LaMnO_3$, or $SrRuO_3$ with comparable structural compatibility with MgO and YBCO. The choice of buffer layer material can then be focused on other favorable properties. For this reason, $SrTiO_3$ (STO) has been chosen because of its chemical and thermal stability, its low cost and its availability as a high-density target. The good chemical compatibility of the STO buffer layer can be seen in the Rutherford Back Scattering (RBS) data in Fig. 12b. The stoichiometry of the 1.5 μm thick YBCO film is correct, with no evidence of diffusion of other elements through the buffer.
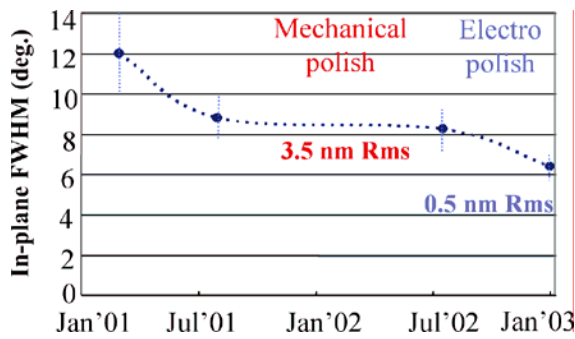
Fig. 11a. Improvements in surface roughness of the coated conductor substrate.
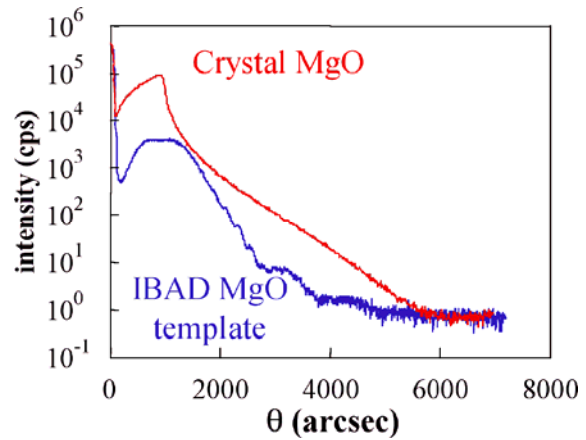
Fig. 11b. Width of x-ray peak for IBAD MgO and MgO on a single-crystal substrate.
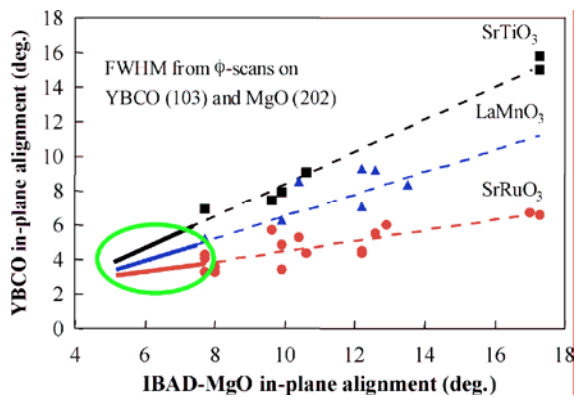
Fig. 12a. Dependence of YBCO in-plane texture on MgO-IBAD in-plane texture for several buffer layer candidates.
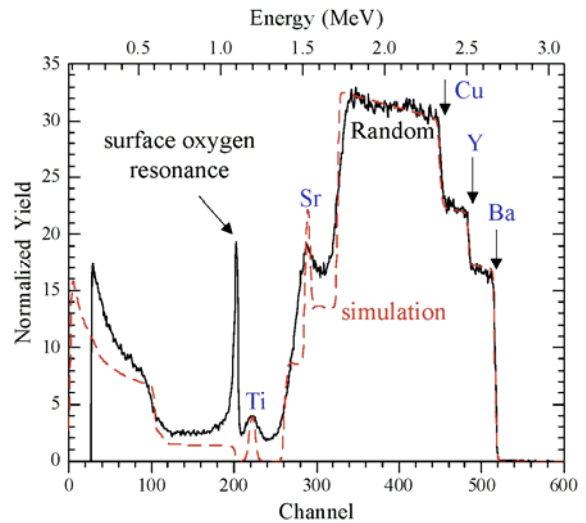
Fig. 12b. Rutherford Backscattering pattern for YBCO showing good stoichiometry for the YBCO film with an STO buffer.

Fig. 13 shows the effect of increasing YBCO film thickness on c-axis tilt. For thin (0.2 μm) YBCO, the tilt is measurable; however, for much thicker (1.5 μm) YBCO, this tilt becomes negligible. For the thicker film, other factors besides the epitaxial MgO surface are more critical for determining the film out of plane orientation.
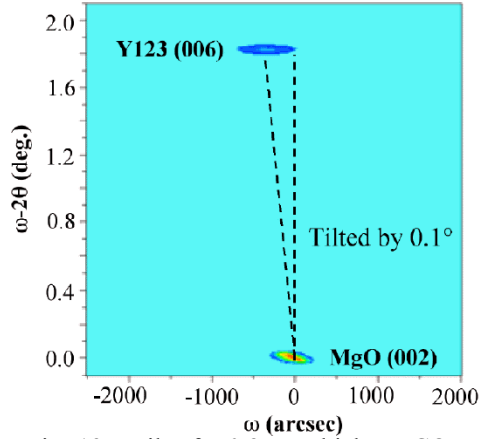
Fig. 13a. Tilt of a 0.2 μm thick YBCO c-axis from the single crystal substrate normal.
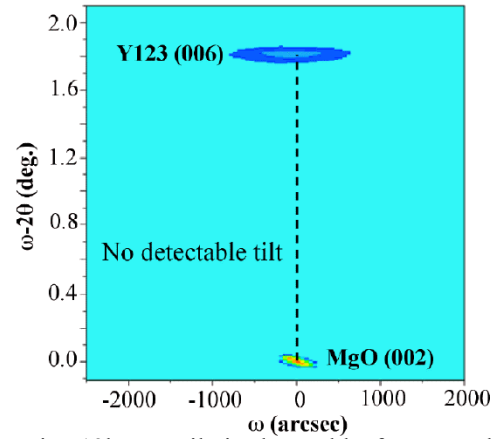
Fig. 13b. No tilt is detectable for a much thicker (1.5 μm) YBCO film on single crystal MgO.

Fig. 14a shows the RBS ion channeling spectra of YBCO on crystalline MgO. Low χ_{min} is a direct indication of a good quality epitaxial layer. Point defects, impurities, dislocations, and slightly different orientations can all contribute to a large value of χ_{min}. Fig. 14b shows that as the film gets thicker the out of plane texture (narrowness of peak width in a rocking curve or ω scan) degrades only slightly. The in-plane texture (FWHM of (103) peak in φ scan) remains unchanged at 1.4°. Meanwhile, the ion channeling yield χ_{min} varies from 4% (high quality) for the 0.2 μm thick film to about 28% for the 1.5 μm thick film.
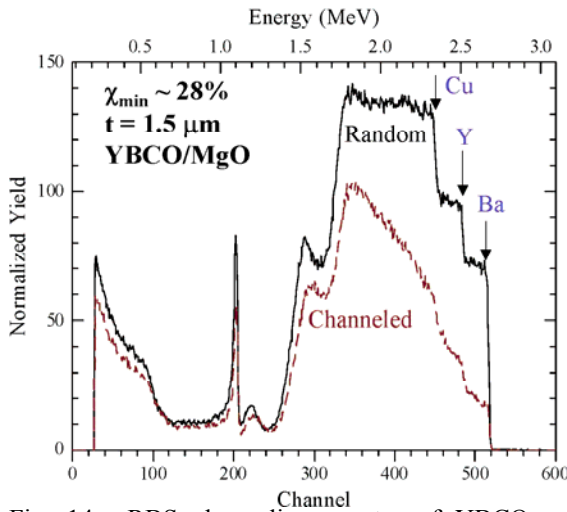
Fig. 14a. RBS channeling spectra of YBCO on single crystal MgO.
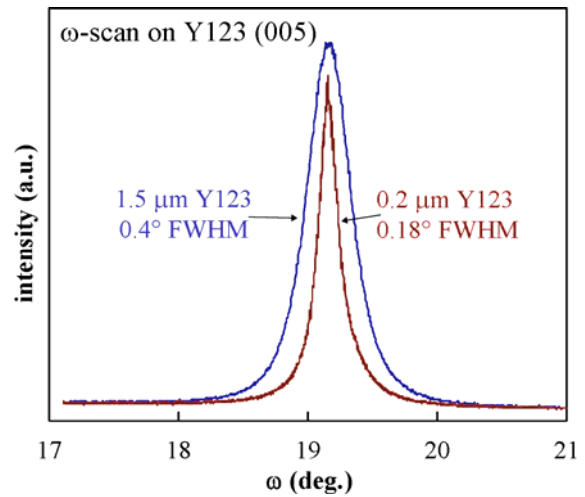
Fig. 14b. Comparison of rocking curves of YBCO (005) peak for a thin and thick film on single crystal substrates.

Fig. 15 shows the high crystalline quality of the MgO/STO and the STO/YBCO interfaces for films grown on single crystal MgO. There are no extra impurity or reaction layers present, so that the growth is also seen to be epitaxial at both interfaces.
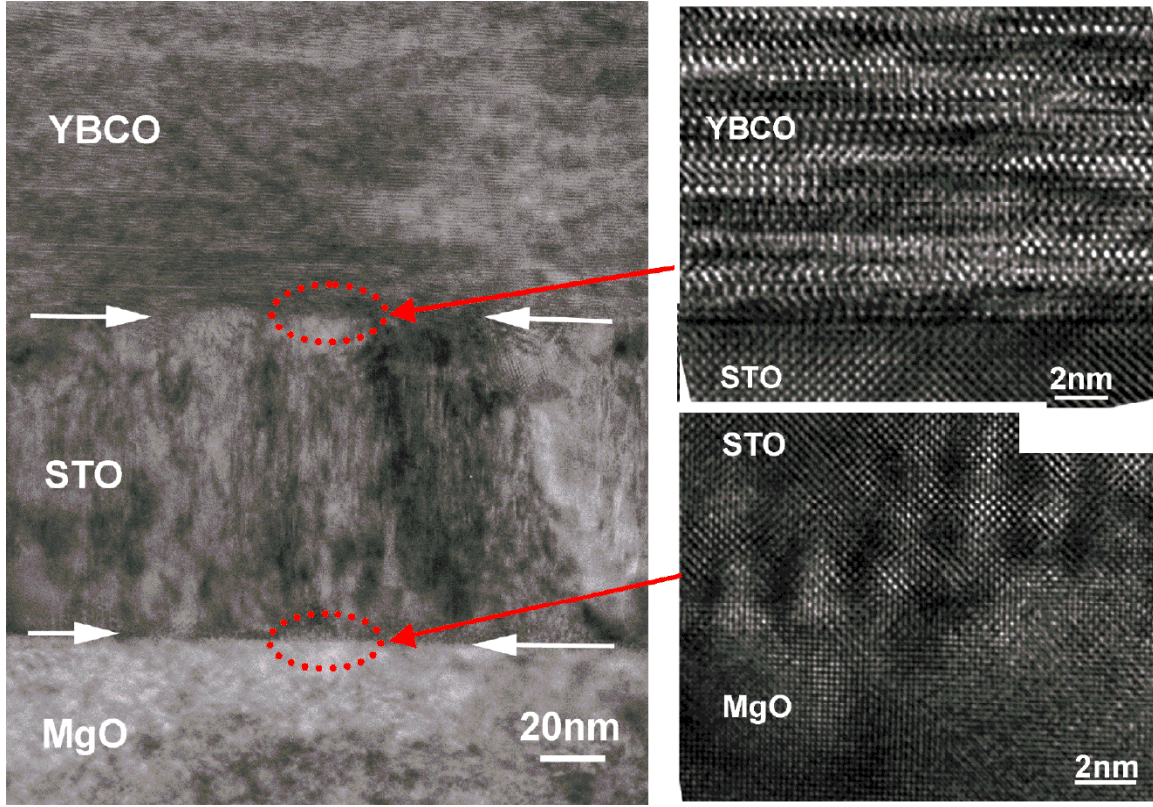
Fig. 15. TEM image shows that the MgO/STO and STO/YBCO interfaces are both clean, highly crystalline.

Comparisons of YBCO on crystal substrates with YBCO on IBAD-MgO/metal alloy substrate indicate that the properties are not significantly different for the latter. Fig. 16a shows a comparison of the out of plane mosaic, the ω-scan YBCO (005) peak width, which increases only a factor of 2 to 3 for the IBAD-MgO case. The smooth, highly crystalline IBAD MgO surface poses no limitations on surface quality for subsequent epitaxial growth of high performance YBCO films. The in-plane texture (Fig. 16b) of a thick YBCO film on IBAD MgO has only slightly larger ϕ-scan FWHM (2.4° vs. 1.4°-1.7°) for otherwise comparable films on single crystal MgO. Also, because of the improved in-plane texture, it is now possible to obtain RBS channeling data on a YBCO/STO/IBAD MgO/Hastelloy sample. Fig. 17 shows the spectrum for a 1.5 μm thick YBCO sample; the channeling yield χ_{min} is 65%.
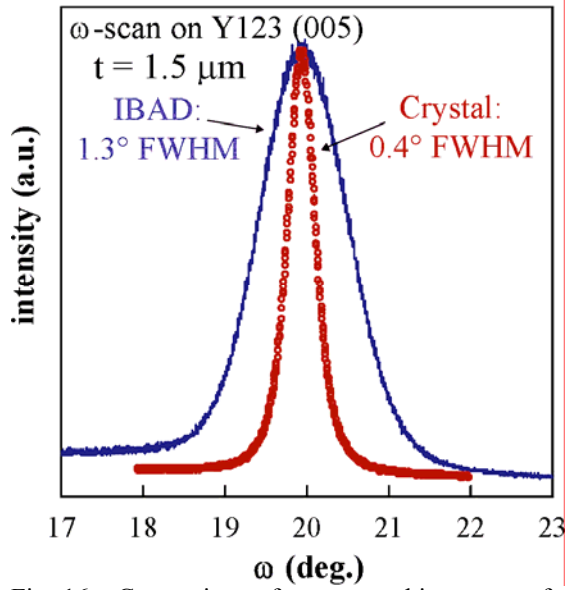
Fig. 16a. Comparison of ω-scan rocking curves for YBCO on crystal MgO and on MgO IBAD.
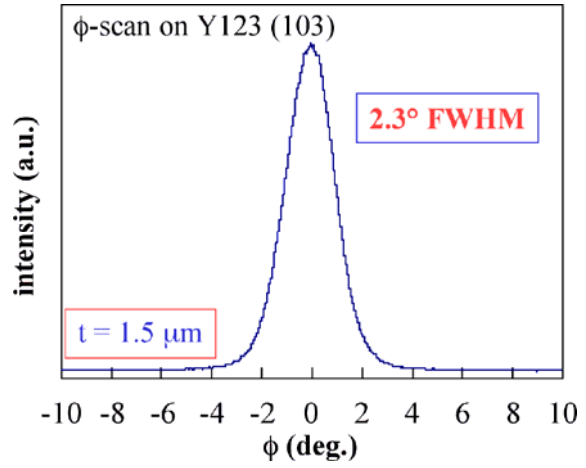
Fig. 16b. φ-scan on YBCO thick film on MgO IBAD.

Figs. 18a and 18b show a comparison of scanning tunneling microscope (STM) images of the surface morphology of thick YBCO on crystal MgO and on IBAD MgO. The latter sample surface shows that larger grains have formed from smaller clusters.

The STM images in Fig. 19 shows that the grains in a thick YBCO film on IBAD MgO are elongated. Fig. 19a shows the surface morphology, and Fig. 19b, the surface roughness along the line indicated in the STM image.
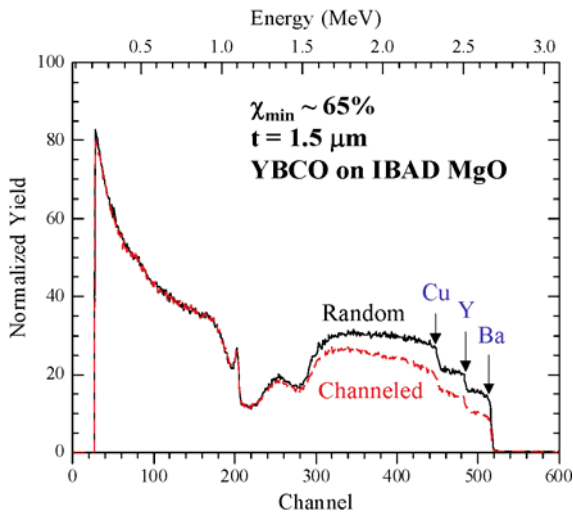
Fig. 17. RBS spectrum of YBCO on IBAD MgO showing the channeling yield.

27

0   1.0 μm
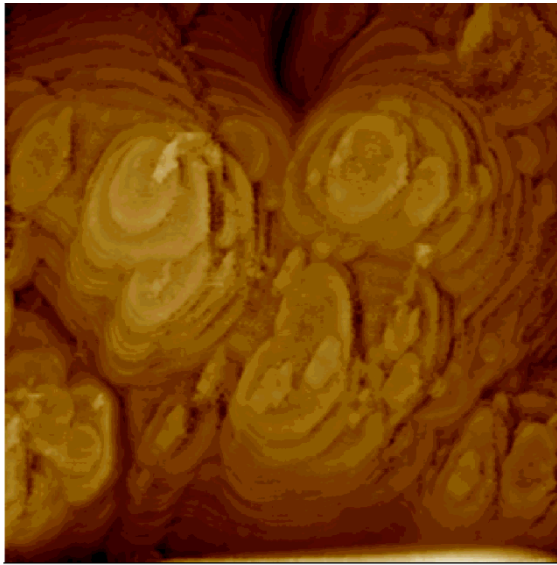
Fig. 18a. AFM image of YBCO on crystal MgO. YBCO film thickness is 1.5 μm.

0   1.0 μm
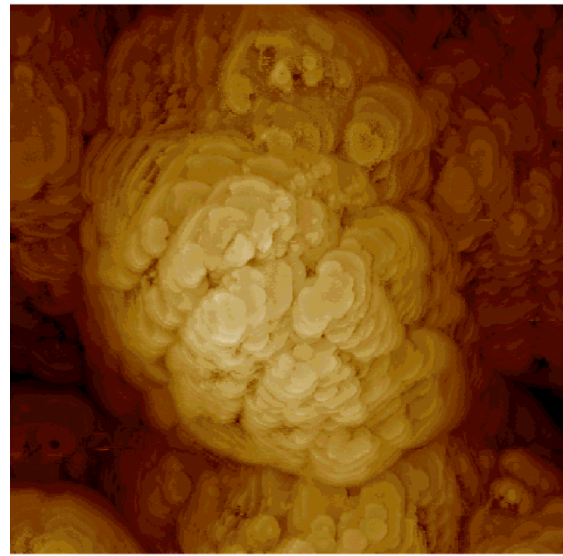
Fig. 18b. AFM image of YBCO on IBAD MgO. YBCO film thickness is 1.5 μm.
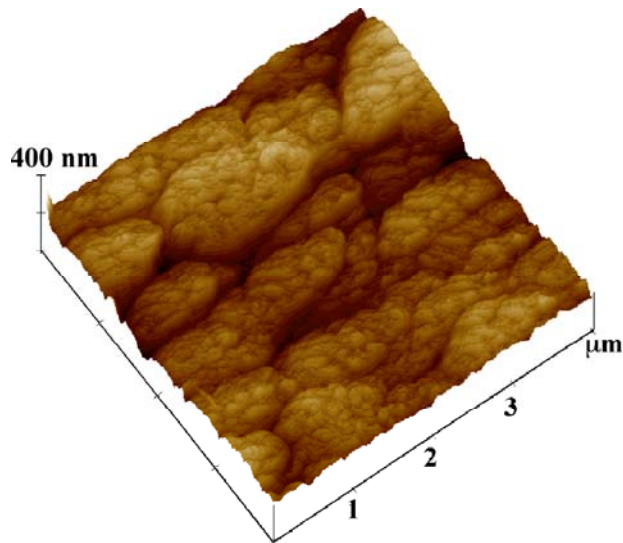
Fig. 19a. STM image of the surface of a thick YBCO film on an IBAD MgO template film. Note the elongated grains.
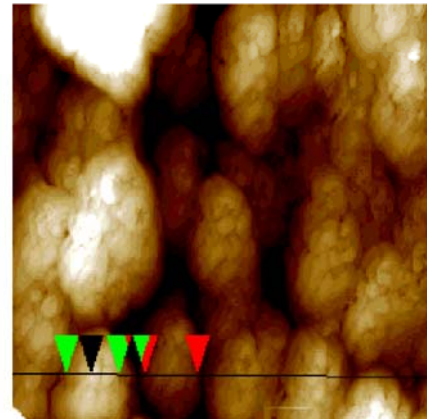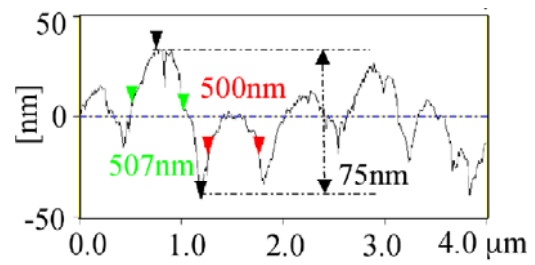
Fig. 19b. STM image and surface profile showing grain size and surface roughness. Same sample as in Fig. 19a.

28

Defects, such as dislocations and inclusions of second phases, act as strong vortex pinning centers. They play a critical role in the enhancement of critical current density in YBCO films. We have used high resolution x-ray diffraction (HRXRD) to evaluate the dislocation densities in the YBCO films. In this experiment, we measured the rocking curve (ω-scan) of the symmetric reflections YBCO (00l) by using a triple-axis diffractometer set-up. The density of screw type threading dislocations can be extracted from the Williamson-Hall plots through the following relationship:

$$FWHM_\omega = \alpha_\omega + \frac{\lambda}{\sin\theta} \bullet \frac{1}{2L} \tag{1}$$

where $FWHM_\omega$ is the FWHM value of the rocking curve, θ is the Bragg angle, λ is the wave length of the X-ray, α_ω is the tilt angle related to the screw dislocation, and L is the lateral coherence length. In Fig. 20, $FWHM_\omega(\sin\theta)/\lambda$ is plotted against $\sin\theta/\lambda$ for each reflection and fitted by a straight line. The slope of the plot is the tile angle α_ω, from which the density of the screw type threading dislocations can be calculated by

$$N_s = \frac{\alpha_\omega^2}{4.35b_c^2} \tag{2}$$

where b_c is the Burgers vector of the c-type threading dislocation.

The calculated densities of the screw dislocations for the YBCO films on metal with IBAD MgO as a template and single crystal MgO are 1.4×10^{10} /cm^2 and 3.4×10^9 /cm^2, respectively. These results show that the density of the screw dislocations is much higher for the YBCO film on the metal substrate, which is 4 to 5 times that on single crystal MgO. Because of a pseudocolumnar structure with each column consisting of small 3D crystallites, the IBAD MgO template may have more stacking faults, anti-domains or heterogeneities compared to single crystal MgO. The STO buffer layer may adapt to this kind of surface termination as well. The defects in STO could easily act as nucleation centers for screw dislocations in YBCO layer due to the spiral columnar growth. With more nucleation centers, the YBCO film on the IBAD MgO template would have more screw dislocations than the film on the single crystal MgO substrate.
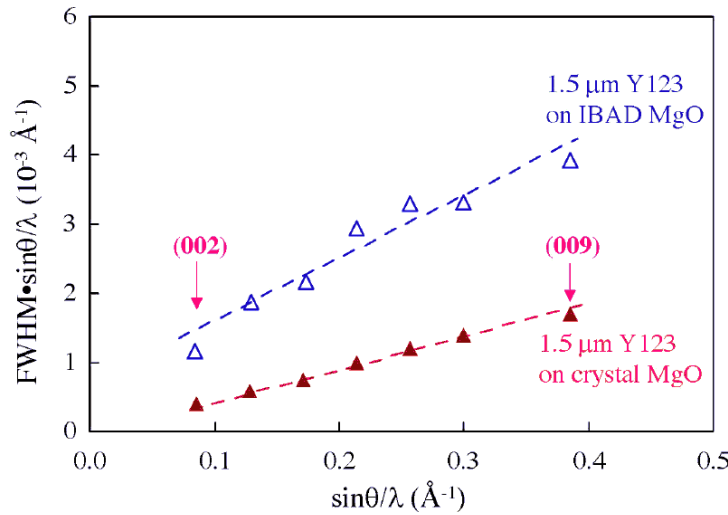
Fig. 20 Williamson-Hall plots for YBCO films on the Ni-alloy using IBAD MgO as a template and on single crystal MgO.

Fig. 21 shows TEM images of all layers of a 1.5 μm thick YBCO film on IBAD MgO. The IBAD MgO provides a good template for the epitaxial growth of the STO buffer layer. The interface between the STO and YBCO is sharp and clean with no evidence of a "dead layer" in the YBCO.

Fig. 22 compares TEM images of the YBCO/STO interface for films on crystal MgO (22a) and on IBAD MgO (22b). There are almost no observable differences, indicating the high quality of the films on IBAD MgO.

The J_c vs. thickness dependence of YBCO on IBAD MgO is essentially equivalent to that of YBCO on crystal YSZ and MgO substrates. Fig. 23 indicates the trend from 1992 using YSZ substrates to the present data.

Ion milling experiments were also carried out to look for any position dependence of J_c through the film thickness, i. e., the presence of "dead layers" near the interfaces, etc. The J_c of the sample on IBAD MgO was first measured, then the film was thinned using ion milling, the thickness and J_c measured, and this step repeated several times. The results are shown in Fig. 24. What was observed is that the thickness dependence of J_c is identical to that of as-deposited films on crystal MgO. There were no dead layers found, and the supercurrent was found to flow through the entire film thickness.
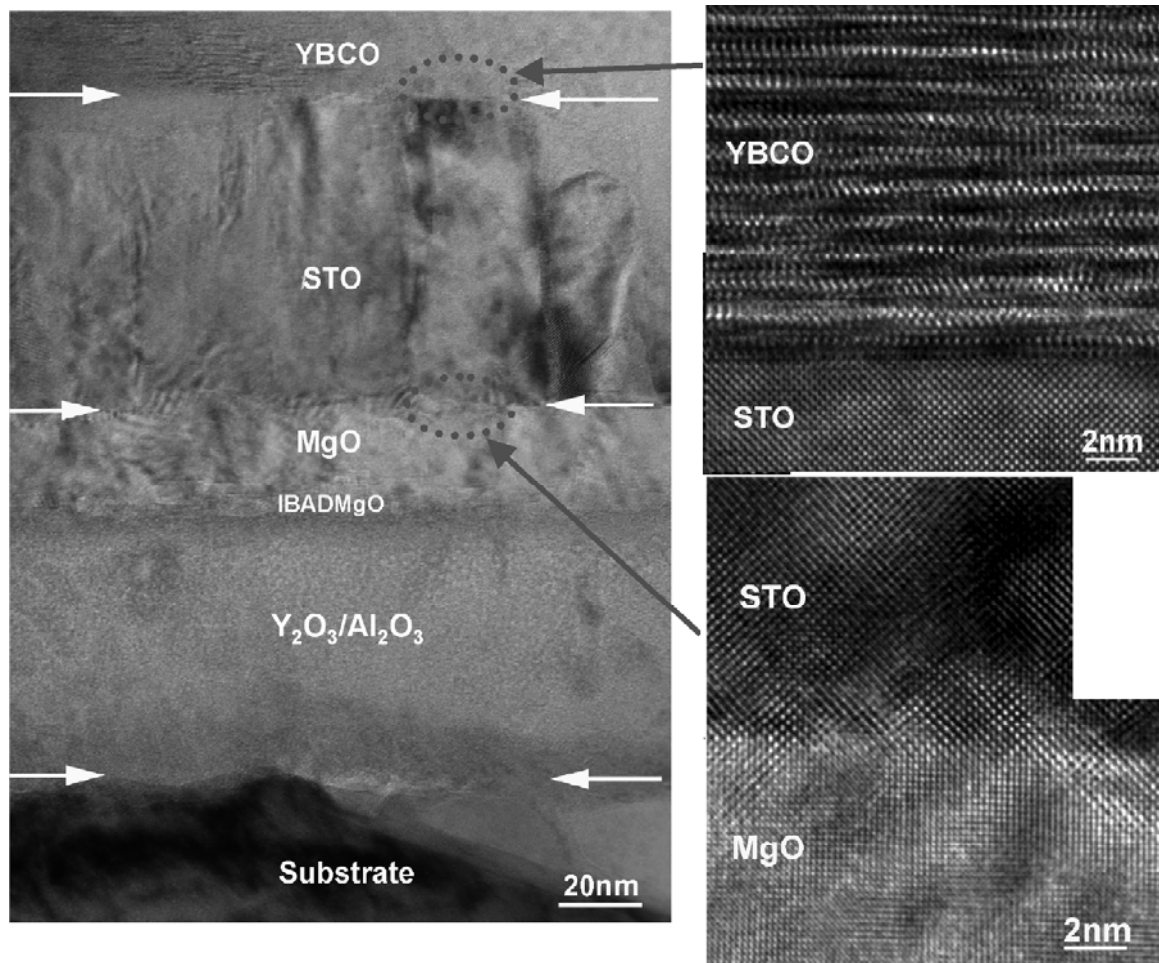
Fig. 21. TEM images of all layers of the YBCO coated conductor. The white arrows indicate the location of the various interfaces. The gray arrows show the location of the expanded images on the right.

30
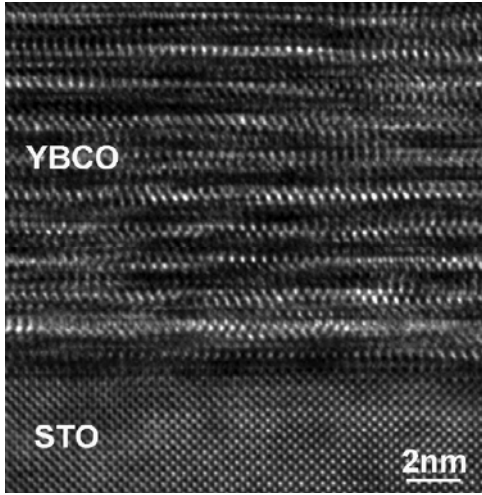
Fig. 22a. YBCO/STO interface for a film on crystal MgO
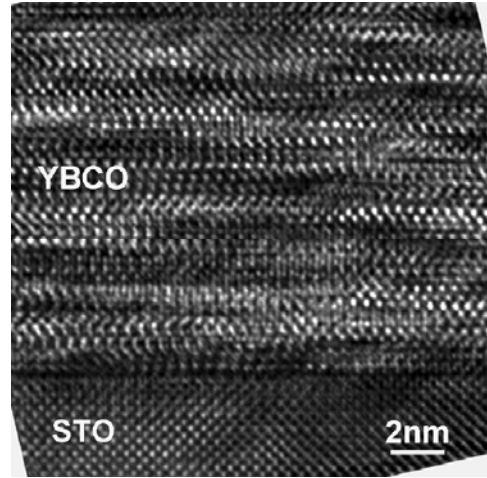
Fig. 22b. YBCO/STO interface for a film on IBAD MgO
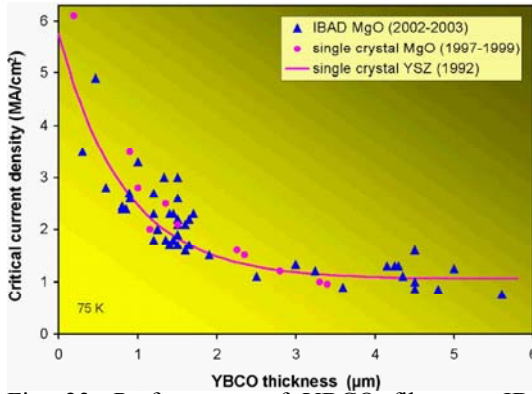
Fig. 23. Performance of YBCO films on IBAD MgO follow the same curve as those deposited on single crystals.
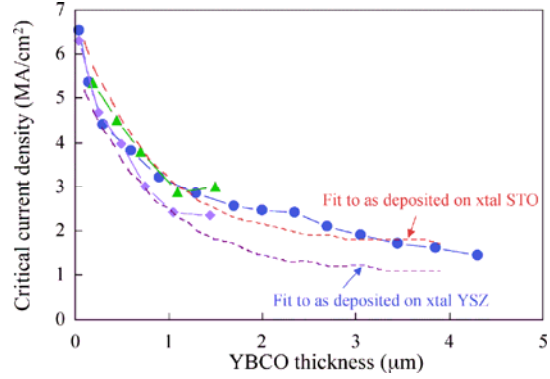
Fig. 24. Critical current density vs. YBCO thickness shows the same dependence on thickness for as deposited films and for films ion milled to different thicknesses.

To summarize, microstructure analysis illustrates that thick YBCO films on IBAD MgO are as good as the films on crystal MgO. XRD and RBS channeling have demonstrated that there is variation of microstructure through the film thickness. Both as-deposited and ion-milled films follow the same J_c vs. thickness relationship.

2.1.3 High current YBCO on IBAD MgO by pulsed laser ablation
S.R. Foltyn, P.N. Arendt, L. Civale, J.Y. Coulter, R. DePaula, P.N. Dowden, J.R. Groves, Q.X. Jia, Y. Li, B. Maiorov, L. Stan, H. Wang; (University of Cambridge): J. MacManus-Driscoll; (SuperPower, Inc.): J. Reeves

A. YBCO on MgO IBAD with near single crystal texture
As the texture of MgO IBAD improves, so does that of the YBCO films deposited upon this template. With the MgO IBAD in-plane texture in the 7° full width at half maximum (FWHM) range, the texture of YBCO is approaching that of films on single crystal MgO, as can be seen in Fig. 25 for a YBCO film 1.8 μm thick. The in-plane texture for this film on IBAD is only about 30% larger than that of YBCO on a single crystal substrate. While the value of the rocking curve FWHM is a factor of ~2.4 larger for the film on IBAD than on single crystal, the width is still very small on an absolute scale.
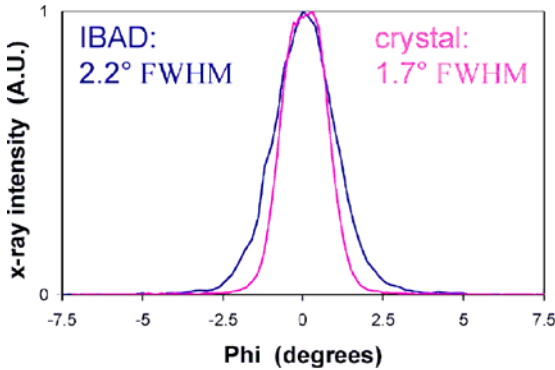
Fig. 25a. Phi scan of YBCO (103) peak for films on IBAD and on crystalline substrates.
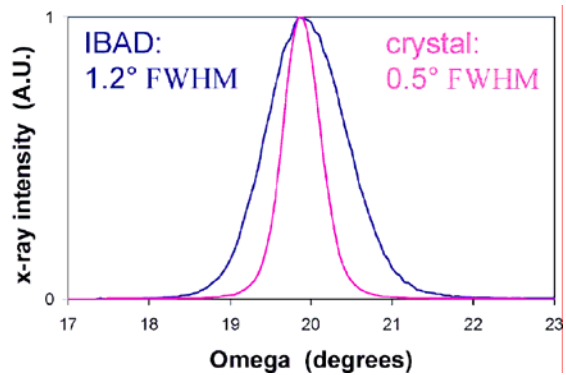
Fig. 25b. Rocking curve (omega scan) of YBCO (005) peak on IBAD and on single crystal substrates.

In July of 2002, the critical current density J_c levels of YBCO of IBAD MgO were below the best values achieved for YBCO on IBAD YSZ. However, the improvements achieved in in-plane texture by July 2003 routinely yield higher performance, as seen in Fig. 26. Part of this performance enhancement resulted from changing the buffer layer material from $SrRuO_3$ (SRO) to $SrTiO_3$ (STO). Because the STO does not improve the YBCO texture as much as the other two buffer layers, shown in Fig. 27, it cannot be used until the IBAD MgO texture is less than about 8° FWHM.

STO is a chemically stable buffer material that aligns well on MgO and is an excellent lattice match for YBCO. Figs. 28a and 28b show that both the top and bottom interfaces of the STO layer are smooth and free of chemical reaction products. These properties help to make it a prime candidate for a buffer layer.
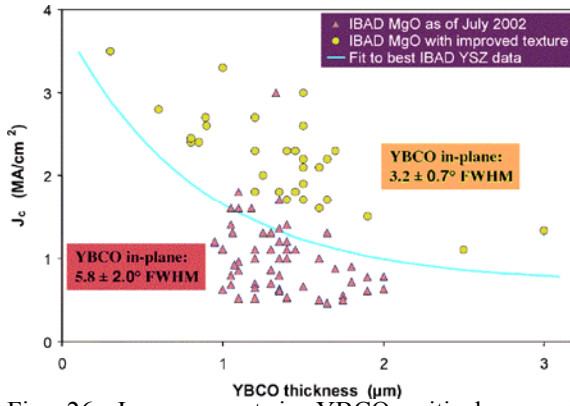
Fig. 26. Improvement in YBCO critical current density with time.
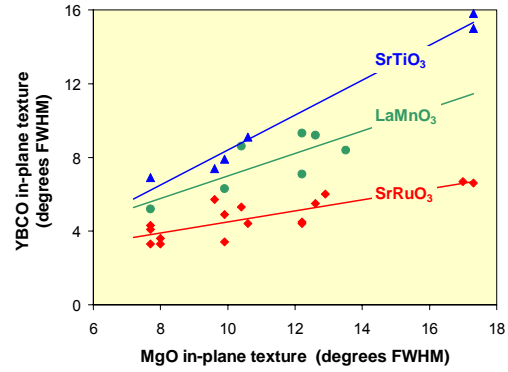
Fig. 27. Improvement in texture for various buffer layers on IBAD MgO.
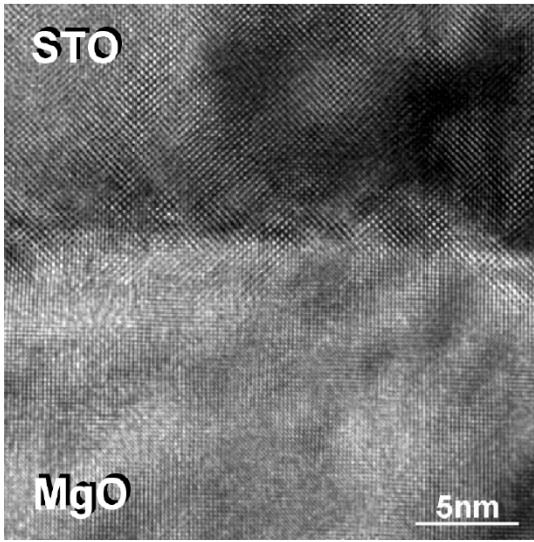
Fig. 28a. High resolution TEM cross-section image of the MgO – STO interface.
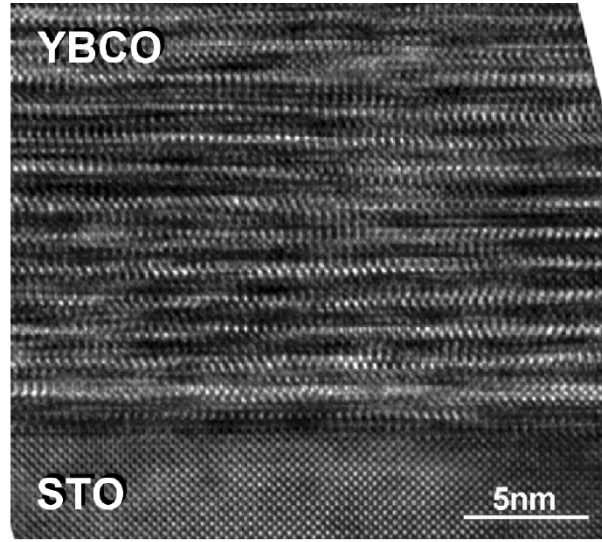
Fig. 28b. High resolution TEM cross-section image of the STO – YBCO interface.

Because of the improved texture in the IBAD MgO, the J_c values are now comparable to those achieved using single-crystal substrates, as shown in Fig. 29. This figure shows a fitted curve for the 1992 study of YBCO on single-crystal YSZ and the more recent LANL study of YBCO on single-crystal MgO. One suggestion as to why the performance is comparable refers to the dependence of J_c on misorientation angle in bicrystal experiments on YBCO, Fig. 30. It was found in three separate studies that perfect grain alignment is not required to reach single-crystal J_c levels. Instead, there is a plateau in J_c for angles below 5-10°. This same phenomenon, if it is present in IBAD MgO based films also, could explain the present results.
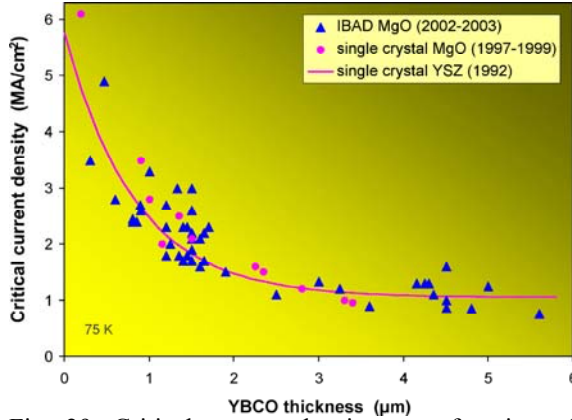
Fig. 29. Critical current density as a function of YBCO film thickness for several templates.
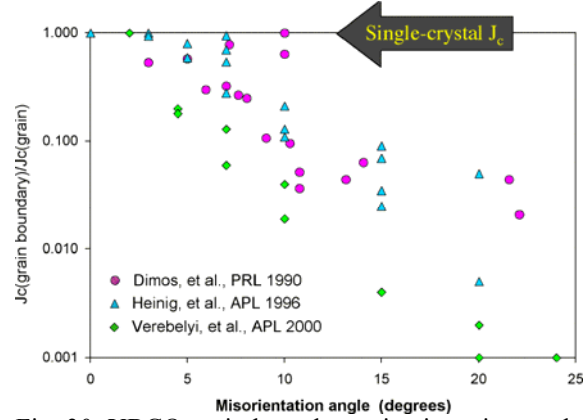
Fig. 30. YBCO grain boundary misorientation angle dependence of J_c from various studies.

One of the possible explanations for this threshold behavior is that the YBCO crystallinity is barely disrupted in very low angle grain boundaries. Fig. 31 shows a TEM image of a low angle grain boundary in YBCO on IBAD MgO. As can be seen, there is little disturbance of the atomic planes by the boundary.
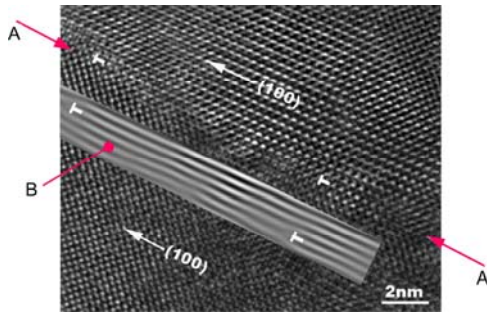
Fig. 31. Plan view TEM showing a 2.2° grain boundary in YBCO on IBAD MgO. The [001] tilt boundary plane is indicated by A, and a Fourier filtered image, showing more clearly the dislocations separated by ~11 nm, is indicated by B.

It may also be that the 1992 single-crystal YSZ curve is an outdated benchmark. To check this, a more recent data set on the best possible substrate, SrTiO$_3$, was obtained as shown in Fig. 32a. Indeed, the new J_c data values are uniformly higher than the older ones. Empirical fits to the data are shown by the solid lines and by the equations in the figure. Fig. 32b shows that the J_cs for the best YBCO films on IBAD MgO still compare favorably with this newer benchmark.
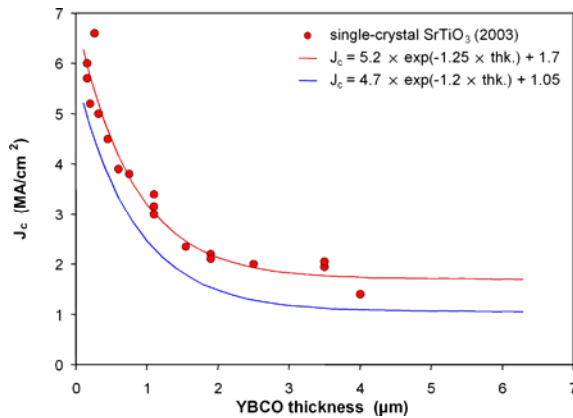
Fig. 32a. Comparison of previous benchmark curve for J_c vs. thickness with recent data for YBCO on SrTiO$_3$ substrates.
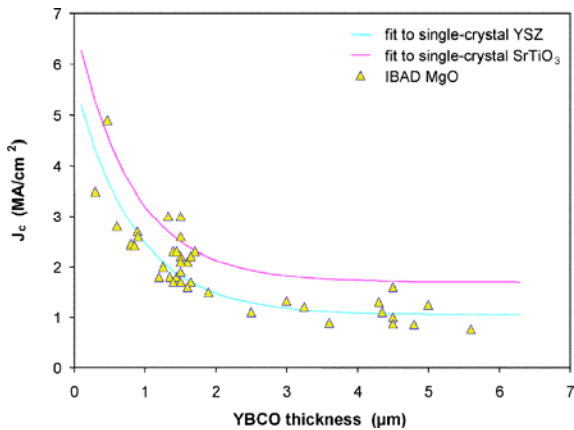
Fig. 32b. J_c for YBCO on IBAD MgO as a function of film thickness.

34

B. High critical current YBCO on IBAD MgO

In our previous work on YBCO deposited on IBAD yttrium-stabilized zirconia (YSZ), it was found (Fig. 33a) that, regardless of film thickness, the maximum achievable critical current I_c was about 250 A/cm width. It was confirmed by means of ion milling thick samples to various thicknesses and measuring I_c at each thickness (Fig. 33b), that for these films, only the first ~1.5 µm was effective at carrying current; the material greater than this thickness carried almost no current.
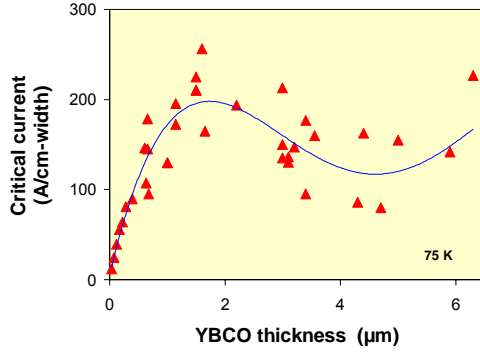
Fib. 33a. Critical current I_c as a function of YBCO film thickness for a YSZ IBAD template layer. I_c saturates near 250 A/cm width.
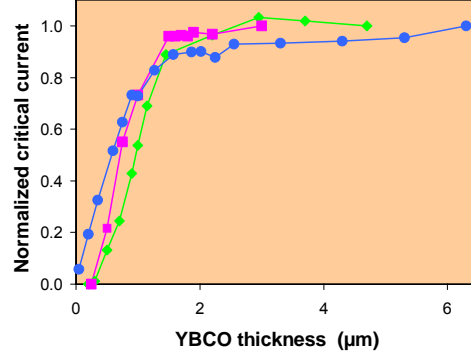
Fig. 33b. Normalized I_c as a function of YBCO film thickness for films ion milled progressively from 4.5 µm (red line, diamonds) and ~ 6 µm (blue line, circles) thicknesses.

If instead of a single, thick YBCO layer, a multilayer stack of roughly 1 µm thick YBCO and (much thinner) SmBCO layer pairs is deposited (Fig. 34a) to a total thickness of 4 to 6 µm, the critical current is found to depend nearly linearly on the thickness (Fig. 34b). This indicates that the full YBCO thickness of the film stack carries current and that the critical current density is nearly uniform throughout the YBCO, in contrast to the result for the single layer film (Fig. 33b).
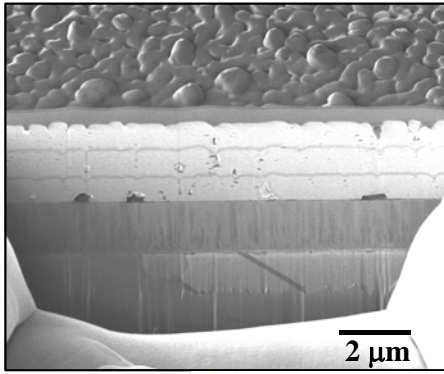
Fig. 34a. SEM cross section image of multilayer YBCO/SmBCO thick film.
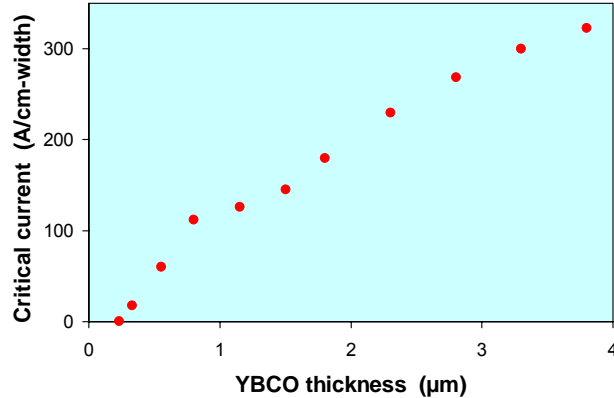
Fig. 34b. Critical current as a function of YBCO thickness in a thick 4 µm thick film measured as a function of thickness after progressively ion milling to thin the sample.

However, more recently, with the replacement of the IBAD YSZ template with the much thinner, faster to deposit, and smoother IBAD MgO template layer, it is now possible to achieve high critical current densities (Fig. 35) in single layer thick YBCO films, i.e., high critical currents are now achievable with a single layer.
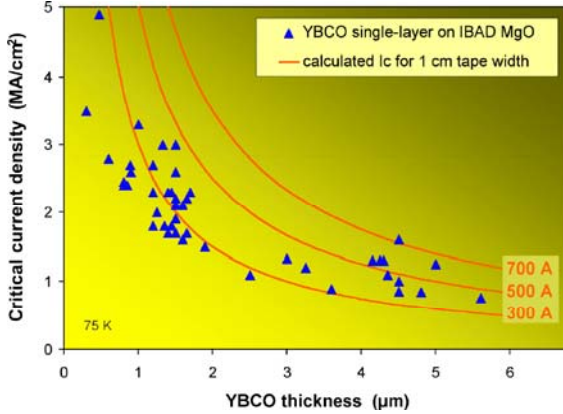
Fig. 35. Critical current density for single layer YBCO films on IBAD MgO as a function of YBCO film thickness.

The source of the different top surface morphology for YBCO films on the two different template layers (Fig. 36) is likely a result of the much smoother substrate surface in the case of MgO (Fig. 36b). This tends to reduce cumulative roughening (Fig. 36a) that is believed to lead to lower connectivity of the YBCO grains.

The YBCO microstructure for films deposited on IBAD MgO is very dense and largely free of porosity (Fig. 37), in sharp contrast with the gradually deteriorating and more porous structure seen for thick YBCO on IBAD YSZ. The present result is consistent with the better through thickness performance seen in the ion milling experimental results in Fig. 38. The dependence of J_c on thickness for YBCO on MgO (Fig. 38a) is now comparable with that of films on single crystal substrates, instead of falling off significantly faster, as was the case for YBCO on IBAD YSZ. The data of Fig. 38b indicate that instead of reaching a plateau at 250 A/cm width at about 1.5 μm for IBAD YSZ, as in Fig. 33, I_c for YBCO on MgO IBAD keeps increasing with thickness well above 2 μm to more than 600 A/cm width near 4 μm thickness.
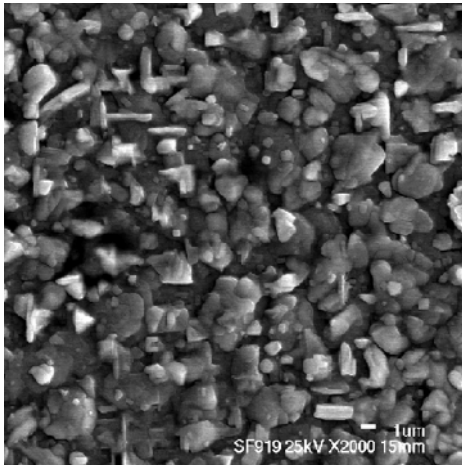
Fig. 36a. SEM image of the rough surface of a 3 μm thick YBCO film on an IBAD YSZ template layer. J_c(sf, 75.5K)= 0.6 MA/cm^2.
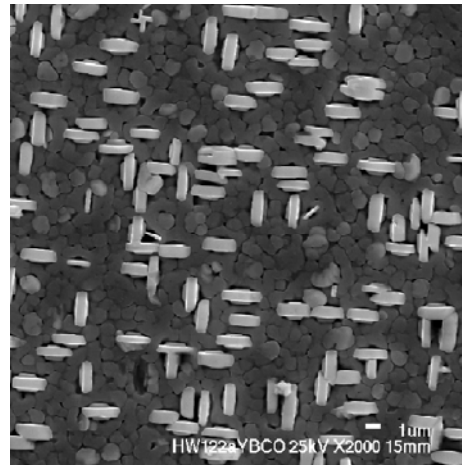
Fig. 36b. Significantly smoother surface of a 4.5 μm thick YBCO film on an IBAD MgO template layer. J_c(sf, 75.5K) =1.6 MA/cm^2.
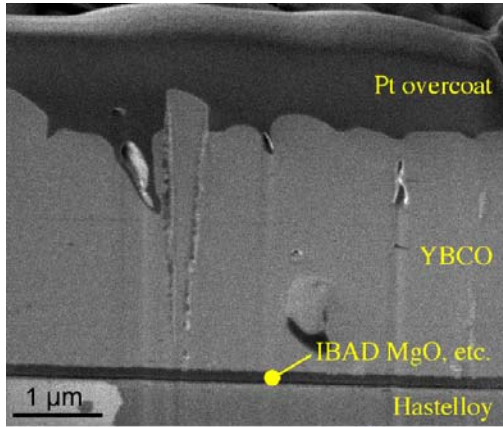
Fig. 37. Focused ion beam prepared cross section (viewed at 45º) of a 4.5 μm thick YBCO film deposited on an IBAD MgO template. The film has J_c(sf, 75.5K) > 1.0 MA/cm^2
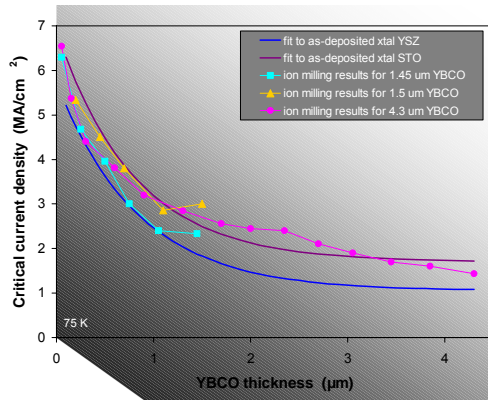
Fig. 38a. J_c as a function of film thickness for YBCO on single crystal substrates and for ion milled films on MgO IBAD.
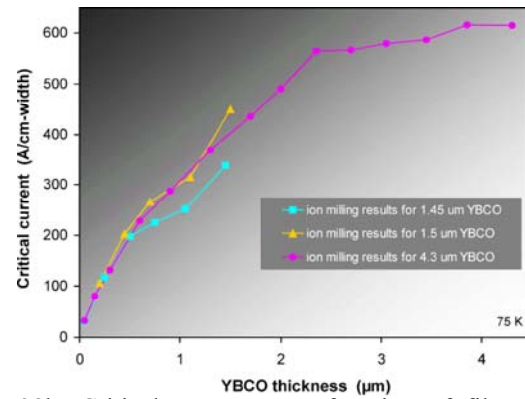
Fig. 38b. Critical current as a function of film thickness for three progressively ion milled YBCO films on MgO IBAD.

C. High critical current continuously processed tapes

As a result of the advances in template layer development, it is now possible to achieve greatly improved YBCO J_c performance. After solving a problem with temperature instability of the laser in the meter loop system and optimization of deposition parameters, five short tapes (~20 cm coated, ~10 cm measured, 1 cm wide) with I_cs of 265, 276, 292, 298, and 319 A (J_cs of 0.9 to 2.2 MA/cm^2) at 75.5 K were produced. Longer length samples had self field I_cs of (1) 173 A over 79 cm and (2) (Fig. 39a 175 A over 72 cm and 233 A over 54 cm. A thicker 4.3 μm film (Fig. 39b) showed much higher currents than were achievable previously. The J_c values of these longer tapes are quite comparable to that of batch-processed bridges, as indicated by the data shown in Fig. 40.

To summarize, ion-milling experiments showed that thinned films and as-deposited films have the same J_c vs. thickness dependence. They also revealed no adverse effect of substrate elements diffusing into the YBCO, suggesting that barrier and buffer layer thicknesses can be reduced. It was discovered that the porosity problems found in thick YBCO on IBAD YSZ do not exist with IBAD MgO; and it is believed this is due to the smoother substrate surface used for the latter. Therefore, it is no longer necessary to use the Y-Sm multilayers for thick, high-current films. Many thick film bridge samples on IBAD MgO were produced with I_c(H∥c) > 300 A/cm-width, and the best result of I_c(H∥c) = 720 A/cm-width (4.5 μm, 1.6 MA/cm^2). A 5 μm thick film with a J_c of 1.2 MA/cm^2 @ 75 K was measured in pumped liquid nitrogen, with a result of I_c(sf, 65 K) = 1000 A/cm-width.
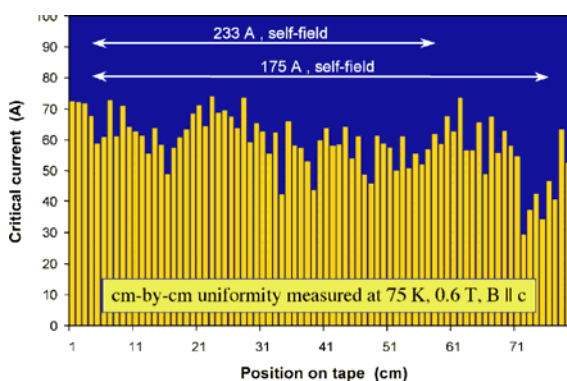
Fig. 39a. Critical current as a function of position for at 0.6 T for a YBCO / MgO IBAD tape.
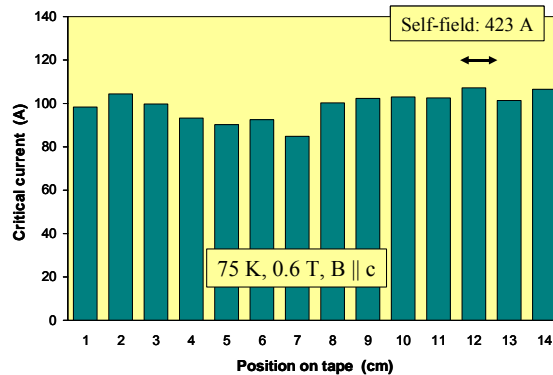
Fig. 39b. I_c at 0.6 T for a 4.3 μm thick film as a function of position. A short section of the tape had a measured self field I_c of 423 A.
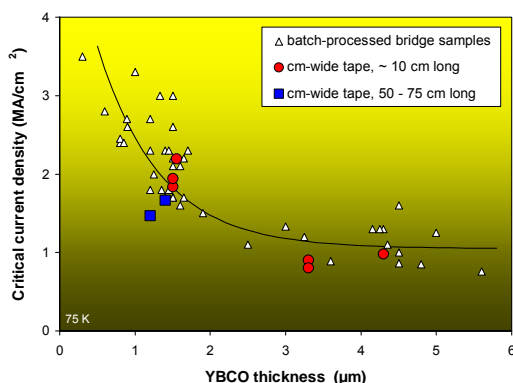
Fig. 40. Comparison of I_cs for cm wide tapes and for batch processed bridge samples.

Future work will be directed at investigating experimentally the fundamental texturing mechanisms of IBAD, with a goal of developing a model that will allow further refinement of IBAD deposition parameters and texture. Another target is, approaching the drop in J_c with thickness as though it is a materials- processing issue and not intrinsic, to maximize J_c through a comprehensive process optimization at a particular thickness with a goal to reproducibly achieve I_cs over 400 A/cm-width at a film thickness of ≤ 1.5 μm. A third goal is to design and implement systematic experiments to determine if chemical modifications to REBCO offer enhanced performance, particularly in an external magnetic field, with the goal to reproducibly double J_c at 75 K in a magnetic field parallel to the c axis.

In conclusion, IBAD MgO is an industrially-scalable process that involves a commercial alloy substrate, electropolishing, and less than 160 nm of deposited material between the metal and YBCO. From microbridges through meter lengths, we are achieving higher YBCO J_cs and higher cm-wide I_cs on IBAD MgO than we ever did on IBAD YSZ. We believe that there remain several areas in which the IBAD MgO structure can be simplified and superconductor performance on IBAD MgO can be enhanced – we will focus on these areas in FY 2004. The first step in transferring IBAD MgO technology to industry was very successful, and this transfer will continue next year.

38

2.1.4 Angular dependence of critical currents in YBCO coated conductors and thin films
L. Civale, J.O. Willis, J.Y. Coulter, A. Serquis, B. Maiorov, S.R. Foltyn, P.N. Arendt,
Q.X. Jia, J. Driscoll-MacManus, H.Wang, and Y. Li

The critical current density J_c of YBCO films prepared by pulsed laser deposition (PLD) on MgO template films prepared by ion beam assisted deposition (IBAD) is now at a level equivalent to those deposited on single crystal substrates. Fig. 41 shows recent Los Alamos data for YBCO on IBAD MgO compared with films deposited on MgO, SrTiO$_3$ (STO), and yttria-stabilized zirconia (YSZ). The numbered data points indicate samples that will be reported on in more detail in this section.
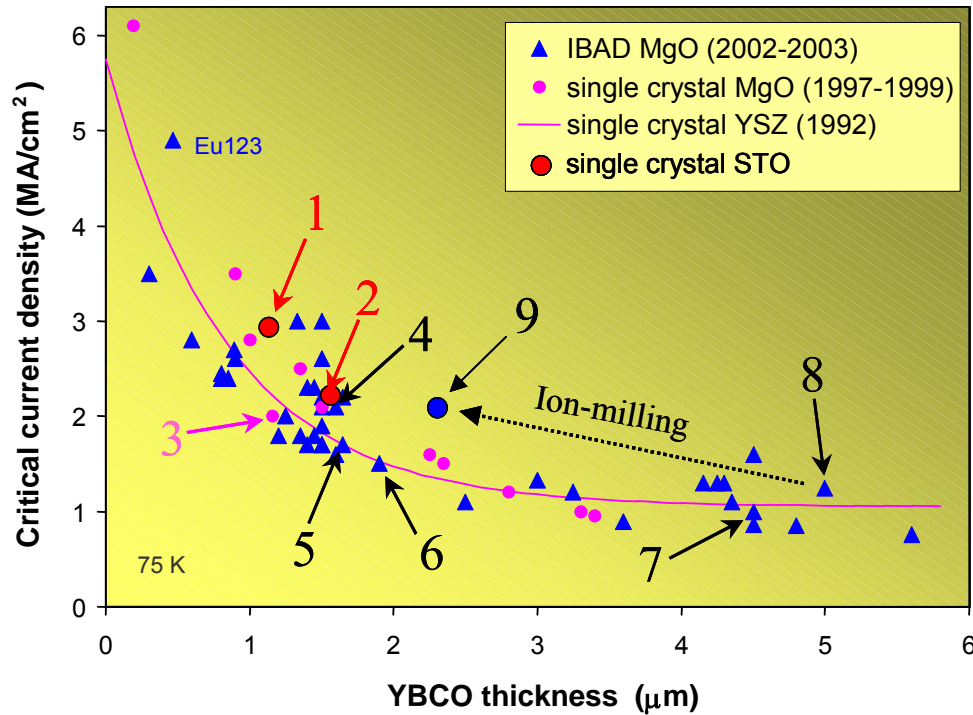
·Fig. 41. Critical current density as a function of YBCO film thickness for YBCO on a variety of substrates. Numbered samples will be discussed and referenced below.

The implication of the equivalence of J_c values for samples on single crystals and on IBAD MgO is that J_c is limited by bulk vortex pinning and that the current flow is uniform. In other words, J_c for films on IBAD MgO is not being limited by weak links and percolative current flow being.

Furthermore, the field, angular, and temperature dependence of J_c of YBCO films on single-crystal substrates and on IBAD template layers (YBCO coated conductors or CC) should provide important information for the investigation and identification of the various pinning sources. In particular, this type of data can help identify pinning from correlated and uncorrelated defects. Comparisons of the pinning for YBCO on single crystal substrates and on template layers prepared by different processes address the question of universality of the pinning mechanisms. One of the most important long term goals of this effort is the investigation of improved in-field J_c by engineering of defects. Some of the questions that must be asked in this effort are (1) how reproducible is $J_c(H,\Theta)$ for a given process; (2) what is the standard or reference material, and (3) which are the useful characterization parameters?

To begin, the coordinate system used for the measurements is shown in Fig. 42a. All of the measurements, unless otherwise noted, were performed at 75.5 K. Fig. 42b shows a

typical data set for sample 2, a 1.55 μm thick YBCO film deposited on single crystal STO, at magnetic field strengths from 0.5 to 7 T. Uncorrelated disorder from random defects plus the effect of electronic anisotropy of YBCO lead to a smooth angular dependence of $J_c(\Theta)$ with a maximum at H//ab. Correlated disorder (extended parallel defects, linear or planar) lead to the additional peaks indicated by the ellipses in Fig. 42b. Near the ab plane, the peaks may be a result of intrinsic pinning and possibly laminar structures. Near the c axis, twin boundaries and grain boundary defects (edge or screw dislocations) may be the source of the extra pinning giving rise to the peak at that position.
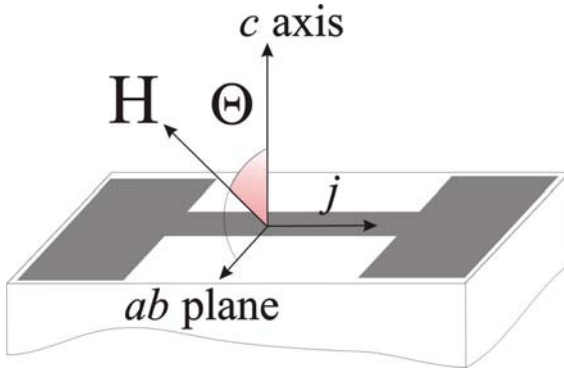
Fig. 42a. Coordinate system used for the anisotropy measurements. $\Theta=0°$ is for the magnetic field along the c axis, and $\Theta=90°$ is for the magnetic field in the ab plane. All measurements were made under the condition of maxium Lorentz force (H⊥J). Unless otherwise noted, all measurements were made at 75.5 K.
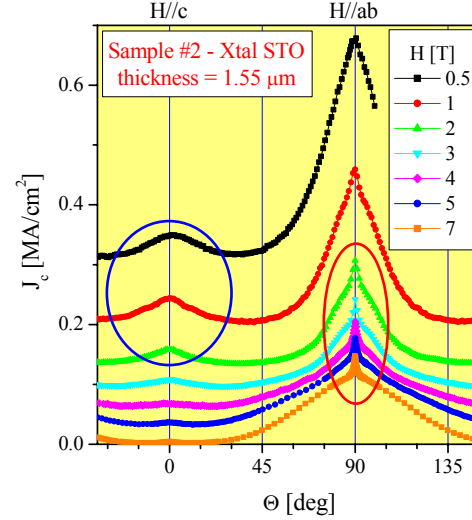
Fig. 42b. J_c as a function of angle for a film on single crystal STO at various magnetic fields. See text for a discussion of the regions in the blue and red ellipses, near 0° and 90°, respectively.

Pinning by uncorrelated disorder as the result of random defects in the lattice coupled with the underlying electronic mass anisotropy of YBCO has been studied by Blatter *et al*. They proposed an anisotropic scaling model (Fig. 43a) in which $J_c(H,\Theta) = J_c[H\varepsilon(\Theta)]$ and $\varepsilon(\Theta) = [\cos^2(\Theta+\gamma^{-2}\sin^2(\Theta)]^{1/2}$ where (the electronic anisotropy) $\gamma=5\text{-}7$. If this model is applicable (if only random defects are present), then J_c should depend only on the scaled parameter $H\varepsilon(\Theta)$. For instance, the model predicts that J_c should be the same for pairs (H,Θ) of (0.5 T, 63°) and (1 T, 82°) both of which are equivalent to $H\varepsilon(\Theta) = 0.24$. These two points are indicated by the arrows in Fig. 43b for the data of sample #2, and indeed the J_c values are identical, demonstrating the appropriateness of the model.
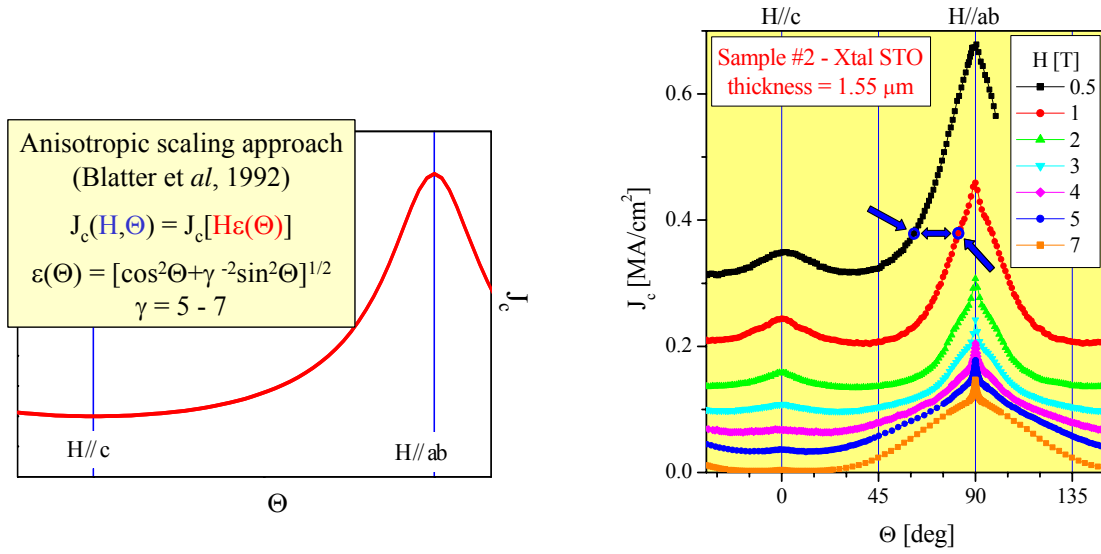
Fig. 43a. $J_c(\Theta)$ according to the anisotropic scaling model of Blatter *et al.*

Fig. 43b. Critical current density as a function of angle at various magnetic field strengths for sample #2. The arrows indicate that the J_c values for two points with the same value of the scaling parameter $H\varepsilon(\Theta)$ are equal, indicating the validity of the model.

For a particular field H, the J_c data as a function of angle Θ may be replotted against the scaled variable $H\varepsilon(\Theta)$. Fig. 44 shows this exercise for sample #2 at 5 T. The upturns at the ends of the data curve in the scaled plot (Fig. 44b) correspond to the peaks in the raw data (Fig. 44a) near H//ab and H//c. If this is repeated for the whole series of magnetic field magnitudes, the resulting set of curves seen in Fig. 44c is the result. Recognizing that the strong deviations from the curves for each field represent deviations from the anisotropic scaling behavior, these are ignored in a fit to the envelope of the set of curves (red line in Fig. 44d). This fitted curve can now be projected back into the unscaled variables of H and Θ. This result is shown in Fig. 44d for sample #2 at 5 T. The difference between the blue (upper) curve of the data and the red (lower) curve represent enhancements in pinning from correlated defects.
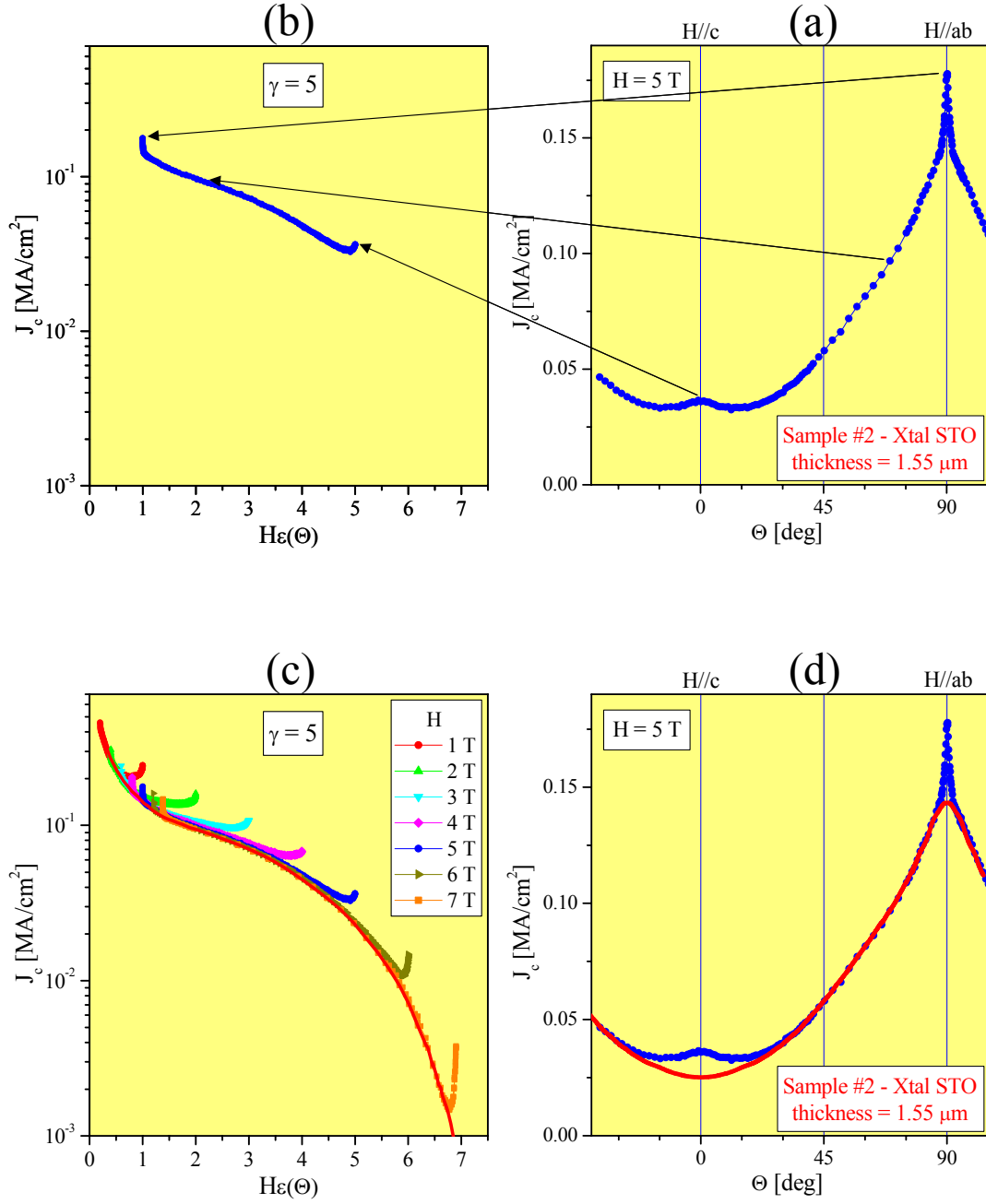
Fig. 44. Counterclockwise from top right: (a) Critical current density as a function of angle (i.e., unscaled) for sample #2 at 5 T; (b) Correspondence of features when J_c as a function of angle is replotted as a function of the scaled variable $H\varepsilon(\Theta)$ for sample #2 at 5 T; (c) Scaled J_c data for magnetic field magnitudes from 1 to 7 T for sample #2. The red line is a fit to the envelope of the curves for all fields; (d) J_c as a function of angle (i.e., unscaled) for sample #2 at 5 T (upper, blue curve) and the projection of the scaled fit of Fig. 5a to J_c vs. angle (lower, red curve).

Focusing on the region near the c-axis peak next, the peak feature can be analyzed by a simple construction: the width w_c is defined as the angular difference between the minima in J_c as shown in the inset to Fig. 45a. The height h_c is also defined and shown in that inset. Both h_c and w_c for sample #3 are plotted in Fig. 45b for all fields measured. Here, the height h_c is normalized to its value at 1 T. At low fields (<~1 T), both the peak height and width increase with H. However, at higher fields, both parameters decrease with magnetic field. The peak height h_c follows an exponential dependence with field and is proportional to $\exp(-H/H_c)$, where H_c is about 1.8 T. While the width also decreases with magnetic field, it does not decrease so drastically, changing from ~80º near the peak to ~40º at 7 T.
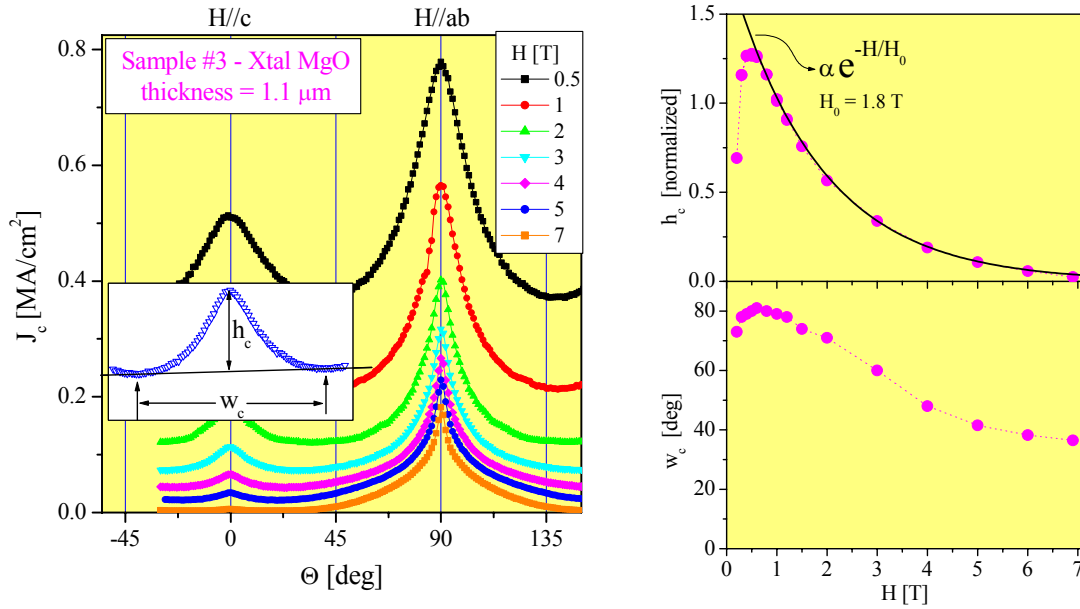
Fig. 45a. J_c for sample #3 on single crystal MgO as a function of angle for the magnetic fields shown. The inset shows the peak feature near the c axis. The height and full width of this peak are defined in the inset.

Fig. 45b. Normalized c-axis peak height h_c [$h_c(1\,T)$ = 1] and peak width w_c as a function of magnetic field for sample #3. Above about 1 T, h_c can be fit with an exponential as shown.

Comparing these data for sample #3 and this same analysis for sample #8, a 5 μm thick film on MgO IBAD, and sample #9 (sample #8 ion milled to 2.35 μm), it is apparent that both the unscaled data in Fig. 46a and the analyzed c-axis peak data in Fig. 46b are quite similar for each of these three samples.

Fig. 47 summarizes the c-axis peak characteristics for eight YBCO films on single crystal and IBAD MgO substrates with thicknesses ranging form 1 to 5 μm, including one ion milled sample. The (normalized) height and the width have essentially the same field dependence for all samples. This implies that the same type of correlated defects must be acting in all cases. Differences in the true (unnormalized) height indicate variations in defect density among the samples. All samples show a crossover in field dependence as a peak near 1 T.
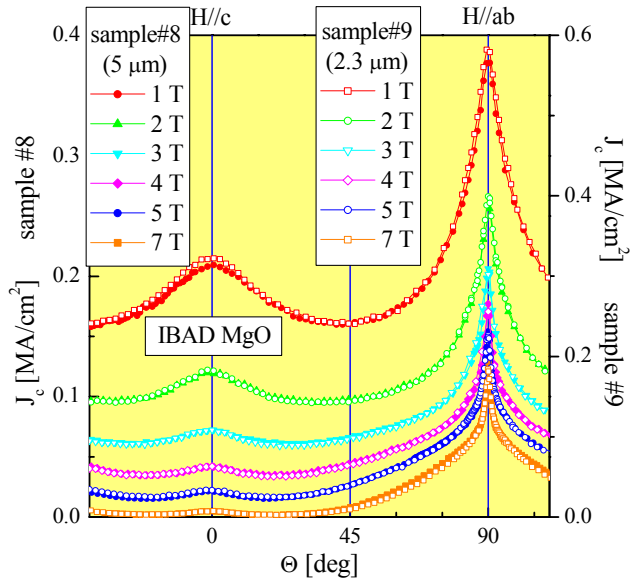
Fig. 46a. J_c for samples #8 and 9 (#8 thinned by ion milling) on IBAD MgO as a function of angle for the magnetic fields shown.
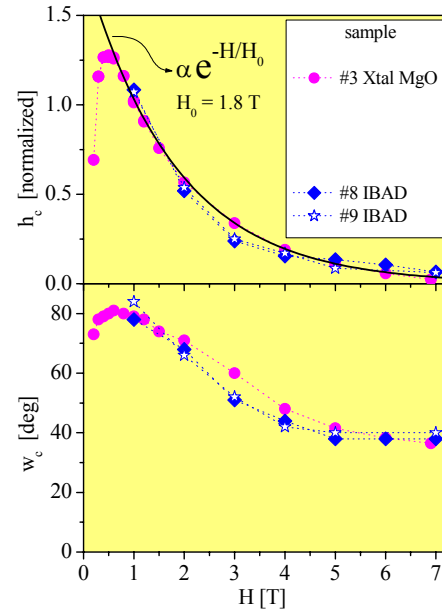
Fig. 46b. Normalized c-axis peak height h_c and peak width w_c as a function of magnetic field for samples #3, 8 & 9. The data for all three samples are quite similar.
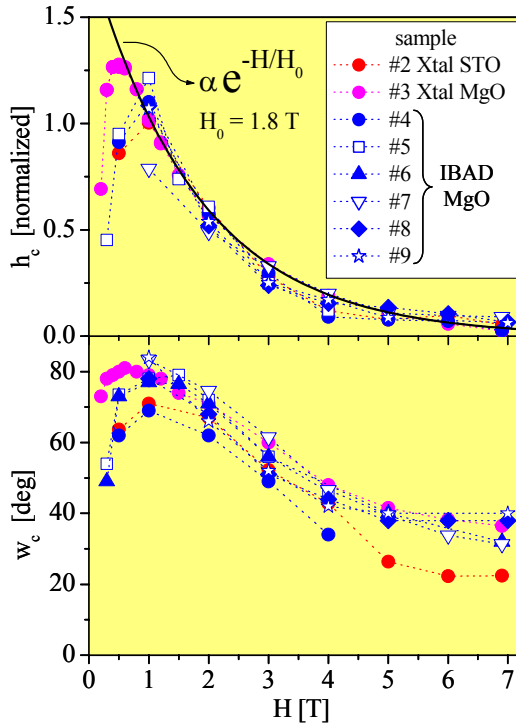
Fig. 47. c-axis peak height and width as a function of magnetic field for 8 different YBCO samples on both single crystal and IBAD MgO substrates.

44

Now focusing attention on the intrinsic pinning peak associated with the ab planes, a very sharp peak in J_c above that predicted by the anisotropic scaling model is apparent (Fig. 48) when the magnetic field is very close to the ab plane. A well-known pinning source near the ab planes is the intrinsic pinning associated with the periodic modulation of the order parameter, which arises from the layered structure of YBCO. (In addition to this mechanism, pinning by extended defects in the ab plane, such as film-substrate or intergrowth layers, may also contribute to the correlated pinning.) As H is progressively tilted away from the ab planes, the vortex lines first remain locked along the ab planes (Fig. 48a, left side of inset), then begin to form "staircases" with ab segments connected by kinks to ab segments in adjacent ab planes. Eventually, as the angle becomes large enough and exceeds the "trapping angle," the effect of the ab plane intrinsic pinning becomes very small, and J_c decreases to the anisotropic scaling level. The full width at half maximum (FWHM) of the peak is w_{ab}, and is a very small 3º at 7 T. The intrinsic pinning effects should be spread out over an angular range at least as large as that of the out of plane mosaic spread $\Delta\omega$ shown schematically in Fig. 48a, right side of inset. This value is 0.29º for sample #2 (Fig. 48b).
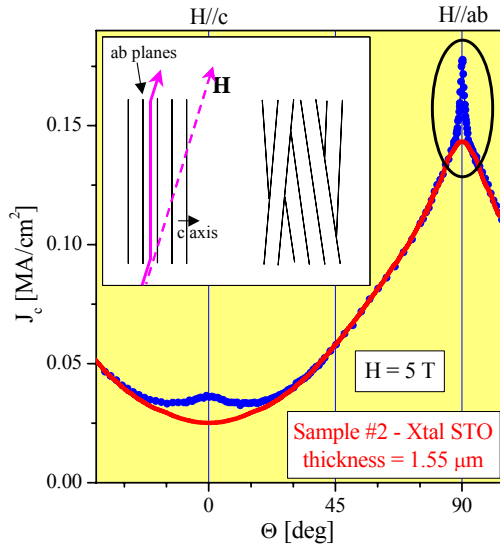
Fig. 48a. J_c as a function of angle at 5 T for sample #2 showing the very sharp ab plane peak. The inset shows (left) how the vortex lines tend to lock into the ab planes for values of Θ close to 90º and (right) the ab planes with a small mosaic spread.
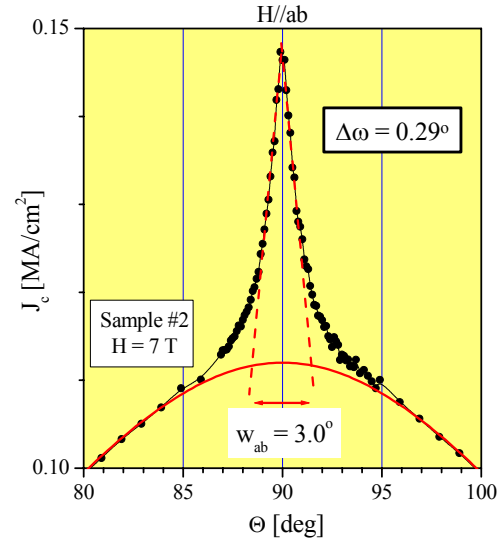
Fig. 48b. J_c as a function of angle for sample #2 at 7 T near the ab plane peak, showing the very sharp intrinsic pinning peak of width $w_{ab} = 3.0$º and the mosaic spread $\Delta\omega=0.29$º.

Examining the ab plane peak for a variety of YBCO films (Fig. 50a) deposited on both single crystal substrates and IBAD MgO, it is clear that this feature occurs in all samples. As noted above, it is expected that there should be a correlation between w_{ab} and the mosaic spread $\Delta\omega$ with $w_{ab} >= \Delta\omega$. Indeed, this is the case for YBCO deposited on a variety of substrates (Fig. 50b). There is a minimum value for w_{ab}, of about 4º as $\Delta\omega$ approaches zero, indicative of the value of the trapping angle. However, as $\Delta\omega$ increases above about 1 to 1.5º, w_{ab} begins to increase rapidly and the correlation between the two parameters becomes apparent. The absence of any systematic differences in the angular dependence of J_c between the films on single crystals and on IBAD strongly suggests that the correlated defects are similar in all these PLD films.
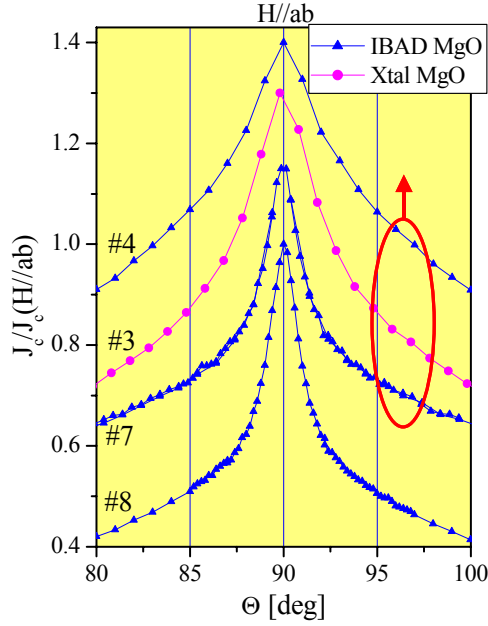
Fig. 49a. Normalized ab plane peak feature (curves are displaced for clarity) in J_c as a function of angle for samples on IBAD MgO and single crystal MgO.
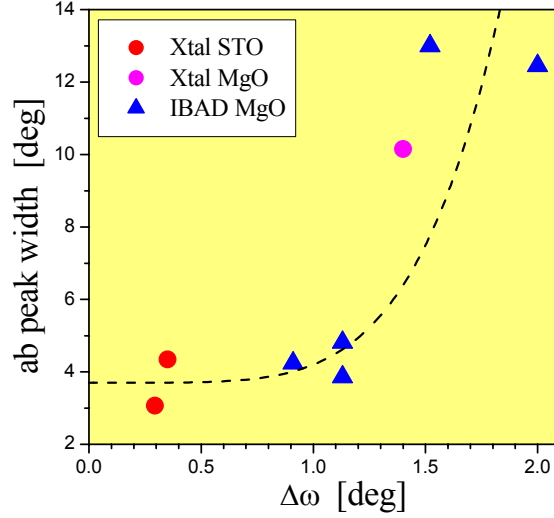
Fig. 49b. Correlation of ab plane peak width as a function of the out of plane mosaic spread $\Delta\omega$ for YBCO on single crystal substrates and IBAD MgO.

Summarizing the results thus far, the reproducibility among the samples made by the same process is good, and samples of different types have overall similar angular dependences. The main sources of vortex pinning and the various angular regimes have been identified. The angular dependence of the contribution of random defects to J_c can be described using an anisotropic scaling model. The c-axis peak arises from correlated disorder, such as twins and grain boundaries, and was analyzed in terms of the angular width and normalized peak amplitude; these follow a universal field dependence for PLD YBCO. An additional ab plane peak due to intrinsic pinning appears in all measured samples; the peak sharpens as the out-of-plane texture of the film $\Delta\omega$ decreases.

Finally, comparing the $J_c(H,\Theta)$ for PLD films deposited on single crystal substrates and on IBAD MgO (Fig. 50a) normalized to the self field values $J_c(sf)$ to account for the effect of film thickness, the qualitative shape is quite similar. Also, films #2, #3, #4, and #9 have the same $J_c(sf)$ within 20%, so that the comparison in Fig. 50a for these samples is essentially quantitative for J_c. Fig. 50b shows a similar comparison for the same samples at 3 T. For reference purposes, the samples' $J_c(sf)$ and thicknesses are shown in Fig. 41.

Looking just at the four samples with similar $J_c(sf)$ (Fig. 51), it is clear that the films on IBAD MgO have a higher J_c, compared to those on single crystal substrates, over most of the angular range. This is true at 1 and 3 T (Figs. 51a and 51b, respectively) and generally at higher fields also. Structure evidence (x-ray line broadening) indicate that there are about five times more threading screw type dislocations for YBCO on IBAD MgO relative to on single crystal MgO. Also, Rutherford backscattering channeling indicates that films on IBAD have more point defects and larger misorientation. These extra defects in the films on IBAD result in stronger vortex pinning and improvements in J_c relative to that on single crystal substrates.

46
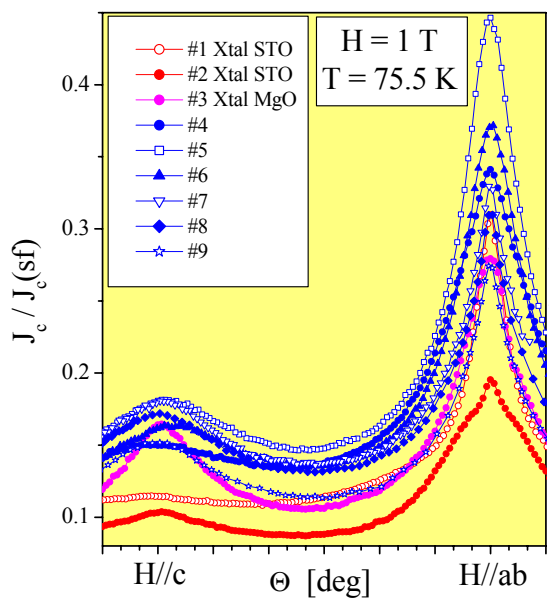
Fig. 50a. Normalized J_c as a function of angle for all measured samples at 1 T.
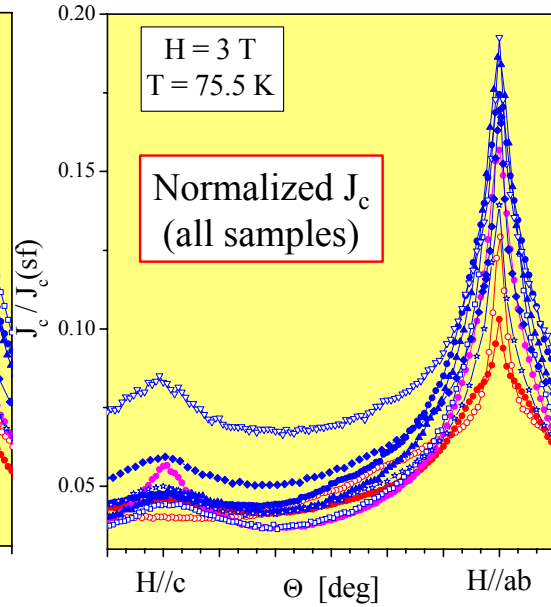
Fig. 50b. Normalized J_c for all measured samples at 3 T. The legend is the same as for Fig. 50a.
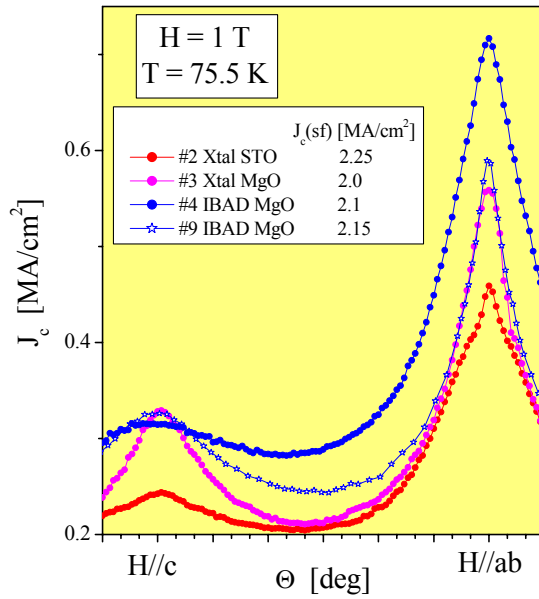
Fig. 51a. Comparison of J_c as a function of angle at 1 T for films on single crystal and IBAD MgO.
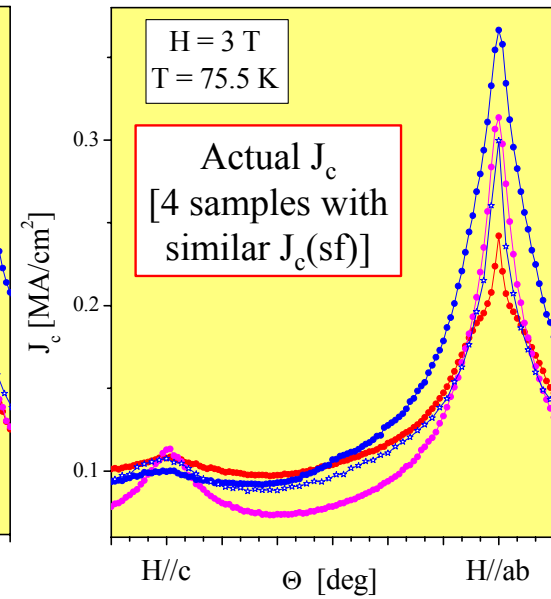
Fig. 51b. Comparison of J_c as a function of angle at 3 T for the same samples shown in Fig. 51a.

Summarizing the results of this part of the study, the PLD YBCO / IBAD MgO coated conductors were found to have higher J_c than the films on single crystals over extensive ranges of magnetic field intensity and orientation. The extra pinning probably arises from: additional random defects (larger RBS reflectivity); additional c-axis correlated defects: more screw dislocations at low-angle grain boundaries, slightly higher in-plane mosaic $\Delta\phi$, sub-grain structures; and additional correlated structures parallel to the ab

planes (higher out-of-plane $\Delta\omega$). There is room for further pinning improvement in CC through microstructural engineering, and the pinning optimization will be application dependent (temperature, magnetic field angle and direction, etc.).

Future plans include the extension of transport measurements and analysis to lower temperatures with the goal of identifying pinning sources and angular regimes in the temperature range 75 K < T < 26 K (liquid Ne). Films thinner than 1 μm will also be studied with the goal of determining whether the main pinning sources in those films with J_c > 4 MA/cm^2 are still the same. The angular dependence of J_c will be explored in CC with different architectures with the goal of determining how the relative importance of the pinning mechanisms identified in IBAD MgO change depending on the microstructure. J_c measurements will be performed with current flowing in different directions in the plane with the goal of exploring the in-plane anisotropy of the c-axis correlated disorder, to determine whether the defects are linear or planar. HTS films with rare earth substitutions will be grown with the goal of searching for pinning enhancements by introduction of random defects. Finally, columnar defects will be introduced at different angles in YBCO films on single crystal substrates with the goal of measuring the angular dependence of J_c in samples with a controlled defect structure, for comparison with the CC.

2.1.5 Coated conductor development: substrate and template layers

V. Matias, B.J. Gibbons, L. Civale, S. Kreiskott, A.T. Findikoglu, P. te Riele, C.J. Sheehan, L.E. Bronisz, S.R. Foltyn, P.N. Arendt

The role of the Superconductivity Technology Center (STC) facility at the Los Alamos Research Park (RP) is to form a bridge between the small sample research performed within the core program at the STC and the scale up needed by industry for manufacturing. It has been two years since the inception of the RP project, and all systems are operational and productive. Major tasks have been: to scale up the coated conductor (CC) fabrication and characterization processes using reel to reel tape transport systems; to increase interaction with outside collaborators, to provide process specifications to industry (possible architectures, inputs for cost analysis, etc.); to provide new *in situ* diagnostic capabilities; and to provide a unique facility that is available to outside users.

The coated conductor architecture used in the fabrication process is the one developed by the core program and is illustrated in Fig. 52. The substrate for the CC is a Ni-based superalloy, Hastelloy C-276, that is electropolished. This is followed by deposition of a nucleation and barrier layer. A biaxially textured layer of MgO is then produced using ion beam assisted deposition (IBAD). This is followed by an epitaxial layer of MgO. Additional buffer layers and the YBCO HTS layer are produced by pulsed laser deposition (PLD) and finally overcoated *in situ* with a layer of sputtered silver.

Ag layer
YBCO
Epi buffer layer(s)
IBAD-MgO layer
Nucleation layer (Y_2O_3)
+ barrier layer (Al_2O_3)
Ni superalloy
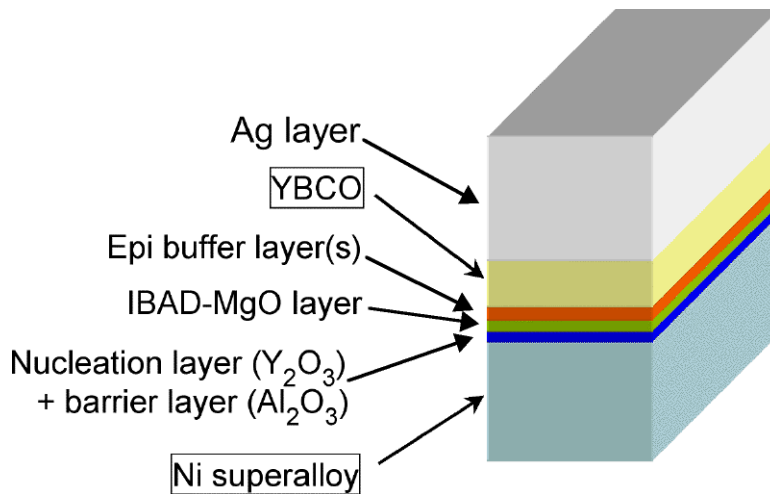
Fig. 52. Coated conductor architecture used for reel to reel scale up process.

Some of the achievements over the past year include the electropolishing of more than 2 km of tape; the processing of 100's of meters of IBAD-MgO tape in continuous pieces > 10 m with in plane mosaic spread of < 8º full width at half maximum (FWHM); the processing of 10's of meters of YBCO by PLD; and the providing of many samples to collaborators.

The first stage in the production of CC is the electropolishing of the substrate. Previously, good surface finishes were obtained on Hastelloy C-276 with the as-delivered system, shown in Fig. 53a. However, the electrical contact brushes, as delivered from the equipment supplier, and rollers, as modified at LANL, can often scratch the tape surface (Fig. 53b).

Fig. 53a. Electropolishing system for substrate polishing
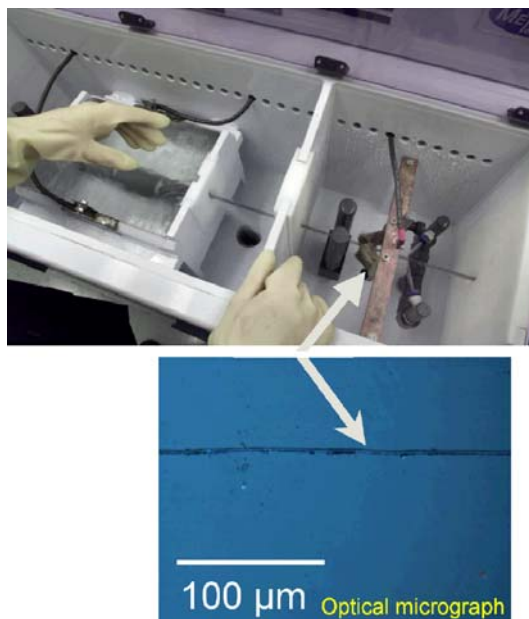
Fig. 53b. View of contact brushes (top) and scratches on tape surface from those brushes.

The system was then modified to utilize a bipolar setup for electropolishing, as shown in Fig. 54. As Fig. 54a indicates, there are no mechanical contacts to the sample; electrical contact is provided by the electrolyte solution. This system provides even better polishing results than the original one with mechanical contacts and without any scratches.
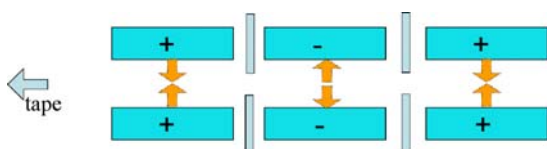
Fig. 54a. Schematic of the bipolar polishing system.

Fig. 54b. Top view of the polishing cell showing the 3 compartments and electrode leads.

The polishing process has a relatively wide processing window and is quite rapid, resulting in a smooth finish in ~30 s. The rms roughness is typically <0.5 nm for a 5 x 5 μm area. The electropolisher is usually run at a speed of 20 cm/min or 12 m/h using two 10 cm long cathodes. It is expected that these polishing results can be extrapolated to tapes up to 10 times wider (10 cm) and with more electrodes, e.g., 8 times, to increase throughput. Extrapolating both these factors leads to an equivalent throughput of 1 km/h of 1 cm wide tape, the speed which we believe is necessary for economical production of coated conductors.

4 sec

28 sec

12 sec

100 μm
34 sec

20 sec
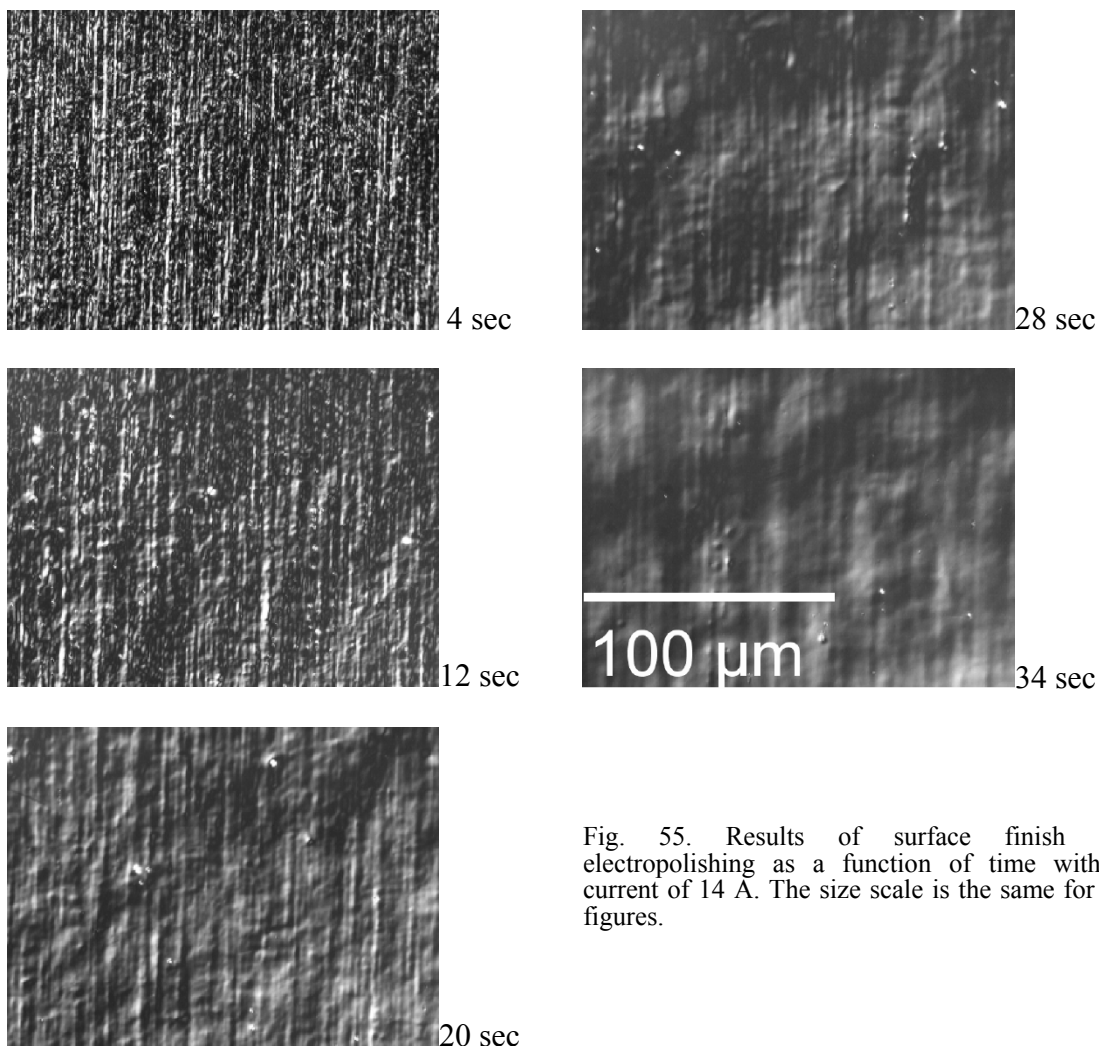
Fig. 55. Results of surface finish for electropolishing as a function of time with a current of 14 A. The size scale is the same for all figures.

The next steps in producing a coated conductor are the depositions of the barrier, nucleation, and template layers (Fig. 52). In transferring the IBAD process from our small-scale research program to the CC scale up program, the texture of the IBAD -MgO template layer was initially found to be poorer (8º vs. 12º, respectively). We investigated the possible causes that could affect the IBAD texture in detail, including ion beam divergence, ion to molecule ratio, IBAD layer thickness, and the nucleation layer. Some of these parameters had already been studied in the small-scale program, but we needed to see how they transferred to our new system (Fig. 56) using e-beam MgO evaporation.

Fig. 56. Photograph of the Ion Beam Assisted Deposition chamber.

51

We first examined the divergence of the ion beam. The divergence can be measured using the method of sputtering a multilayer film through an aperture [Ref. Kaufman]. Variations in the depth of sputtering indicate the spread of the ion beam as shown in Fig. 57a and b. The beam is known to be broad in the as-supplied source, which we measured to be 25º along the length of the source, and 11º across the width, as shown in Fig. 57c. This tool can be used to track modifications to optimize divergence. Fig. 57c shows the measured divergence of the ion beam in the x (in the tape direction) and y direction (perpendicular to the tape). Using a series of parallel plates to collimate the ion beam we were able to obtain a 2º beam divergence. However, the ion beam divergence reduction was found to improve the texture only marginally, (Fig. 57d) from 3.5º FWHM in plane and 2.5º out of plane without collimation, to 3º in plane and 2º out of plane with collimation.
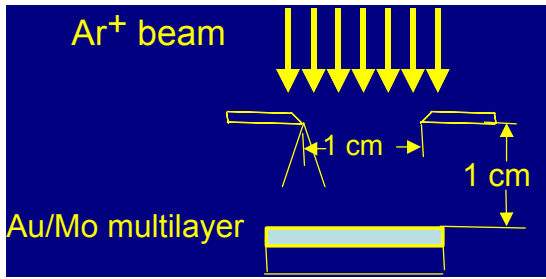
Fig. 57a. Measurement tool for Ar ion-beam divergence.
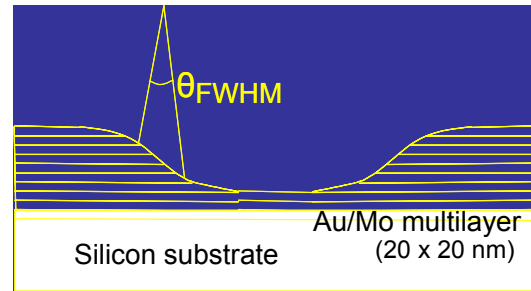
Fig. 57b. Ion sputtering of multilayer as a function of angle from normal.
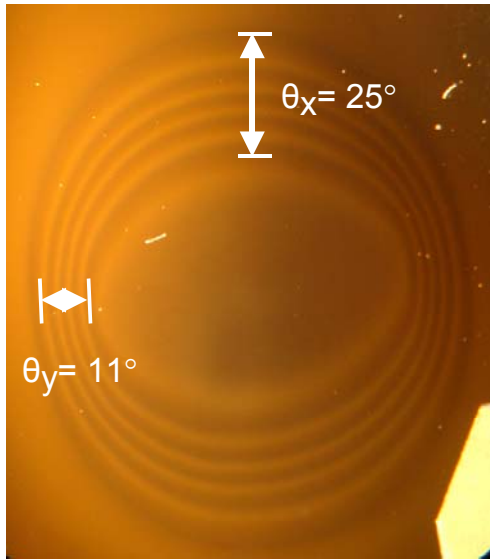
Fig. 57c. Ar ion beam divergence determined from fringes in multilayer film.
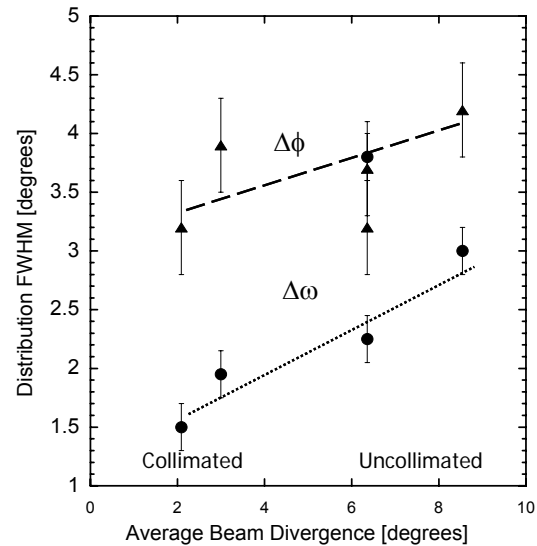
Fig. 57d. In plane and out of plane texture as a function of beam divergence.

However, the Ar ion to MgO molecule ratio was found to be the most critical parameter affecting our in-plane texture. As this ratio is increased over the range 0.6 to 1.3, the in-plane texture improves from 9.5º to about 3.5º; however, the ratio of ion-etched to deposited MgO film thickness also increases. At a ratio of 1 or above, essentially no MgO film is deposited, thus there is a trade off between ion/molecule ratio and in-plane texture; the results are shown in Fig. 58.
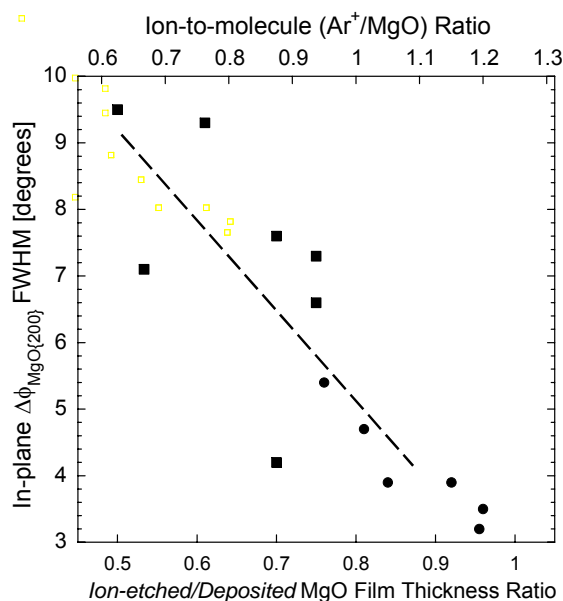
Fig. 58. Variation of MgO in-plane texture as a function of ion to molecule ratio for IBAD MgO.

The IBAD process has now been successfully transferred from the core research program to the CC processing program at the RP. Current production quality is 6-7º in plane FWHM textured IBAD tape in > 5 m lengths; without the Al_2O_3 barrier layer, the texture is 4-5º. The key process parameters to obtaining good texture are understood, but there are still some unanswered questions. Surface control and the right nucleation layer are key. *In situ* diagnostics, such as reflection high-energy electron diffraction (RHEED), are very helpful. A new *in situ* system to be use for surface characterization in the IBAD chamber is a time-of-flight ion scattering and recoil spectroscopy (TOF-ISARS) system made by Ionwerks, Inc. (Houston, TX). This company provided initial characterization of IBAD-MgO samples. A small amount (<1%) of Cu was found on the surface of the MgO and some Al from the Al_2O_3 barrier layer is present on the surface of a heated Y_2O_3 nucleation layer (Fig. 59). These data show the extreme surface sensitivity of this analytical tool. The TOF-ISARS will be installed in the IBAD system during FY2004.
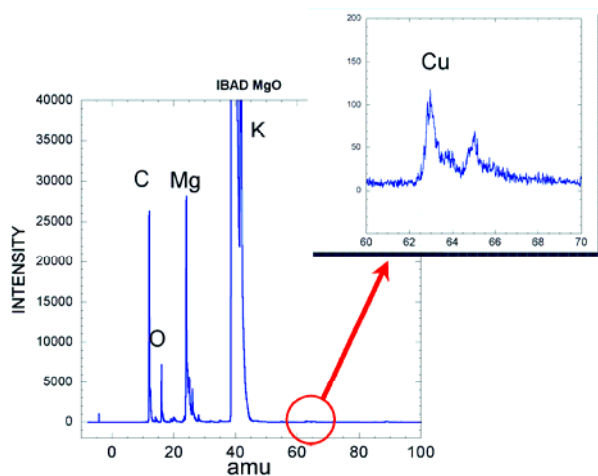
Fig. 59a. A small amount of Cu is present on the surface of IBAD MgO by TOF-ISARS.
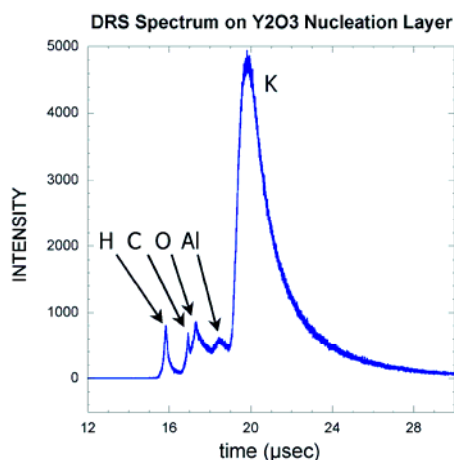
Fig. 59b. Al from the Al_2O_3 layer is present on the surface of the Y_2O_3 layer.

53

Our IBAD process is controlled with the use of two quartz crystal monitors (QCM) for measuring IBAD deposition rates. One QCM monitors only the MgO deposition rate (it is shielded from the Ar ion beam, and the second monitors both the net (deposition - etch) deposition rate (Fig. 60). With this control, stable depositions over 10 m can be achieved. Typically, ±5% variations in rate result in less than 0.5º difference in in-plane texture and a robust deposition process.
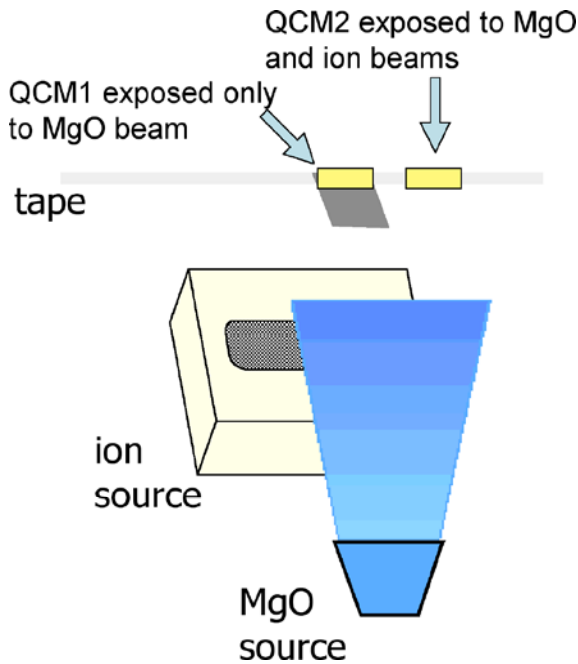
Fig. 60. Deposition monitoring system for IBAD MgO using two quartz crystal monitors.

It has been known from previous work that it is possible to rework "bad" regions of IBAD tape. The presence of a bad region can be determined by use of *in situ* RHEED or another *in situ* diagnostic. Once the bad region has been identified, the deposited layers can be removed, and a new nucleation layer and IBAD layer deposited. Here we demonstrated for the first time that a repaired region can be seamlessly connected to existing IBAD. Fig. 61 shows the RHEED images for good and bad regions and the "seams" at the edges of the repaired region showing good intensities, indicating high quality of the texture and the efficacy of such a repair process.
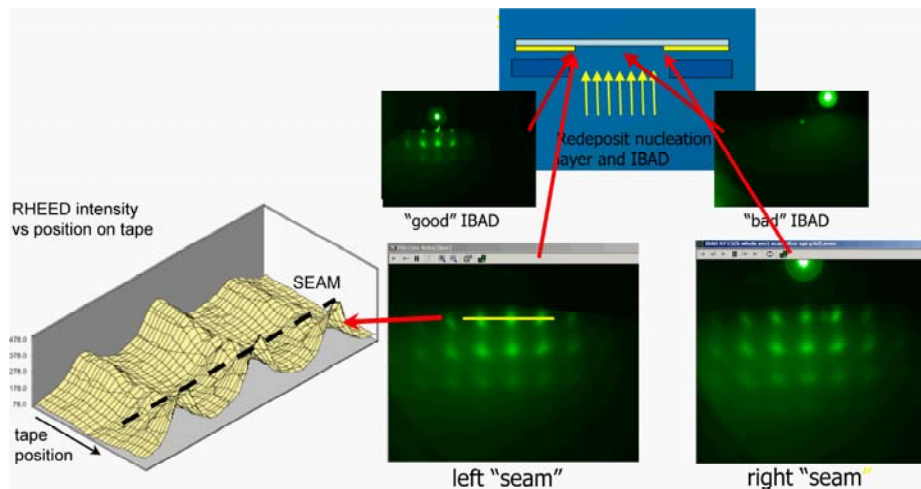
Fig. 61. RHEED patterns of the bad and good regions, of the good quality of the RHEED images at the edges "seams" of the repaired region, and RHEED intensity as a function of position near one of the seams.

One major goal of the RP CC processing program is to increase the speed of the IBAD MgO process. The normal deposition speed is 5-10 m/h, or about 2 mm/s. To scale the process to higher rates, the Ar ion current was increased to its maximum of ~320 mA, given the present ion beam source in the IBAD scale up system. The MgO deposition and tape speed were adjusted accordingly, by a factor of 5. The resultant template layer produced at 36 m/h and limited by the ion gun in the chamber still had very good texture: 4.5º in-plane and 1.4º out of plane. The very sharp peaks in the MgO pole figure and φ-scan intensities for this tape are shown in Fig. 62. Extrapolating to a 50% longer deposition zone and tape 5x wider (5 cm), to use the ion gun more efficiently, yields a rate of 250 m/h of 1 cm wide equivalent tape. With four ion guns placed in series, the throughput is calculated to be 1 km/h of 1 cm wide tape, reaching the necessary benchmark for economic large scale production.
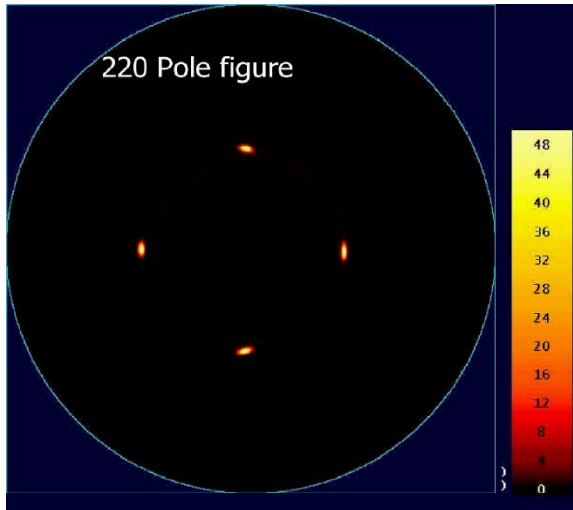
Fig. 62a. Pole figure of MgO 220 peaks for high deposition rate IBAD MgO.
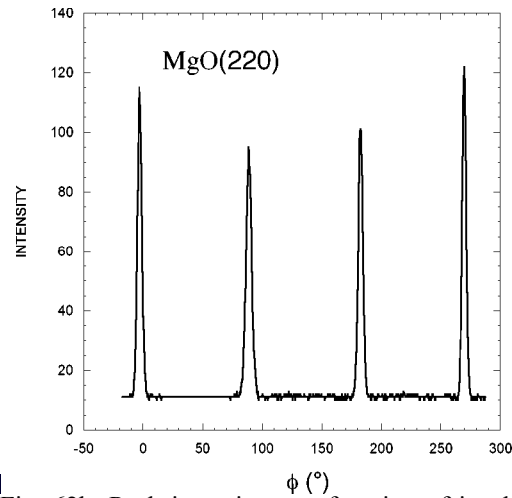
Fig. 62b. Peak intensity as a function of in plane angle, φ. The peak FWHM is ~4.5º.

Following deposition of the template layer, the next step is the deposition of buffers and YBCO. Pulsed laser deposition (PLD) has demonstrated the highest critical currents to date (Göttingen, Fujikura, LANL), with the best results over 400 A/cm-width. PLD is the easiest deposition system to set up quickly, and it is very versatile. However, it is useful to explore other deposition processes, particularly other *in situ* processes. Reactive co-evaporation could be a good candidate for an inexpensive CC production line. This process has been widely employed for the production of HTS electronic devices. To that end, a co-evaporation system is to be installed at the Los Alamos RP. The system (Fig. 63) uses a single electron beam gun with computer controlled scanning. Laser atomic absorption spectroscopy is used for accurate rate control.
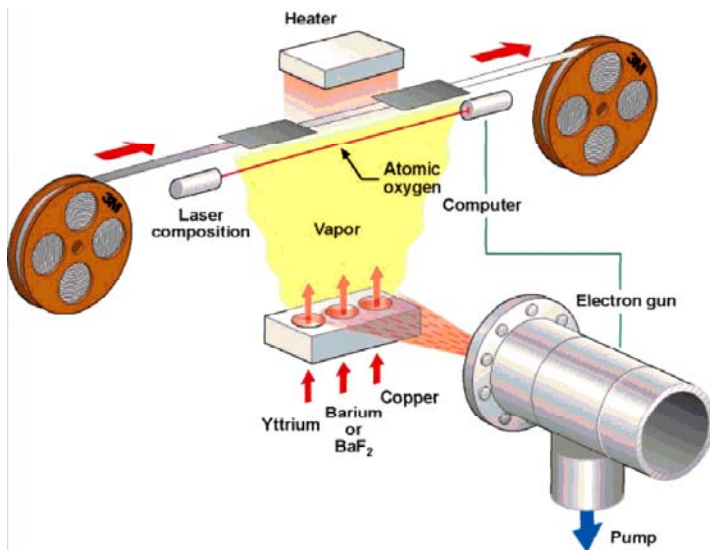
Fig. 63a. Schematic of coevaporation system.

Fig. 63b. Coevaporation system (left) and laser atomic absorption system (right).

Summarizing the substrate preparation IBAD-MgO performance, the bipolar electropolishing system has been set up and produces <1 nm RMS surface roughness in over 100 m lengths of tape. Hundreds of meters of electropolished tape have been supplied to industrial partners. IBAD MgO in-plane texture is typically 6-7º, with champion values of 4-5º FWHM. Lengths of >5 m have been prepared with in-plane texture of 6º FWHM; the longest single continuous IBAD length was 12 m. (PLD YBCO on the RP IBAD tape has produced >170 A in short lengths and 50 A for >1 m lengths.) Several meters of IBAD tape have been supplied to industrial partners. High rate IBAD-MgO has been demonstrated at 36 m/h with in-plane texture of 4.5º FWHM. Proof of principal for IBAD repair has been demonstrated.

Future work includes providing IBAD-MgO to collaborators in lengths >10 m with in plane texture <8º FWHM. The ion scattering capability will be added to the IBAD processing chamber and will be used for optimization of the diffusion barrier. The IBAD repair process will be developed in more detail with respect to optimization of the HTS layer by maximizing I_c across the repaired region to 80% or better of the average I_c. Reactive co-evaporation of the YBCO will be implemented with a goal of producing a 1 m length with I_c>100 A at 75 K.

2.1.6 Coated conductor development: pulsed layer deposition of YBCO

B.J. Gibbons, S. Kreiskott, V. Matias, C.J. Sheehan, L.E. Bronisz, S.R. Foltyn, P.C. Dowden, X. Liao, and T.G. Holesinger

After the polishing of the raw substrate and the deposition of the various layers in the ion beam assisted deposition chamber, i.e., up through the IBAD MgO layer and homoepitaxial MgO (Fig. 64), the tapes are transferred to the reel to reel pulsed laser deposition (PLD) chamber for deposition of further buffer layers, the YBCO, and the silver layer.

Fig. 64. Coated conductor architecture used for reel to reel scale up process.
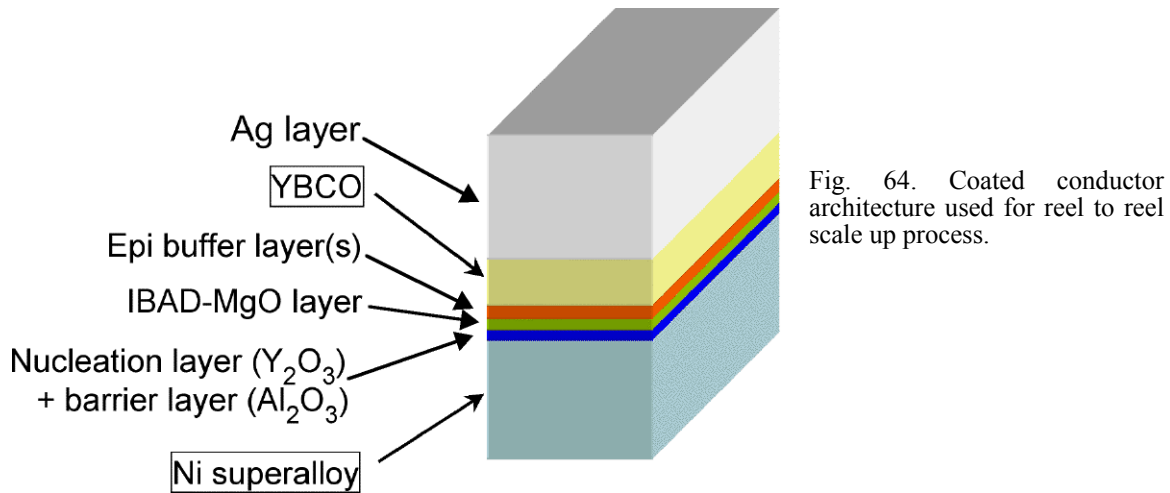
The chamber is shown in Fig. 65. The laser employed is a 200 W XeCl (308 nm) excimer laser capable of a 650 mJ pulse at a 300 Hz rate. Four 4" targets are available on the target manipulator for deposition of a variety of oxide layers. The system can handle sample lengths from 1 cm (by attaching to a carrier tape) to 10's of meters. A quartz lamp heater heats the tape as it moves continuously through the PLD zone. The tape may be moved *in situ* with respect to the laser plume to optimize plume alignment. After the HTS layer is deposited, a silver overlayer to protect the surface and to provide good electrical contact to the tape can be deposited by dc magnetron sputtering.

Fig. 65. Schematic of the Pulsed Laser Deposition chamber.
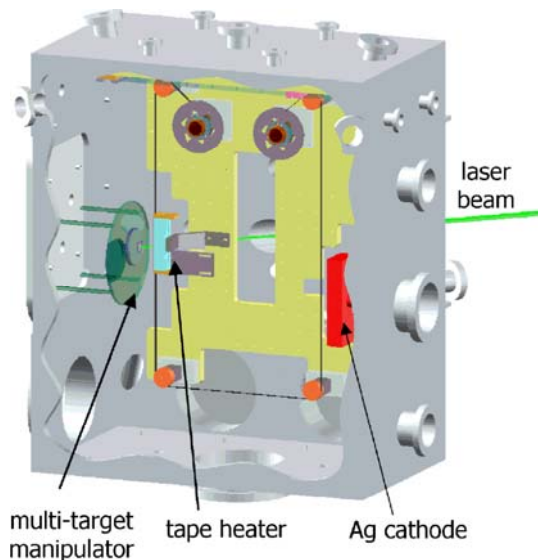
Buffer layer deposition takes place on top of the IBAD MgO template layer produced in the previous steps. The buffer layer used in this step is $LaMnO_3$ (LMO). LMO has the gadolinium ferrite structure, which can be indexed as a pseudo-cubic perovskite (Fig. 66a). When indexed this way, the (110) family of planes becomes the $(100)_{pc}$ with a spacing of 0.3985 nm, providing for an excellent lattice match with YBCO. In addition, LMO can be made as a very dense target, providing for a very stable deposition environment. Other advantages include a very wide processing window and a relatively low deposition temperature (650 – 750º C). The LMO is deposited epitaxially on the MgO IBAD layer as shown in Fig. 66b. The high deposition rate in PLD of 0.1 nm/shot allows tape speeds of up to 21 m/h for a 100 nm thick layer on the 1 cm wide tape. Fig. 67 shows that growth morphology of the LMO is columnar and that the interface between the LMO and the epitaxial MgO is clean and smooth. The surface (Fig. 68a) of the LMO films is smooth with a grain size of ~10 nm. The in-plane texture (Fig. 68b), as determined by the full-width-at-half-maximum (FWHM) of the $(011)_{pc}$ peak width in an x-ray φ scan of the LMO is improved over that of the underlying MgO layer by ~1 to 2º
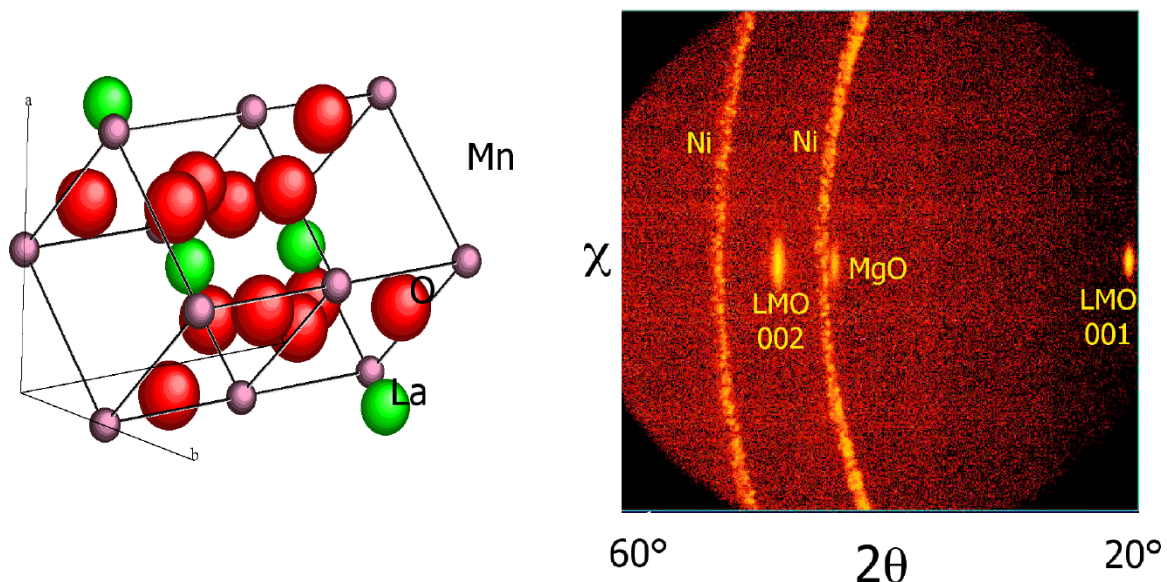
Fig. 66a. Molecular structure of the $LaMnO_3$ pseudo-cubic perovskite.

Fig. 66b. X-ray diffraction scan showing the epitaxially aligned $LaMnO_3$.
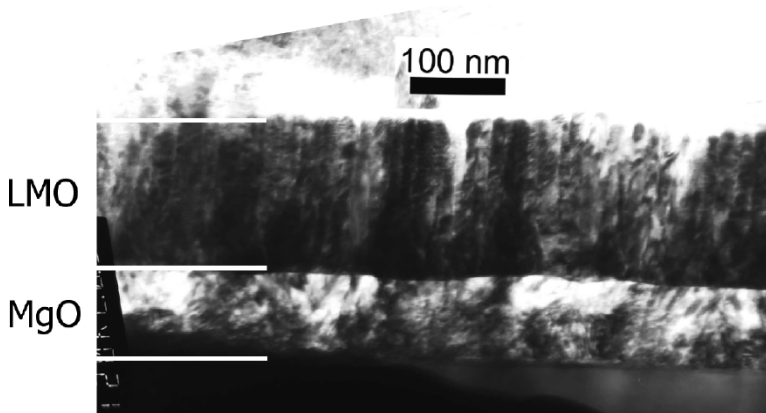
Fig. 67. The smooth LMO/.MgO interface and the columnar growth morphology of the LMO.

58
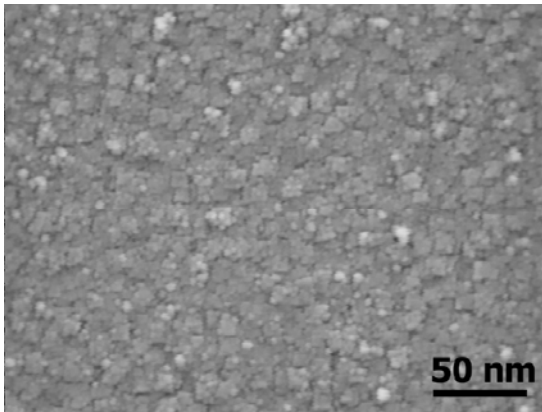
Fig. 68a. Micrograph of the smooth surface of the LMO buffer layer.
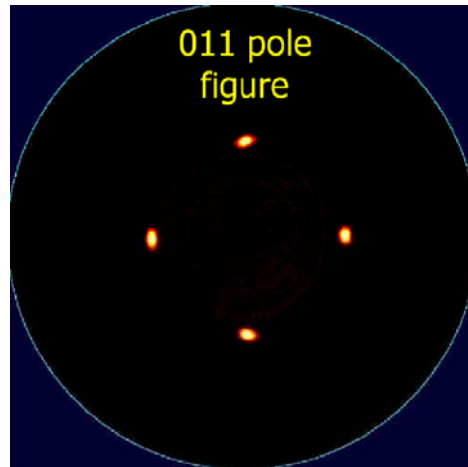
Fig. 68b. LMO shows high degree of in-plane texture.

The YBCO deposition takes place with the substrate at an elevated temperature in the 750-825 °C range. The substrate is radiatively heated using the 30 cm long quartz lamp heater. The temperatures quoted here are those from the heater thermocouple, not the tape itself. Since this thermocouple is closer to the quartz lamp, the measured temperature is typically 100 – 200 °C higher than the actual tape temperature. The YBCO films are typically produced under the conditions of laser frequency up to 80 Hz at 650 mJ in an oxygen atmosphere of 200 mTorr. To date, lengths up to 5 m have been produced.

X-ray diffraction indicates a high degree of orientation of the PLD YBCO films for both in plane (Fig. 69a) and out of plane (Fig. 69b) texture. It should also be noted that there is a significant improvement of the in-plane texture of the various layers in the structure. The epitaxial MgO (deposited on the IBAD MgO/Hastelloy C276) has a φ scan FWHM of 6 to 7°. The LMO layer (50 nm thick) deposited on the epi-MgO has a φ scan FWHM of 5 to 6° (Fig. 70a). Finally, the YBCO layer (2 μm) has a φ scan FWHM of only 2.5-3.5° (Fig. 70b).
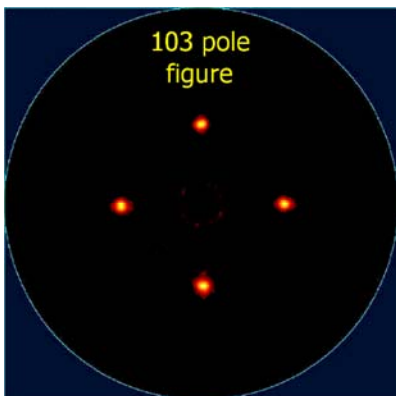
Fig. 69a. X-ray diffraction pole figure of YBCO film showing good in-plane texture.
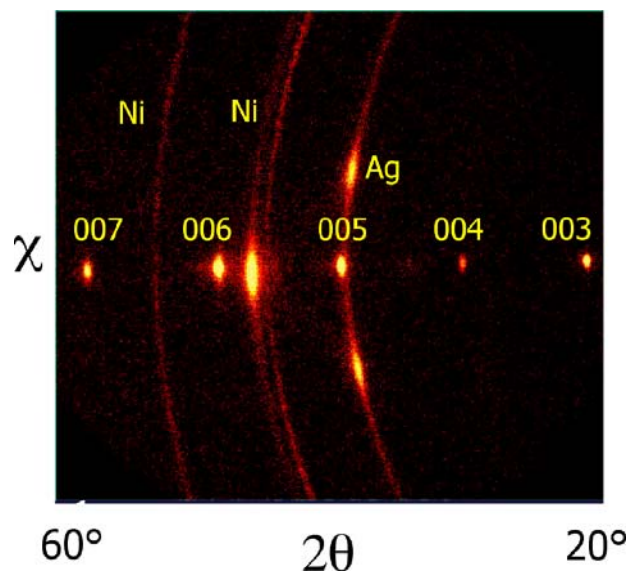
Fig. 69b. X-ray scan of a 2 μm thick YBCO film with a 0.5 μm Ag overcoat showing the 00l YBCO peaks.
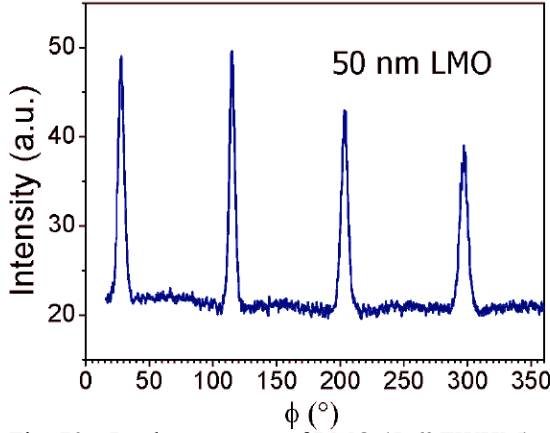
Fig. 70a. In plane texture of LMO (5-6º FWHM).
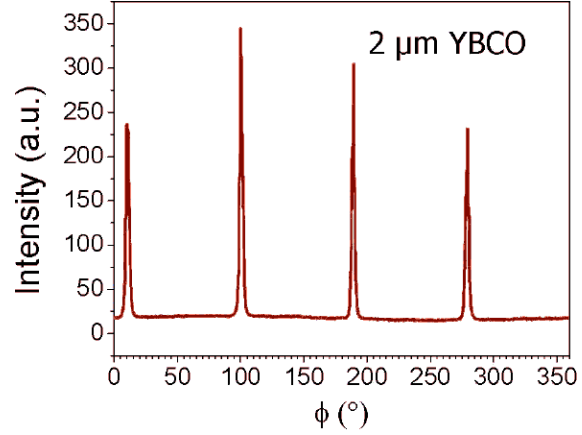
Fig. 70b. Improved in-plane texture of YBCO (2.5-3.5º FWHM).

Critical current performance at self field and 75.5 K for 2 μm YBCO/50 nm LMO/Epi-MgO/IBAD-MgO/Nickel alloy tapes are 178 A across 1 cm, 120 A across 10-20 cm, and 50 A across 1.1 m. Microbridge samples show critical current densities of greater than 1 MA/cm^2. (Fig. 71a). Magnetic field dependence (Fig. 71b) of the critical current I_c shows behavior typical of other films produced by PLD. There is also evidence of a small peak in the c-axis direction.
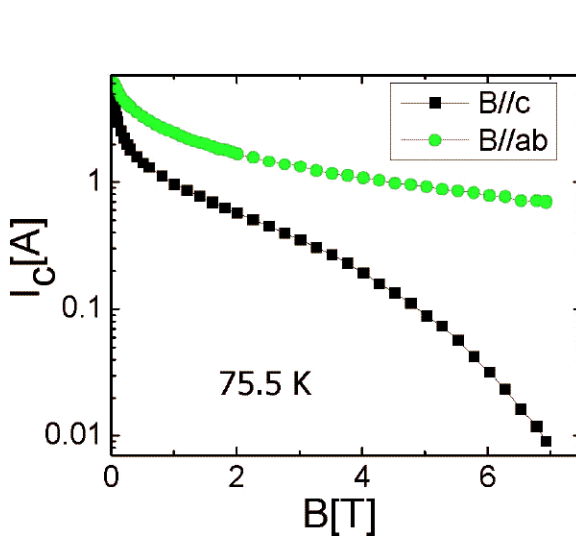
Fig. 71a. Magnetic field dependence of a coated conductor microbridge sample..
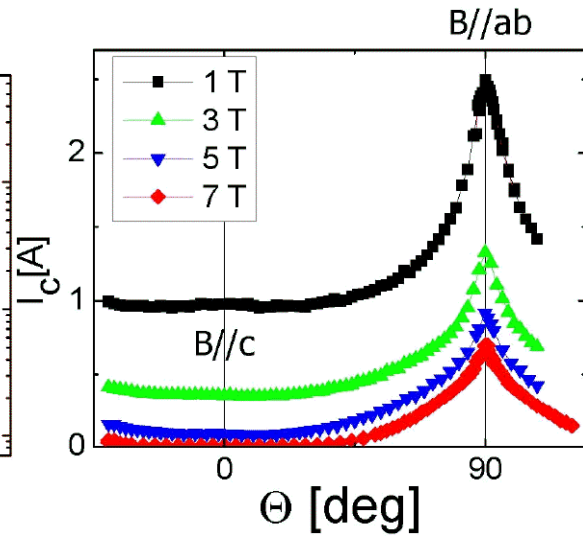
Fig. 71b. Angular dependence of I_c for several magnetic fields of a microbridge at 75 K.

One of the main goals of this study is to increase the rate of production of coated conductor tape. For the buffer and especially the YBCO layer there are a number of key issues that arise in doing this. As the deposition rate is increased, the substrate temperature must also be increased. However, the window for high-quality films seems to be smaller at higher rates.

Fig. 72 shows the dependence of I_c on thermocouple temperature for films deposited at comparatively low rates. These measurements are for films deposited at a laser repetition rate of 30 Hz, equivalent to 0.9 m/h for 1 μm film (4.5-6 nm/s). Fig. 72b indicates that for all deposition temperatures, there is no evidence of a-axis oriented material. Fig. 72a shows that all films produce a measureable I_c, with the best films deposited at 920 ºC.
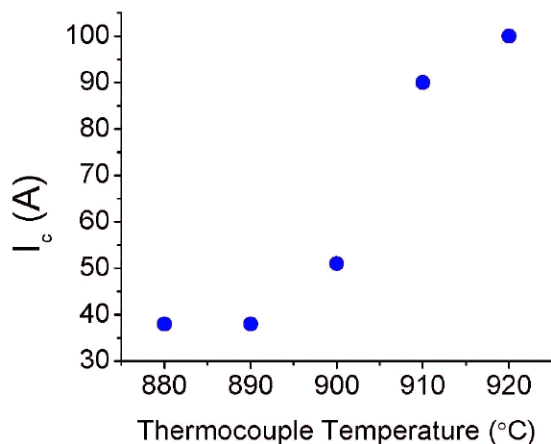
Fig. 72a. Dependence of critical current on substrate temperature.
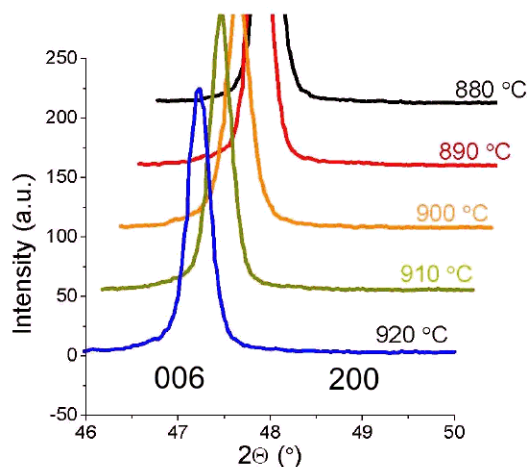
Fig. 72b. (006) x-ray peak intensity showing no evidence of the nearby (200) a-axis peak at all deposition temperatures investigated.

As the deposition rate is increased, the films must be deposited at a higher temperature. This results in several concerns. One, there is a question of substrate reaction at those higher temperatures, which would result in a dead layer, or a minimum thickness of YBCO to be superconducting. In addition, Fig. 73a shows that at the higher rate of 80 Hz, or 2.4 m/h for 1 μm (12-16 nm/s), the optimum temperature range is very narrow. For lower temperatures, the presence of a-axis oriented YBCO becomes larger. This is seen directly in the x-ray scans of the samples (Fig. 73b) with the presence of the (200) peak arising at lower temperature. At temperatures above the optimum of ~935 ºC, there may be more substrate-sample interaction occurring, which degrades the superconducting properties.
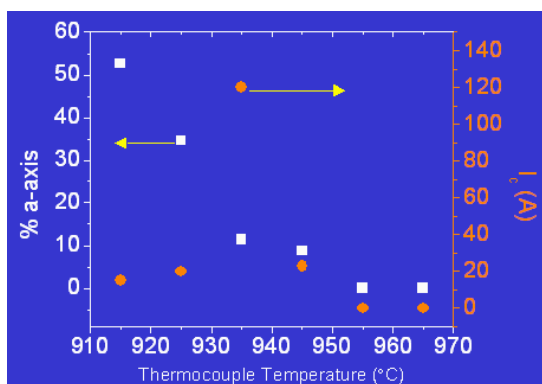
Fig. 73a. Critical current and %a axis YBCO as a function of deposition temperature for films deposited at 12-16 nm/s.
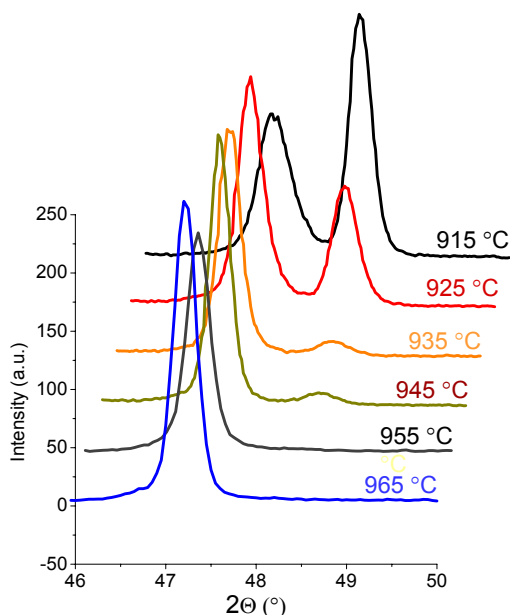
Fig. 73b. X-ray peak intensity for the 006 peak (left) from c-axis oriented YBCO and the 200 peak (right) from a-axis oriented material.

61

Plume stability and uniformity become increasingly important as the deposition rate is increased (as the laser repetition rate approaches 300 Hz). The quality of the beam raster over the target becomes very critical. To maximize utilization of the target material and to minimize surface modification and plume tilting, precise control of the target position and velocity are essential. In Fig. 74, the effects of improvements in the target rastering routine are apparent. However, variations over the target surface are still apparent in the modified routine. This can be addressed further by more significant modifications to the target raster mechanism.
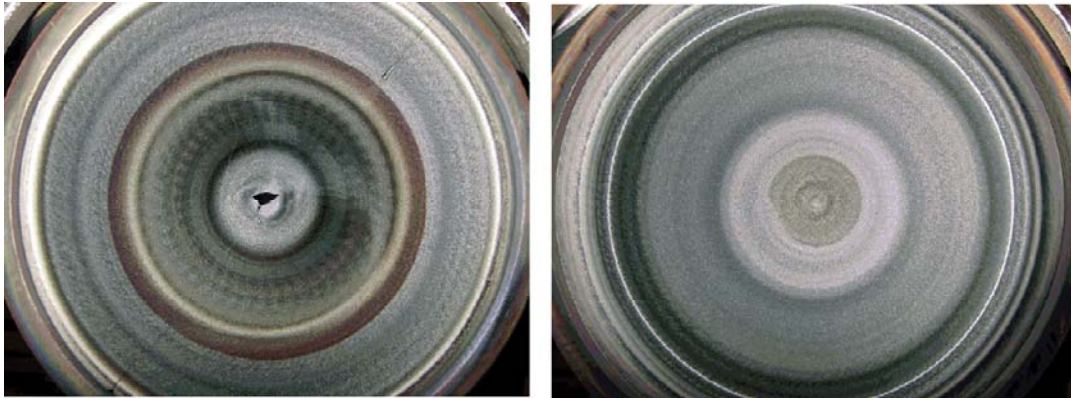
Fig. 74a. YBCO target showing damage to the center region.

Fig. 74b. YBCO target with improved rastering.

As has been demonstrated above, the processing conditions in PLD are strongly interrelated. Laser frequency, tape speed, substrate temperature, and YBCO thickness all interact. With this complexity, even low rate depositions are a challenge. And at higher rates, the process control required for high quality films is significantly more stringent.

To reach higher instantaneous rates, one of the most critical variables is temperature control. To that end, a new heater (Fig. 75) employing nine independent zones using quartz lamps has been designed and is being constructed. This system will allow controlled temperature variation across the deposition zone. It is expected to yield a more robust process for higher rates and longer length tapes.
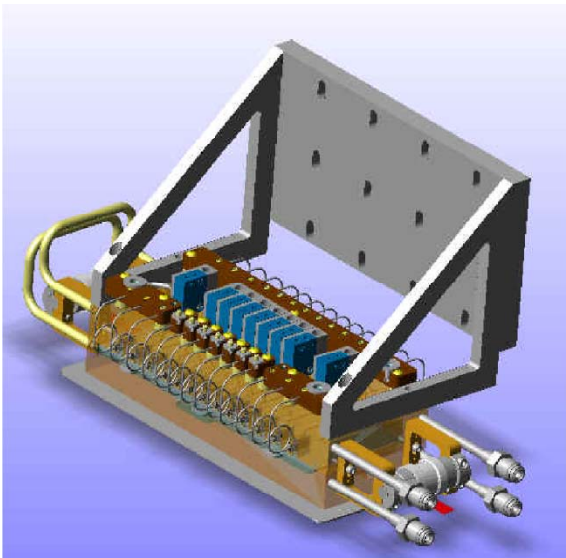
Fig. 75. Nine-zone quartz lamp heater for improved control of substrate temperature for high rate, long length deposition.

Preliminary investigations into the possibility of depositing YBCO directly on the homoepi-MgO/IBAD-MgO/Hastelloy substrate combination have begun. The premise is that if the homo-epi MgO layer is good and thick enough it may be possible to eliminate other buffer layers. Fig. 76a shows the pole figure of a well-aligned YBCO film grown directly on MgO. Fig. 76b indicates the clean interface between the MgO and YBCO layers. These results suggest that this simpler architecture may be feasible.
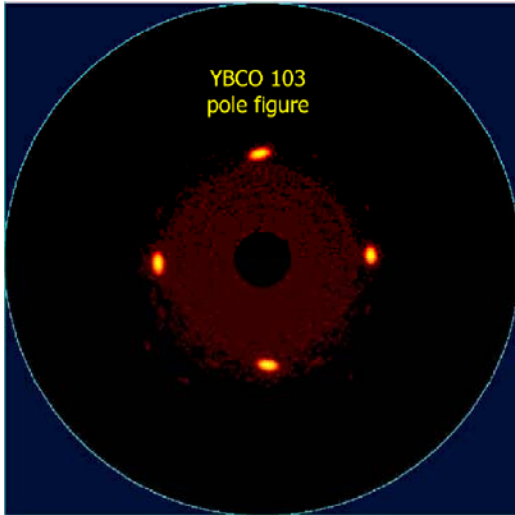
Fig. 76a. Pole figure of YBCO grown directly on the homoepitaxial MgO layer without intermediate buffer layers.
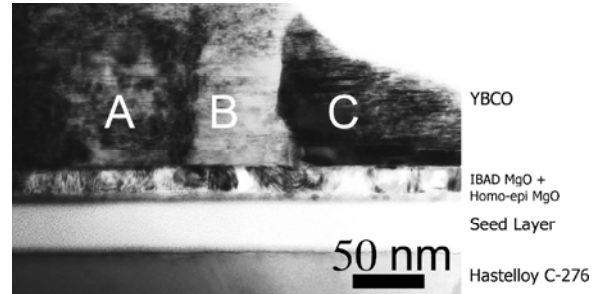
Fig. 76b. Cross sectional image of a 0.5 µm YBCO film with several columnar grains (A, B, and C) with a clean interface on unbuffered MgO.

Several collaborations with outside organizations have been implemented to more thoroughly understand and control the deposition process. In the first, with the Air Force Institute of Technology, the laser plume has been observed with a fast CCD camera and emission spectroscopy for plume analysis (Fig. 77). Using various filters, stoichiometry distributions within the plume can be observed, and forward peaking of the constituents was seen. Attempts to relate these effects to resultant electrical properties are ongoing.
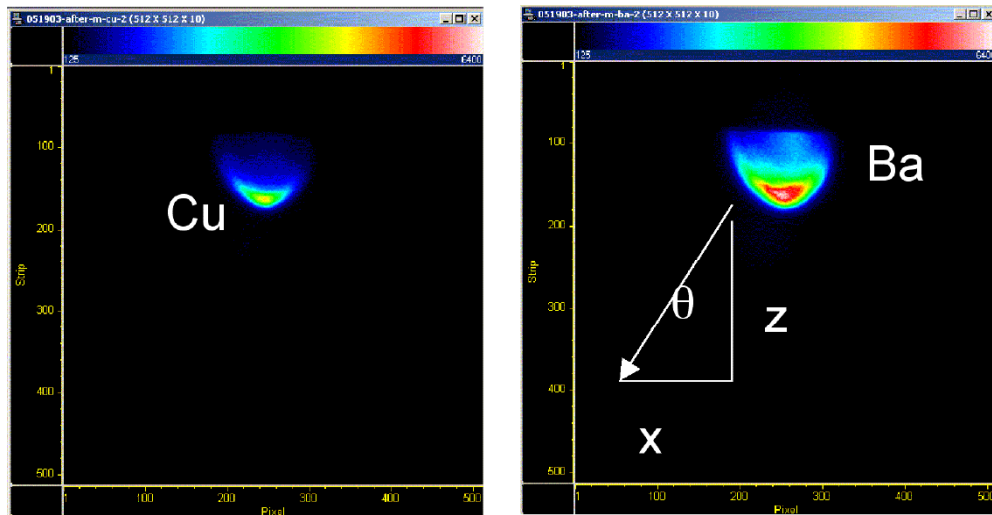
Fig. 77. Enhanced images of laser plume using a fast CCD camera and emission spectroscopy. The substrate is at the bottom of the image.

Another collaboration with Stanford University has also been established to develop a new system (Fig. 78) to measure the substrate temperature by Fourier Transform Infrared (FTIR) Spectroscopy.
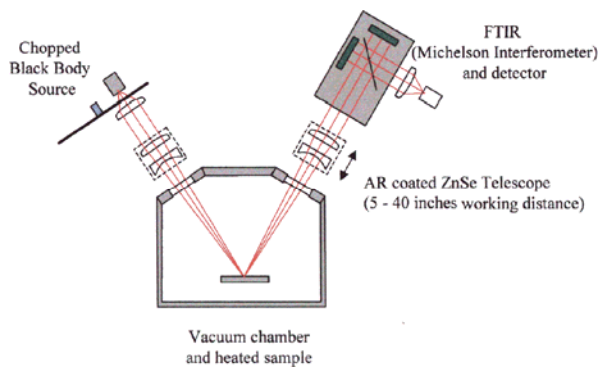
Fig. 78. FTIR system for substrate temperature measurements.

As a result of the work performed to date using substrates electropolished and MgO IBAD produced in the coated conductor development program, short samples of PLD YBCO tape have been produced with I_c values in excess of 170 A (self field, 75 K, 1 cm width) and 50 A in greater than 1 m lengths. The YBCO has been deposited routinely with in-plane texture of $\leq 3°$ FWHM. Some future goals are to improve the thermal control of the substrate during deposition and to increase the deposition rate. This will assist in the goal to fabricate 5 m lengths of conductor with I_c >200A @ 75 K (J_c > 1 MA/cm^2) Another target is to reduce variations over the tape length to <10% on a 2 cm measurement length.

2.1.7 Coated conductor development: long length measurement systems
L. Civale, J.Y. Coulter, J.O. Willis, V. Matias, and B.J. Gibbons

To characterize the long length coated conductors produced in the coated conductor development program, it was necessary to build a measurement system to determine the critical current as a function of position. A schematic of this device is shown in Fig. 79. This system can be used for both routine and for combinatorial measurements. It can handle tapes up to tens of meters with fully automatic tape transport and data acquisition. The tape transport mechanism has a resolution of 0.1 mm and a reproducibility of <0.25 mm for meter long tapes. Transport measurements are made using current contacts, which are copper rollers, ~40 cm apart. Most measurements are made in an applied magnetic field to reduce currents to <80 A and avoid sample damage. Spring loaded, sliding voltage contacts are made with variable separation up to 30 cm. During measurements, all components indicated in Fig. 79 are immersed in liquid nitrogen. Typical measurement rates are ~1 current-voltage curve per minute.
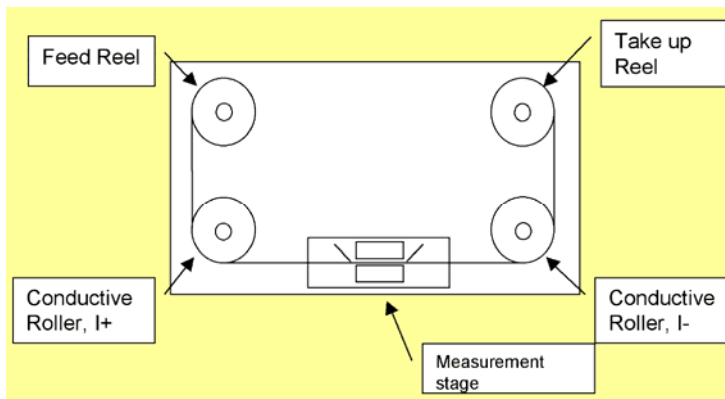
Fig. 79. Schematic of the long length coated conductor measurement system.

The in-field transport measurements are made using one or more permanent magnets (Fig. 80a) to generate the field perpendicular to the tape plane. The field profiles (Fig 80b) can be tailored for a particular experiment, with fields up to 0.75 T available. This reduces the critical current by a factor of 6-7 from the self field value, and thus protects lower I_c sections in a long tape from damage while measuring a stronger section.
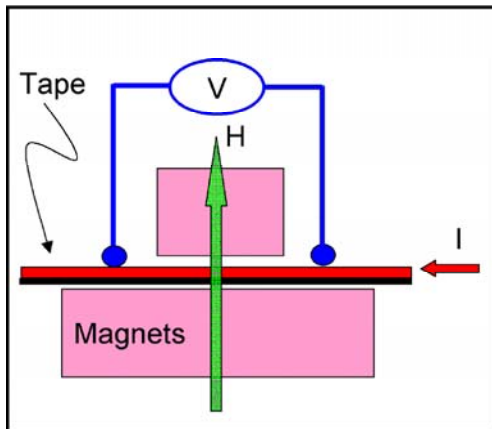
Fig. 80a. Configuration of tape sample, current, voltage contacts, magnets and magnetic field.
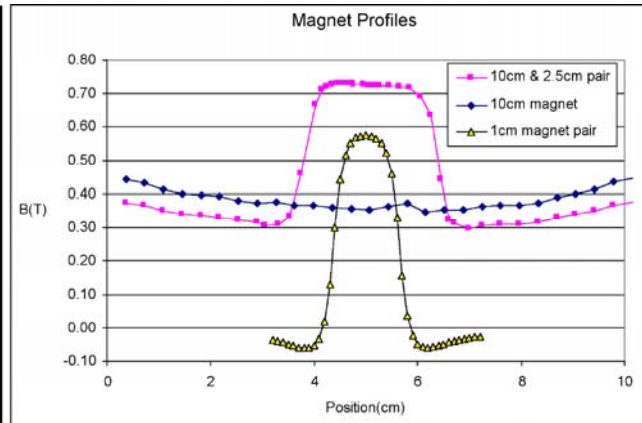
Fig. 80b. Magnetic field as a function of position for several configurations of permanent magnets.

To validate the performance of this system, the same tape was measured first in an earlier system where the tape is fixed and the voltage contacts move. It was also measured in field. The sample was then measured in the new system at two different magnetic fields (Fig. 81). There is good qualitive agreement among all three data sets. The speed of the H=0.36 T measurement set was 1.5 m/h at a 2.5 cm step size. Scaling the data sets (Fig. 82) to H = 0.36 T yields an almost perfect over lap of the data, except for the region near 30 cm, where some handling damage may have occurred. The scaling factors used to generate Fig. 82 are plotted and compared in Fig. 83 with data measured in a high field magnet system on one short sample taken from one end of the tape. The agreement here is also good, indicating that magnetic field dependence may be determined in the continuous measurement system without risk of damage to the sample.
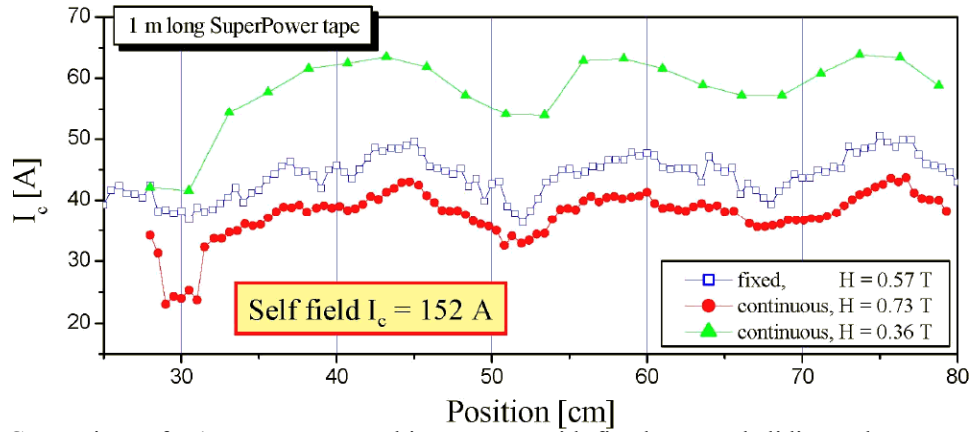
Fig. 81. Comparison of a 1 m tape measured in a system with fixed tape and sliding voltage contacts with data taken in the current system at two different applied magnetic fields.
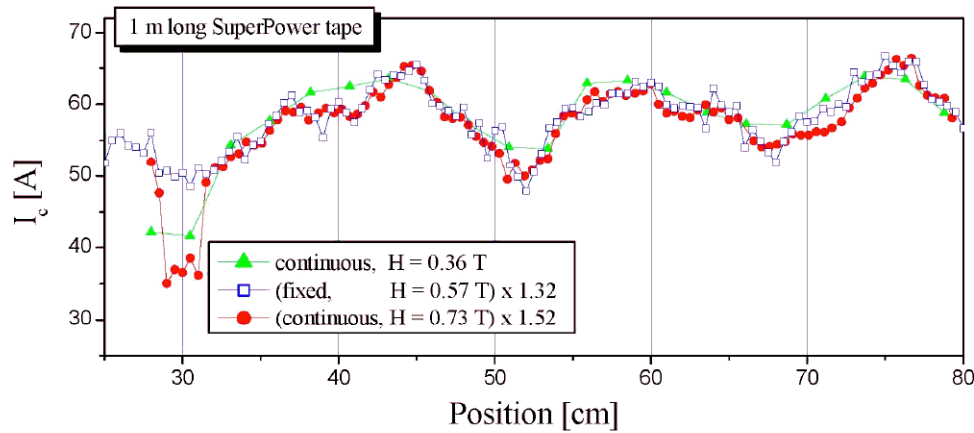
Fig. 82. Scaling of data to H=0.36 T for a long length tape measurement.
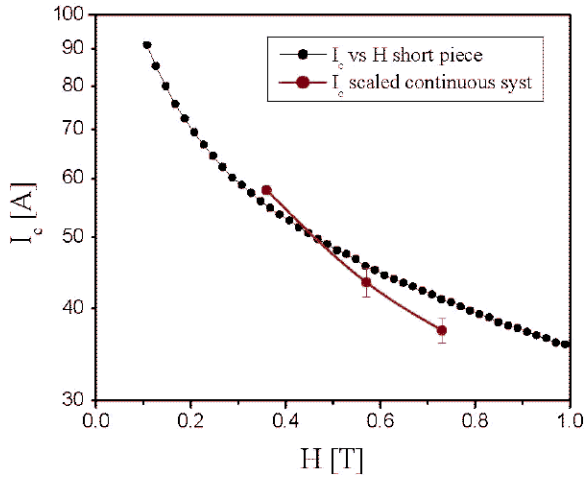
Fig. 83. Comparison of magnetic field dependence measured for a short sample with the average of that determined for the 1 m sample.

During measurement of the I_c values, a current-voltage (I-V) curve up to 50-100 µV is determined. The data are fit to a power law model and the shape characterized by the equation $I_c = A(E/E_c)^N$, where A is a constant, E is the electric field, E_c is the electric field criterion (typically 1 µV/cm) and N is the power law exponent. The N value characterizes the sharpness of the I-V curve and may reflect microscopic variations along the measurement region in J_c or in the cross section or connectivity. The N value data (Fig. 84) on the sample shown in Figs. 81-83 show that the n values correlate with I_c, indicating that the inhomogeneities in the sample are on a microscopic scale.
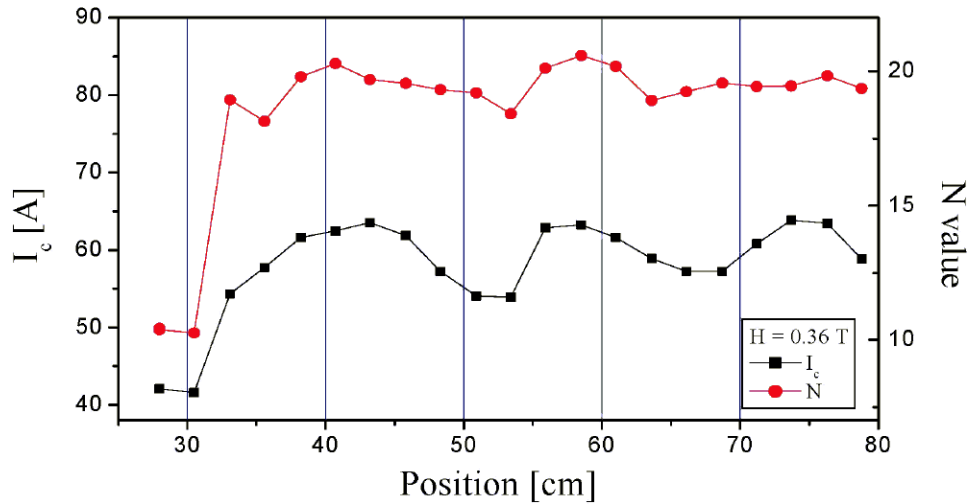
Fig. 84. Variation of I_c and N as a function of position for a long tape.

The measured I_c values for the first 2 m long tape produced within the coated conductor development program are shown in Fig. 85. A 1 m length of the tape was later measured to have a self field (75 K) end to end I_c value of 50 A. This data set illustrates that nondestructive I_c measurements are possible even though one spot has $I_c = 0$. Results from this type of measurement are used to select portions of the conductor for self field and end to end measurements.

67
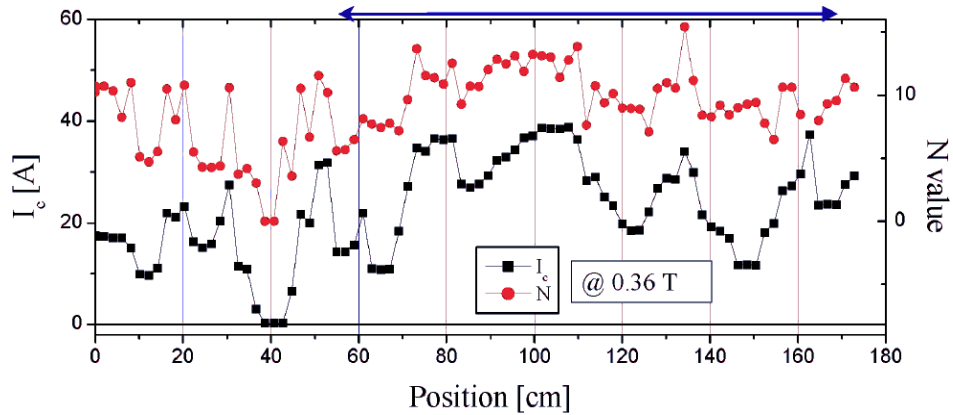
Fig. 85. Measurement results for the first 2 m tape produced in the coated conductor development program. The region indicated by the arrows at the top has a self field I_c of 50 A.

A new system (Fig. 86) is being developed that has several advantages over the system now in use. Because only the lower portion system in immersed in liquid nitrogen, the tape to be measured can be loaded and unloaded at room temperature. This system could be inserted directly into a fabrication line. It also allows adjustment in the separation between the current contacts.
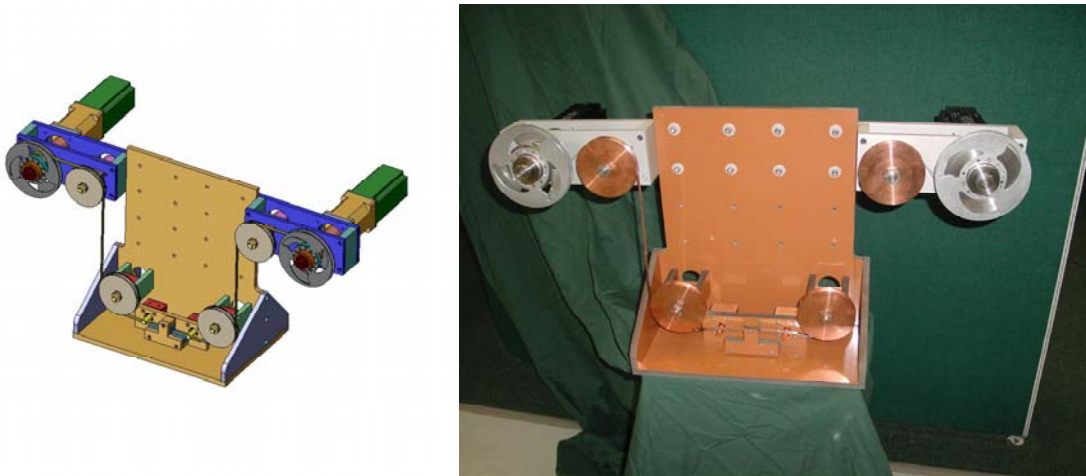
Fig. 86. A new continuous measurement system is under construction.

Summarizing the results of the continuous measurement program, a system has been built, tested and used for YBCO coated conductor I_c characterization. In field measurements provide the required data without risk of sample damage. The magnetic field profiles and field magnitudes can be varied to determine the field dependence of I_c. Tapes up to 2 m have been measured. Finally, a new measurement system with enhanced capabilities is under construction.

2.1.8 AC loss studies in HTS conductors
S.P. Ashworth and Jose Vasquez-Dominguez

Understanding and reduction of the ac losses in HTS coated conductors are important to the wide scale use of these materials in power applications. To that end, a program has been initiated to characterize the ac losses of coated conductors under various conditions. Coated conductors on both RABiTS (roll-assisted biaxially textured substrates) and IBAD (ion beam assisted deposition) template layers as a function of magnetic field amplitude and angle to the tape plane, of current amplitude, and using several different measurement techniques, have been completed.

The data shown in Fig. 87a are on a coated conductor on a RABiTS employing a Ni-W alloy with a thin Ni layer on the top surface. This 1 cm-wide sample with a 77 K critical current >100 A was obtained from American Superconductor Corp. (AMSC). The sample was measured as a function of applied perpendicular (to the tape plane) ac magnetic field at several frequencies. The independence of frequency implies that the losses are hysteretic in nature, as opposed to eddy current-type losses. There are two regions characteristic of most superconductors: a cubic dependence at low fields rolling over to a linear dependence at higher fields. The results shown in Fig. 87a indicate that the observed loss is greater in magnitude than that expected theoretically from the superconductor. Therefore, the contribution from the substrate (Ni/W alloy plus Ni layer) was also investigated. Fig. 87b compares the total loss with that from the substrate only. These data show that the contribution from the substrate is really quite small, at least one order of magnitude smaller than the total loss.

To investigate this discrepancy more carefully, the magnetic induction - magnetic field (B-H) hysteresis loop was determined for the bare substrate in parallel magnetic field, where the sample demagnetizing effect is small and thus the intrinsic material properties can be obtained. From these data, the complex susceptibility and the volume ac losses as a function of local magnetic field amplitude can be calculated. These results are shown in Fig. 88.
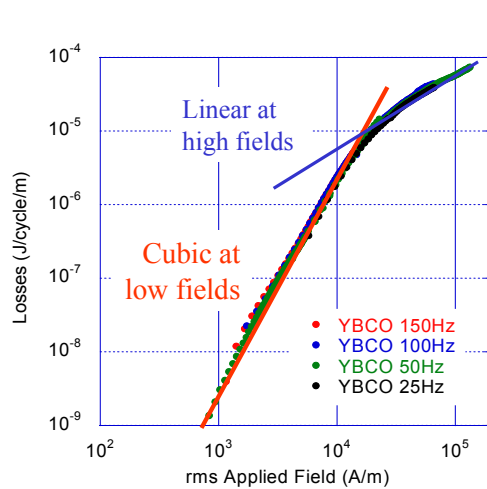
Fig. 87a. AC losses as a function of perpendicular magnetic field for a RABiTS coated conductor tape (tape supplied by American Superconductor Corp.)
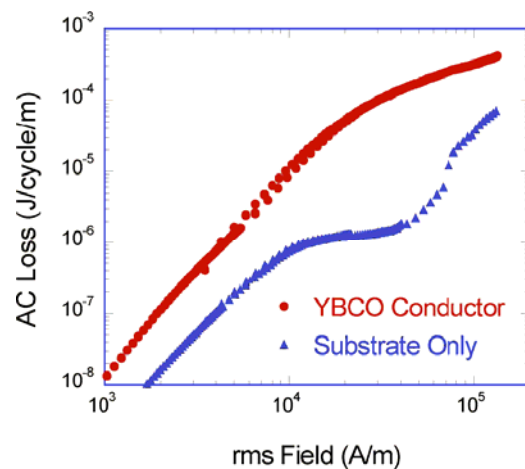
Fig. 87b. Comparison of the measured ac losses for a coated conductor and of the substrate only as a function of applied perpendicular magnetic field.
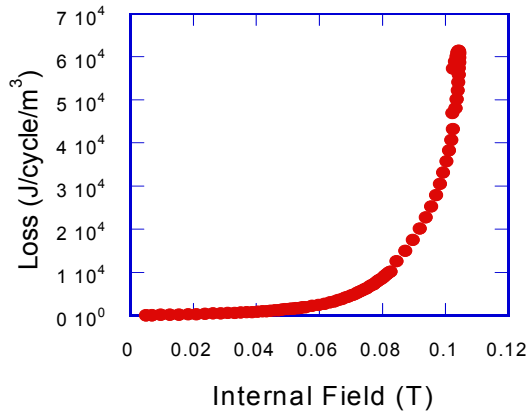
Fig. 88. Losses in the bare RABiTS material as a function of parallel magnetic field calculated from B-H hysteresis loop data.

A finite element (FE) calculation (using 0.1 mm wide strip grid) of the local magnetic fields in the substrate and sample under the conditions of an applied perpendicular magnetic field are shown in Fig. 89a. The calculation shows that the magnetic field is highly concentrated at the edge of the sample. This is a result of the demagnetizing effect of the sample shape and the lack of field penetration into the sample at these relatively low field amplitudes because of the very high critical current density. Fig. 89b (solid blue curve) shows the field magnitude at the location of the red line in Fig. 89a. Also shown in Fig. 89b (dotted red curve) is the calculated loss for the substrate; both functional forms are strongly peaked near the sample edge.

Including both the calculated losses from the HTS material and the calculated localized losses from the RABiTS due to the ferromagnetic hysteresis, the sum of these losses is in reasonable agreement with the measured values on the coated conductor. Thus the extra losses from the substrate material are localized in nature.
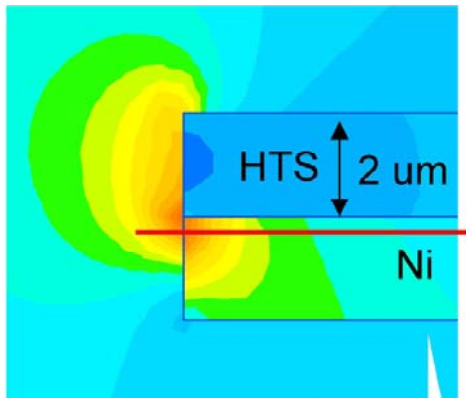
Fig. 89a. Finite element calculation of the magnetic fields near the edge of the sample in an applied perpendicular field. The color scale varies from blue to red as the magnetic field increases. The magnet field amplitudes along the red line are shown in Fig. 89b.
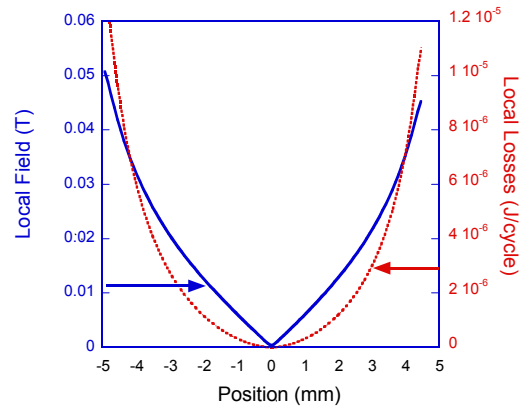
Fig. 89b. Calculated magnetic field (solid blue line) in the Ni layer of the substrate at the position of the red line in Fig. 89a. The dotted red curve shows the calculated losses in the substrate.

Several methods to reduce the ac losses of this conductor have been investigated. These involve doubling the amount of HTS material but also change the local magnetic field, leading to the reduction in substrate losses. Fig. 90 shows the ac losses for the single tape, a stack of two tapes with the HTS inside (face to face) and a stack with the HTS on the outside. Both these configurations exhibit reduced losses, with the more significant reductions (~X8) for the HTS on the outside: this configuration provides better shielding of the Ni from the magnetic field, and it also simulates a double-sided tape configuration with a single substrate. Thus, appropriate selection of the tape configuration can lead to a lowering of the ac losses.
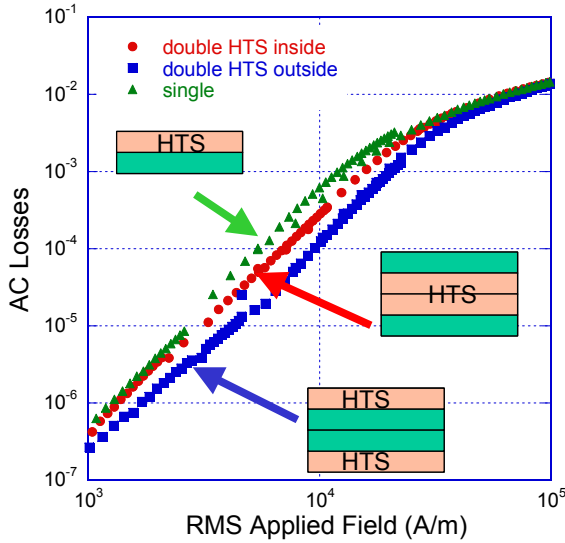
Fig. 90. Losses in a RABiTS-based coated conductor for several different configurations of a two-tape stack.

The next series of measurements examine the effects of combined ac transport current and applied ac magnetic fields on ac losses for a coated conductor. The measurements use a microcalorimetric technique pioneered at Brookhaven National Laboratory with continued improvements at Los Alamos National Laboratory. It is very difficult to achieve accurate measurements of ac losses under the combined affect of both current and magnetic field, and impossible if these two are not at the same phase. The RABiTS sample was provided by AMSC.

The first set of data, shown in Fig. 91a, was taken with the current and magnetic field in phase. At low magnetic fields (>0.04 T), the losses are dominated by the current, increasing with increasing current amplitude. At higher magnetic fields, the magnetic losses dominate. It is noteworthy that this is the same dependence that is observed for coated conductors on IBAD and for BSCCO powder in tube tapes.

As the phase angle between the current and magnetic field is varied, there is a significant change in the ac loss magnitude (Fig. 91b). This variation is present because the local ac loss varies as the cube of the magnetic field, and is thus very nonlinear. At phase 0º, the peak fields are highest on one side of the tape (dominating the integrated losses) and lowest on the other side. At 90º, the peak fields are at a minimum, and the overall losses are reduced. Again, this is the same dependence that is observed for coated conductors on IBAD and for BSCCO powder in tube tapes.

71
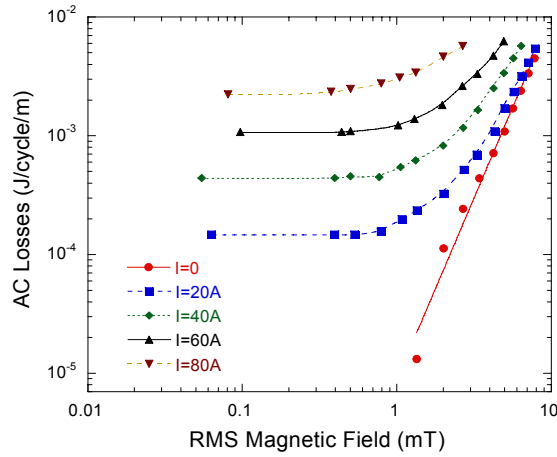
Fig. 91a. Losses for a coated conductor as a function of applied perpendicular magnetic field and transport current. Sample is from AMSC.
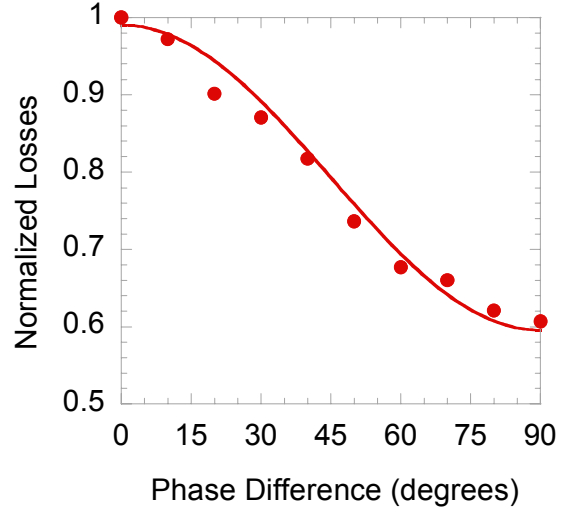
Fig. 91b. Coated conductor normalized ac losses as a function of the phase angle between the current and ac applied magnetic field.

The final set of measurements is of the ac losses in a coated conductor tape deposited on an IBAD MgO template film on a nickel alloy (nonmagnetic) substrate. This 1 cm wide tape was manufactured at the Los Alamos Research Park and has a critical current >100 A. The losses (Fig. 92) follow a series of power laws: cubic (the result for an conductor with an elliptical cross section according to Norris and the critical state model), square, and linear, as the magnetic field is increased. There is no hint of a quartic power law region, indicative of losses in a strip conductor, according to Norris. The losses are similar to those of the sample from AMSC reported above, independent of frequency when plotted per cycle, thus indicating that they are of hysteretic nature and arise in the superconductor.
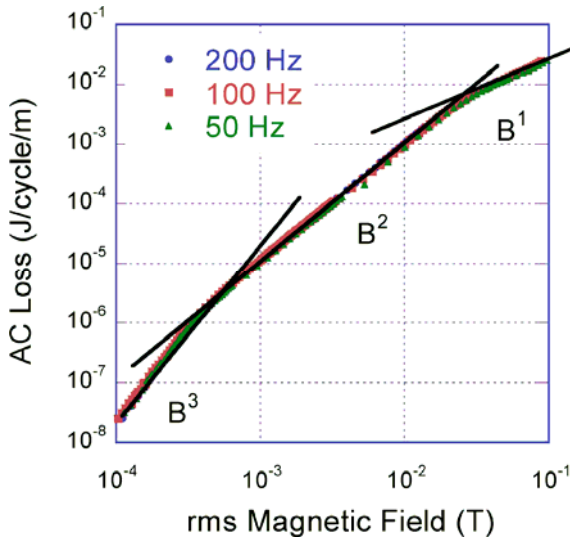
Fig. 92. AC losses as a function of applied perpendicular magnetic field for a coated conductor sample on IBAD MgO.

Starting with this short sample, some experiments were made in an attempt to reduce the ac losses in a perpendicular magnetic field. The 1 cm wide sample was measured at 2 frequencies as a function of ac field. It was then patterned into a series of 5 parallel strips each 2 mm by scribing (with a 50 μm linewidth) along the tape length. The losses were then remeasured and found to be smaller (Fig. 93). Finally, the width of each strip was

reduced by a factor of two, resulting in 10 strips each 1 mm wide. There was a further reduction of the losses, about a factor of four from the 10 mm wide result in the mid range region where the power law is B^2; the decrease is somewhat larger in the other two regions (Fig. 93). As yet there is no model for the reduction of losses; this is purely an empirical result.
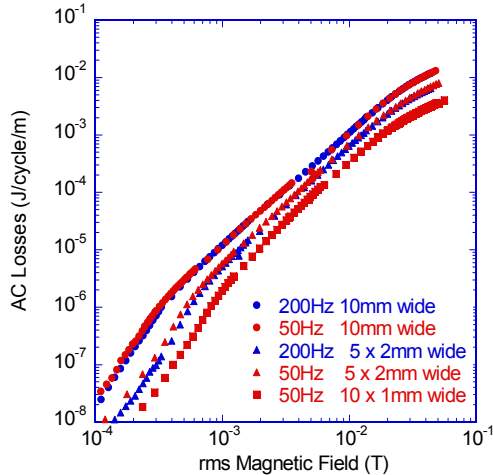
Fig. 93. Reduction of ac losses in short sample of coated conductor on IBAD MgO.

Future work calls for continuing studies of ac losses as a function of magnetic field angle, studies of interactions among stacks and arrays of conductors on the ac losses, development of lower loss conductors, study of the cryo-stabilization of coated conductors under ac conditions. This latter will become increasingly important as the critical current density and critical current of the conductors increases, including the effect of eddy current losses in the Cu stabilizer and overall ac stability.

To summarize, the ac losses of coated conductors were studied as a function of several parameters. For coated conductors on Ni/W +Ni RABiTS, the losses in perpendicular field are larger than the theoretical value for the superconductor, but are hysteretic in all cases. FE calculations suggested that the magnetic field is greatly enhanced at the edges of the sample. Using the calculated field profile and the ferromagnetic losses as a function of field in the substrate material, the sum of the calculated losses from the superconductor and the substrate is in reasonable agreement with the experimental data. A method of tape stacking or conductor architecture was suggested to reduce the losses. Losses in combined transport current and perpendicular field are dominated by the former at low fields and the latter at high fields, a result similar to that of coated conductors on IBAD template layers and of powder in tube BSCCO tapes. Losses as a function of phase difference between the current and applied field are also similar to the losses for these other types of conductors, with the largest losses occurring when the parameters are in phase. Measurements of coated conductors on IBAD MgO showed several power law regions, and the losses in short samples were reduced as the tape was patterned into strips of progressively narrower width.

2.1.9 Residual Bi-2212 intergrowth distribution in high J_c tapes and its origin in the *in situ* conversion process

T.G. Holesinger, J.A. Kennison, J.O. Willis, M. Archuleta, (University of Wisconsin-Madison): E.E. Hellstrom, D.C. Larbalestier, X. Cai, (American Superconductor Corp.): A. Malozemoff, M. Rupich, A. Otto, Y. Huang, and (Argonne National Laboratory): V. Maroni

This work was performed as part of a collaboration with the Wire Development Group, consisting of members from American Superconductor Corp. (AMSC), Argonne National Laboratory (ANL), and the University of Wisconsin-Madison (UW). Formally, the work was performed as tasks of a CRADA with AMSC.

Previously it has been shown that the distribution of Bi-2212 intergrowths in Bi-2223 grains is spatially non-uniform: only Bi-2223 grains next to the silver sheath are free or nearly free of Bi-2212 intergrowths. Fig. 94 illustrates the density of defects (only 1 in A, a region close to the Ag interface) and many more further away from that interface, illustrated by section B. This sample is an AMSC production tape with a post anneal heat treatment and has a critical current I_c of 163 A and a critical current density J_c of 47.7 kA/cm^2, both at 77 K and self field.
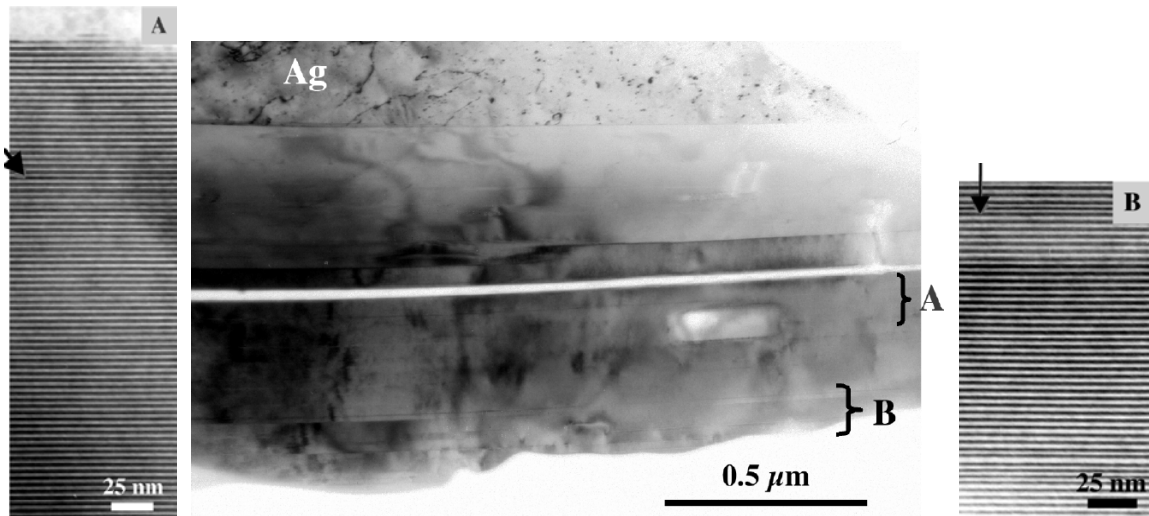
Fig. 94. Micrographs of showing very fewBi-2212 intergrowths (A) near the silver interface and many intergrowths (lighter regions) away from the interface (B) indicated by the arrow. B also has Bi-2234/Bi-2212 intergrowths in the region near the micron bar.

Both scanning electron microscopy (SEM) (Fig. 95 left) and scanning transmission electron microscopy (STEM) (Fig. 95 center and right) reveal significant amounts of residual Bi-2212 even in this very high J_c sample (J_c(0.1 T, 77 K) = 27 kA/cm^2) processed at UW with an overpressure post anneal, designed to increase density and enhance the conversion to Bi-2223. The box in Fig. 95 center indicates the regions over which the elemental maps in Fig. 95 right were made. These maps clearly show the discontinuity in composition indicative of a Bi-2212 intergrowth.

Over pressure processing has pushed J_c(0.1 T, 77 K) above 30 kA/cm^2; nevertheless, a significant population of Bi-2212 intergrowths remains (Fig. 96). As seen previously, the grains next to the silver interface have no intergrowths. Farther into the filament, the Bi-2223 grains contain Bi-2212 in varying amounts and shapes.
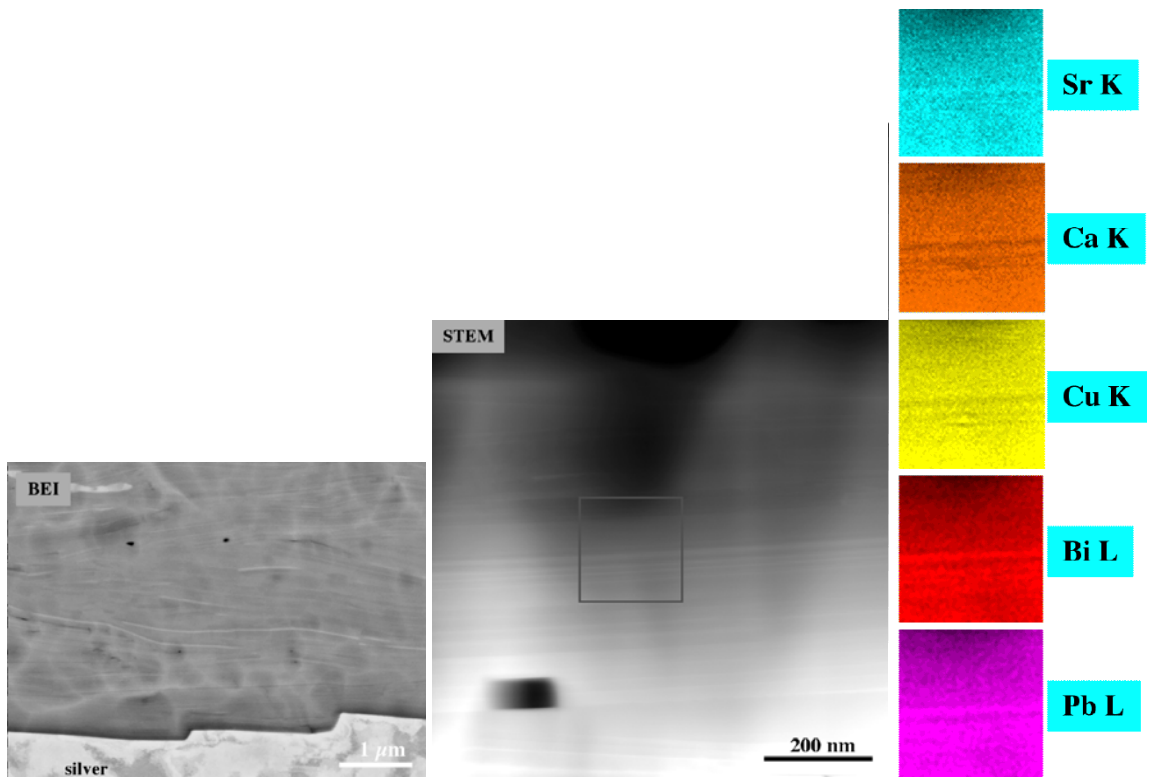
Fig. 95. (Left) Back scattered electron image of Bi-2223; (Center) STEM image of a Bi-2223 grain with a Bi-2212 intergrowth; (Right) Elemental mapping confirming the presence of a Bi-2212 intergrowth.
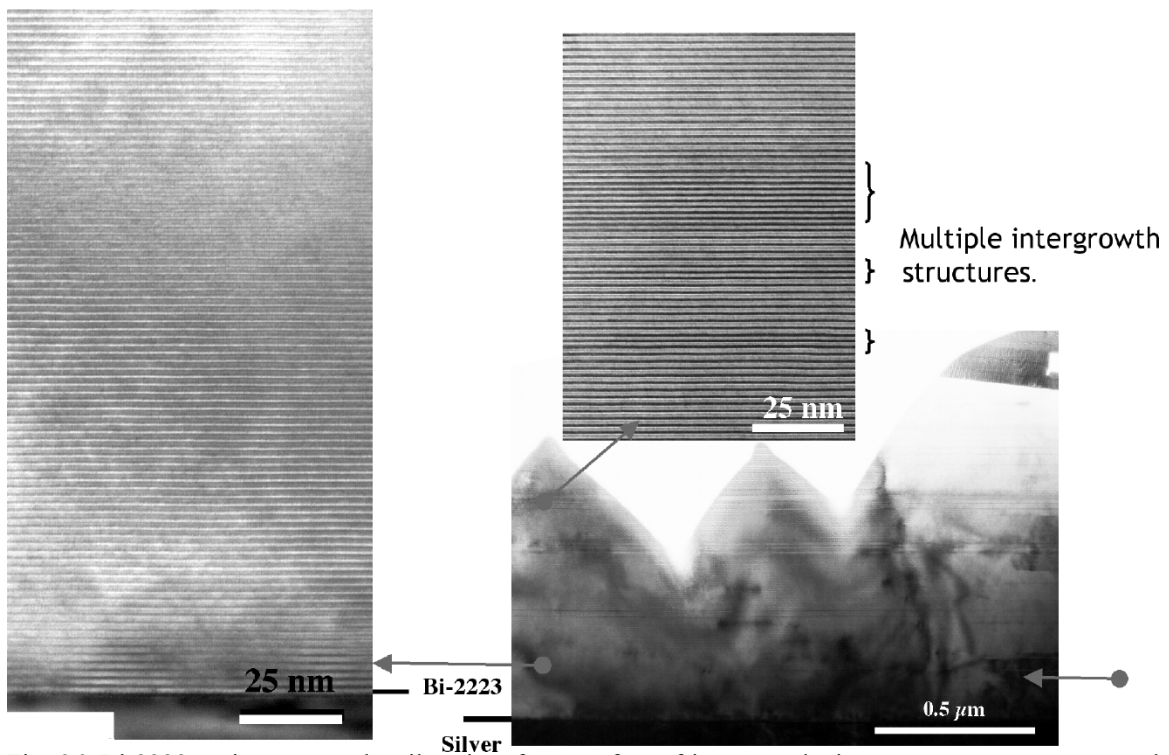
Fig. 96. Bi-2223 grains nearest the silver interface are free of intergrowths in an over pressure processed sample with J_c (0.1 T, 77 K) over 30 kA/cm^2. Grains further from the interface do have intergrowths.

The model for the structure of the filaments that can be proposed is one of a shell of well-formed Bi-2223 coating the inside of the silver sheath. Bi-2212 intergrowths and small grains can be found everywhere else in the filament. Material segregation from the conversion process leaves or traps unreacted material in the filament centers. This microstructural model can be confirmed by SQUID magnetization measurements. Fig. 97a is the magnetization curve indicative of a single-phase superconducting material, namely Bi-2223 as indicated by the ~110 K transition temperature T_c. However, upon crushing the filament structure by rolling, which breaks up the filament but does only minor damage to the grains themselves, Fig. 97b shows that the magnitude of the transition is reduced and it is broadened significantly with a small transition at 110 K (Bi-2223) and a larger one at ~80 K (Bi-2212). In retrospect, the result in Fig. 97a for the intact tape was the commonly observed "shielding" of a lower or zero T_c material by a higher T_c component (here, Bi-2223) that surrounds it. The true volume of Bi-2223 is less than the volume it encloses, by virtue of the Bi-2223's location at the silver interfaces.
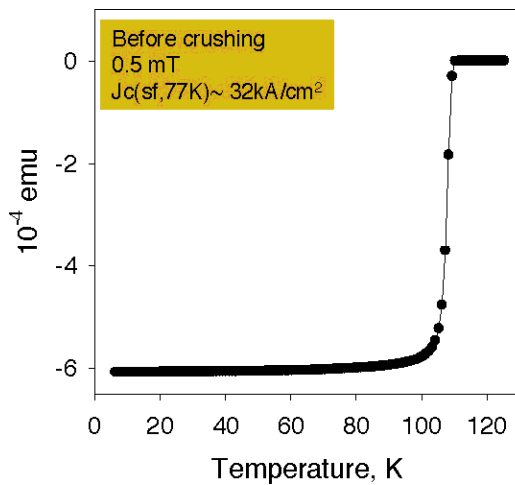
Fig. 97a. SQUID magnetization measurement of an intact Bi-2223 tape.
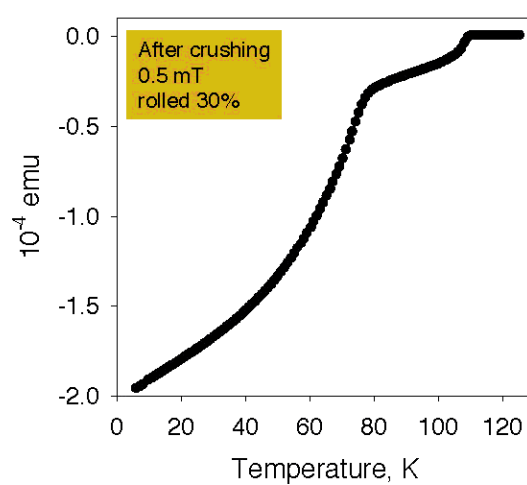
Fig. 97b. SQUID magnetization measurement of the same tape after rolling to break up the filament structure.

The "excess" material that could be used to convert residual Bi-2212 into Bi-2223 is trapped in the filament centers after full processing. Residual phases, such as the 14-24 alkaline earth cuprates (AECs), 2:1 AECs, and the Pb-rich 3221 phase often appear in the central region of a filament. Fig. 98 shows this for an AMSC tape processed at UW with an overpressure post anneal and having a $J_c(0.1\,T, 77\,K) = 27\,kA/cm^2$. The SEM image in the upper left shows the presence of some of these other phases as indicated by the arrow and the difference in contrast. The three elemental maps indicate the different compositions of the other phases. The conversion efficiency of these phases is reduced because the other material needed to react with them is in the Bi-2212 intergrowths trapped in the Bi-2223 grains.
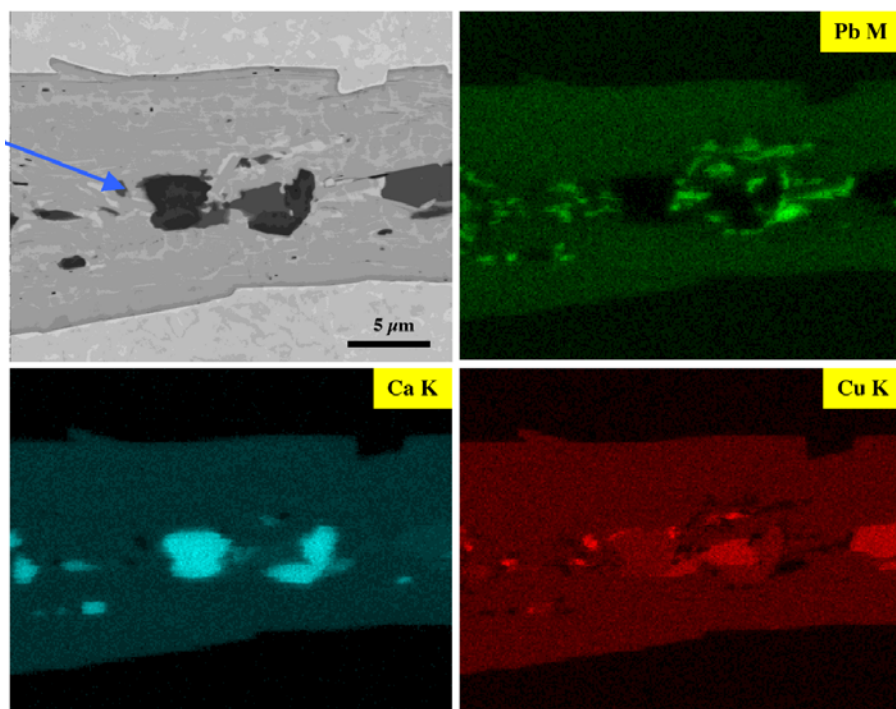
Fig. 98. SEM image with the arrow indicating other phases in the filament centers. Elemental maps allow the identification of these phase.

These compositional inhomogeneities began at the early stages of processing. Preferential growth starting at the silver combined with anisotropic growth rates define a growth front that rapidly decays into a jumble of Bi-2223 grains protruding into the filament center. Fig. 99a shows an AMSC tape after 360 minutes at 825ºC in an 8% oxygen atmosphere. Bi-2212 and other phases remain in the core region of the filament. Fig. 99b shows a tape quenched after 640 minutes. The presence of large second phases is clear in the elemental maps of the filament center.
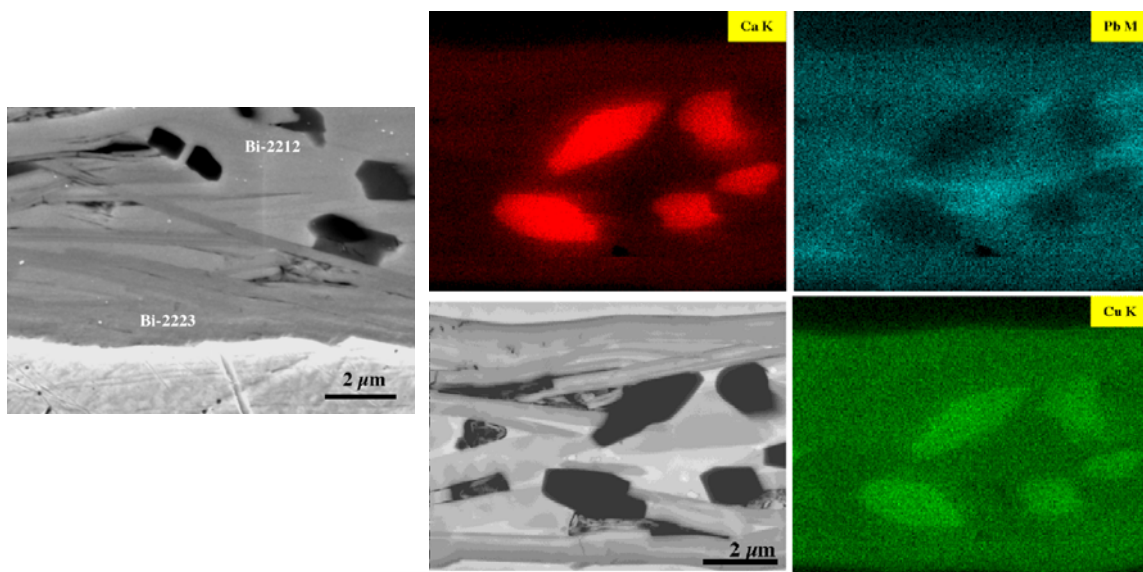
Fig. 99a. AMSC tape after 360 minutes of heat treatment at 825ºC in 8% O_2.
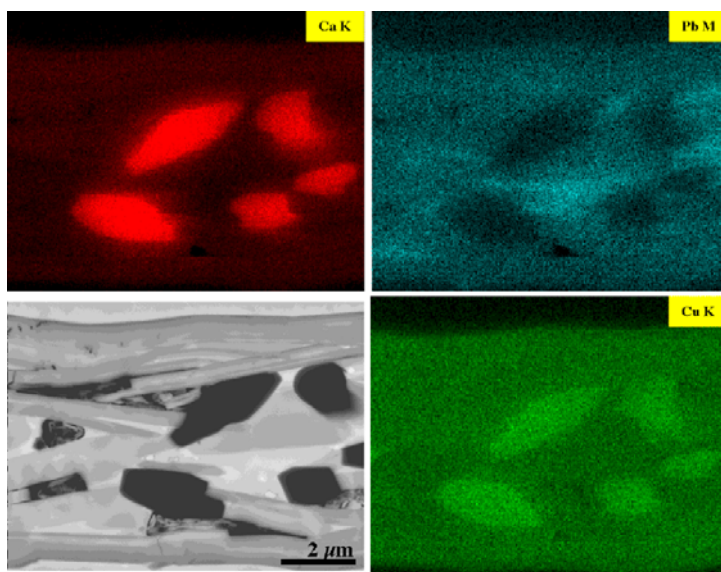
Fig. 99b. SEM backscattered image and elemental maps for an AMSC tape quenched in oil after 640 minutes at 827ºC in 8% O_2.

The distribution of residual Bi-2212 intergrowths within the grains starts with the Bi-2223 precipitation process from the partial melt. Intergrowths in the Bi-2223 grains are continuous, and their density is directly proportional to the distance from the liquid phase. The conversion process ultimately determines the overall distribution of residual Bi-2212 in fully processed tapes. The progression of the phases and the amount of non Bi-2223 phases (intergrowths) is apparent from Fig. 100.
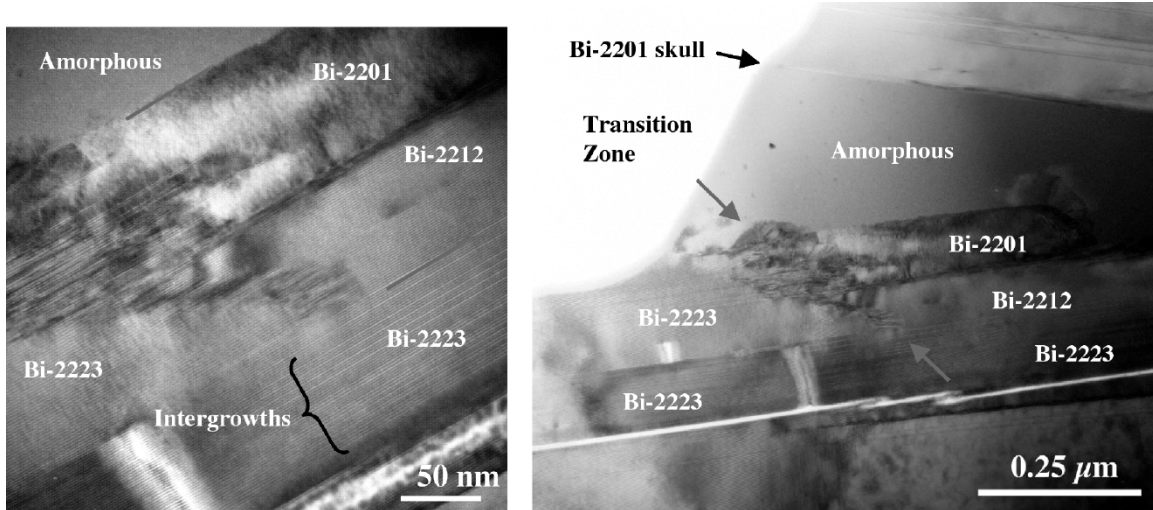
Fig. 100. Density of intergrowths in the Bi-2223 grains is proportional to the distance from the partial melt region.

To summarize, the density and location of Bi-2212 intergrowths during the growth and in fully processed Bi-2223 tapes has been studied. They are almost nonexistent near the silver interface, but increase in density toward the filament cores. "Excess" material found in the core that is prevented from reacting fully to become Bi-2223 because the Bi-2212 needed for this reaction is trapped in the Bi-2223 grains in the form of intergrowths. These intergrowths are present even in very high quality tapes commercial AMSC tapes or those tapes with an overpressure post process.

2.2 System Technology

2.2.1 Design and development of a 100 MVA HTS generator SPI project

J.A. Waynert, S.P. Ashworth, T.A. Jankowski, F.C. Prenger, J.A. Stewart, D.E. Peterson; (University of New Mexico): A. Razani; (University of Illinois-Chicago): J. Campuzano

This work has been undertaken as part of a Superconductor Partnerships with Industry (SPI) project headed by General Electric (GE) and also includes components performed at GE and at Oak Ridge National Laboratory not discussed here.

The major task at LANL is to provide data and technical support for long term vacuum maintenance of the generator. The HTS rotor winding is at 20-40 K and is surrounded by a 300 K environment. Vacuum represents the main insulation. The goal of the program is to achieve a suitable vacuum with no active pumping by means of suitable getters to adsorb particular gas species for a period of ~5 years. Outgassing and gettering properties determine the vacuum life. The outgassing properties depend on the material (stainless steel, composites, aluminum, etc.), the material preparation (machined, welded, etc.) cleaning (materials/chemicals, methods, etc.), handling, assembly environment, and operating temperatures. The gettering ability depends on the getter material, the quantity of material, the gas species, the quantity of gases present, the temperature of the getter, etc.

The system for measuring outgassing is shown in Fig. 101. The pressure difference across a known orifice yields the mass flow rate. Some requirements of the method are that the sample chamber must outgas less than the sample, the temperature must be known and controlled, and the system must accommodate easy sample changes (many samples measured. Finally, it is important to account for re-adsorption because $outgas_{actual}/outgas_{measured} \sim 10^3$.
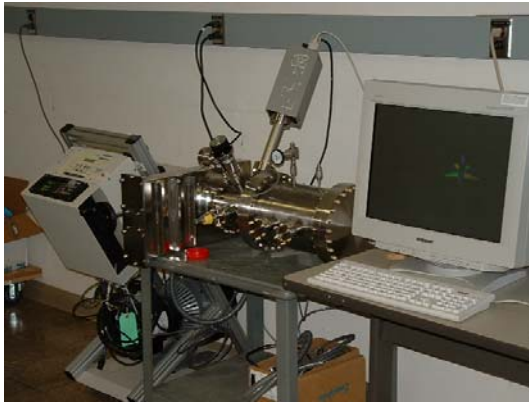
Fig. 101a. Photo of the chamber, pumping system and data acquisition system.
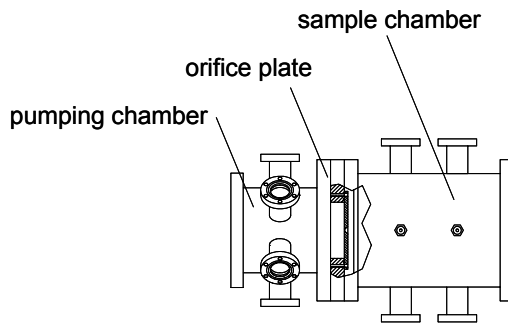
Fig. 101b. Schematic of the vacuum system.

Some results from this system are shown in Fig. 102. Fig. 102a shows the pumpdown curve for multiple numbers of samples as a function of time. Fig. 102 shows the outgassing rate as a function of the orifice area/(sample area times the sticking coefficient).

Fig. 103 shows the data for one material for different numbers of samples and orifice diameters (indicated as 'number: diameter', respectively, on the figure).
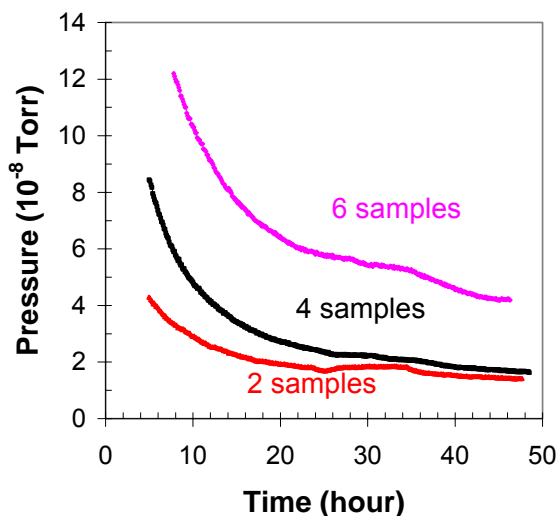
Fig. 102a. Pressure as a function of time for multiple number (area) of sample materials.
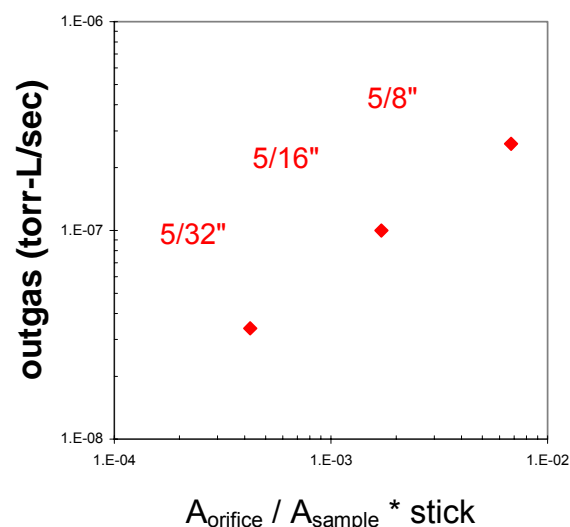
Fig. 102b. Outgassing (mass flow rate) for different orifice sizes normalized by the relative area and sticking coefficient.
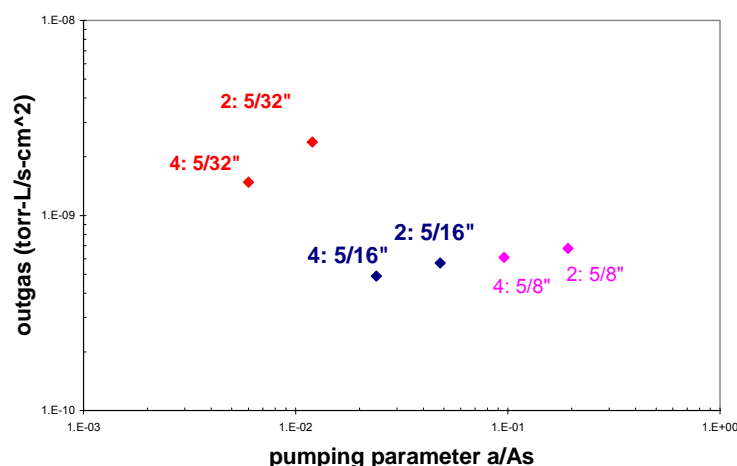
Fig. 103. Typical outgassing data for one material as a function of the pumping parameter.

The third project LANL is working on is the measurement of gettering performance. A second vacuum system (Fig. 104) was designed for these measurements. Based on results to date, a cryocooler will be added to the door to improve performance.

One minor task was to provide electrical design concept suitable for rotors with large time constants. An experiment was proposed to demonstrate the concept using the 1420 MVA LANL generator, which has an open circuit field constant similar to the superconducting rotor, i.e., a large inductance and a low resistance. This task is complete.

LANL is also investigating the use of heat pipes (Fig. 105) for removing heat from the HTS rotor and transferring the heat to the cryocooler. The effective thermal conductivity of a heat pipe is orders of magnitude greater than that of copper. This means that the temperature difference ΔT required to transfer a given amount of heat can be quite small. In the present application, both the rotor and heat pipe operate under the severe condition of high rotational rate.

Fig. 104. Image of vacuum system used for gettering measurements.

.
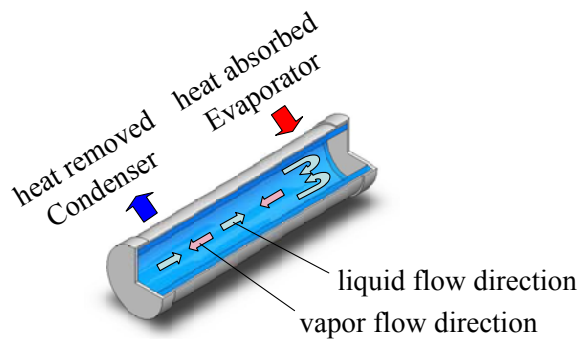
Fig. 105. Schematic illustration of the operating principal of the heat pipe. Liquid flows along the tube innerwall and vapor returns in the central area.

The modern day heat pipe was discovered at LANL in 1963. The existing and validated (over more than 20 years) heat pipe model has been extended to include rotational aspects, to evaluate performance capability, to identify performance issues and limits, and to design a model to validate experiments. This latter is based on similarity of performance via dimensional analysis. At present, a room temperature experiment is progressing. The equipment has been designed and is being procured.

The final topic being investigated is the affect of ac losses on conductor and system design. For instance, conductor ac losses impact steady state heat loads, transient fault condition response (coil stability, conductor protection), and excitation system choice. An ac loss model has been developed and is being used to compare with GE data on heat generation in the HTS rotor. The model includes the dc background magnetic field, dc transport current, superimposed ac ripple, and the Bi-2223 tape properties.

Future plans include further characterization of outgassing materials, of getter materials, and a long term prescription for vacuum maintenance based on outgassing and getter data and the GE design. The rotating heat pipe concept will be evaluated, with appropriately scaled room temperature experiments will be performed, compared to modeling, and incorporation of the rotor analyzed. Ac loss evaluation will extend to measurements on a GE coil. The affect on the GE rotor of the replacement of Bi-2223 with 2nd generation coated conductors will be analyzed.

2.2.2 Waste water treatment with magnetic separation SPI project
J.A. Waynert, F.C. Prenger, L.A. Worl, R.M. Wingo, T.Y. Ying, J.A. Stewart, D.E. Peterson, (DuPont): J.G. Bernard, C. Rey, (New Mexico State Univ.): M. Johnson

This is a SPI project with DuPont employee J.G. Bernard stationed at LANL and leading the effort there. Magnetic separation has received much attention recently due to industrial, medical and governmental interest in selective separation technologies. This is a technique in which magnetic particles are removed from a process stream as they pass through a region of imposed magnetic field. High gradient magnetic separation (HGMS) takes this technology further by using large magnetic field gradients generated on a matrix to accomplish separations of micron-sized particles. A schematic of the system is shown in Fig. 106.
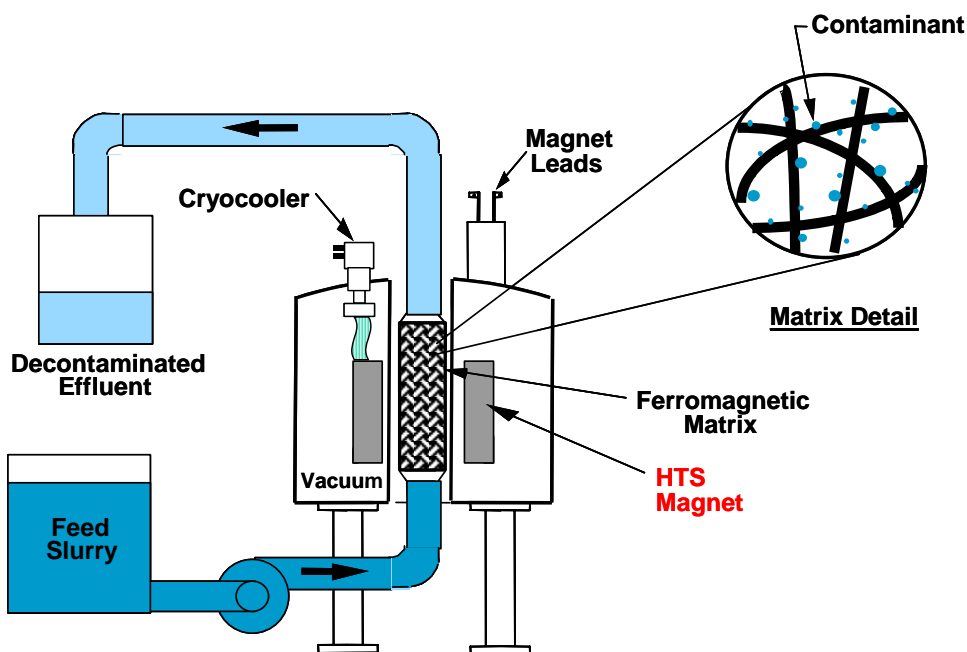
Fig. 106. Schematic of the HGMS process.

This technology has been shown to be very efficient at removing metal particles from such materials as kaolin clay and TiO_2. There are also many potential new market applications, such as wastewater treatment, water purification, medical/biological separations, and the capture of specific target compounds. One application with potential near term success is the removal of heavy metals from mine drainage water. There are thousands of mines in the USA with heavy metal drainage problems, endangering wildlife and humans through pollution of surface and ground water supplies for irrigation and domestic use. The market opportunity for this application is significant if the technique can be made cost effective.

An efficient and reliable high-temperature superconducting (HTS) magnet was used as the source of the magnetic field. It employs an HTS magnet wound from Bi-2223/Ag tape. It is 15.5 cm high with a 2.5 cm cold bore and is cooled by a two stage Gifford-McMahon cryocooler. Cooled to 40 K, the magnet can generate a central field of 2 T at a current of 120 A. This system provides significant advantages over conventional, resistive coil technology. Power usage is significantly reduced. HTS magnets can also be portable in a cryogen-free configuration with cooling requirements supplied by a cryocooler powered by electricity or another source. This portability can be important for

many applications, especially for temporary clean up or for use at a remote site. HTS magnets result in a smaller footprint than conventional systems, which is potentially less costly because less space is required, and support and auxiliary structures can be reduced in size and weight.

The first step of the magnetic separation process takes advantage of the properties of a class of compounds known as ferrites. When the metals in a ferrite are iron, it is known as magnetite (Fe_3O_4), or more precisely $FeO \bullet Fe_2O_3$, and contains iron in the +2 and +3 oxidations states. A wide range of ferrites containing other metals are also known. These are _ferrimagnetic_ crystalline materials that precipitate as they form and are only soluble in strongly acidic media.

The first step of this process involves the in-situ aerial oxidation of aqueous ferrous ions by oxygen in air that is bubbled through the system. When the required 1:2 stoichiometry is reached, a precipitate rapidly forms. This intermediate product is known as green rust (GR) and has a low magnetic susceptibility and is air (oxygen) sensitive.

$$Fe^{2+} + 2\,Fe^{3+} + 8\,OH^- \rightarrow GR\,(solid)$$
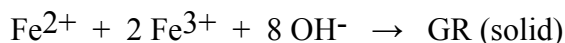
Next, the (GR) undergoes a rate limiting dehydration to form magnetite.

$$GR\,(solid) \rightarrow FeOFe_2O_3\,(solid) + 4\,H_2O$$

Other metals readily substitute for iron in this synthesis. A chemical reaction for the formation of metal-substituted magnetite is analogous to the formation of magnetite as follows:

$$M^{2+}_{(aq)} + 2\,Fe^{3+}_{(aq)} + 8\,OH^-_{(aq)} \rightarrow MO \bullet Fe_2O_{3(s)} + 4\,H_2O_{(l)}$$

or

$$Fe^{2+}_{(aq)} + Fe^{3+}_{(aq)} + M^{3+} + 8\,OH^-_{(aq)} \rightarrow FeO \bullet FeMO_{3(s)} + 4\,H_2O_{(l)}$$
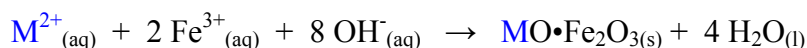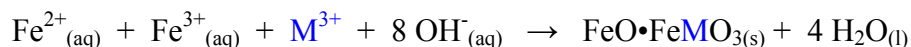
The advantages of the ferrite co-precipitation technique, relative to traditional chemical precipitation methods, include: 1) simultaneous removal of a wide variety of metal ions, 2) precipitates have chemical stability with little risk of subsequent acidic dissolution under environmental conditions.

Experiments have established that ferrite formation occurs very readily in nanopure water. Ferrite formation was also demonstrated at temperatures below 10°C that are often associated with mine drainage water, though it forms at a slower rate. However, in a realistic mine drainage simulant, dehydration of the GR intermediate to form ferrite was inhibited. After further experiments, it was determined that calcium ions in the simulant acted to "poison" the reaction by preventing GR dehydration. Since GR has only a very weak magnetic susceptibility, magnetic separation under these conditions is not feasible. Removal of calcium ions prior to magnetite formation was considered but deemed to be cost ineffective. Increasing the temperature or aging the GR for at least several hours helped to alleviate this problem, but these are not practical solutions for the treatment of large volumes of water.

In an attempt to circumvent the problem of calcium poisoning, the reaction was seeded with small amounts of pre-formed magnetite. It was hoped this would provide a surface upon which nucleation and further ferrite formation would take place. Initial experiments demonstrated that GR formed on the surface of the magnetite seed, producing particles

with magnetic properties suitable for magnetic separation. Full conversion to a high quality ferrite was accomplished by filtration followed by drying the solids under an inert atmosphere. XRD (x-ray diffraction) experiments have confirmed that the magnetic product is indeed a ferrite and not some other dark colored oxide. Toxic characteristic leaching procedure (TCLP) experiments show minimal heavy metal leaching using a scaled down version of the standard EPA test. This is a direct result of the ferrite stability, and allows for inexpensive disposal in a non-hazardous waste landfill. Failure to sufficiently dry a sample causes variable degrees of decomposition to a brown, amorphous product if it is exposed to air for long periods of time.

Step 2 of the process involves the magnetic separation of the magnetite seed/GR particles. The laboratory scale magnetic separator (Fig. 107) uses tubing and a peristaltic pump to transfer a suspension of the ferrite from a beaker through a cylindrical column containing a matrix of 430 series stainless steel wool. When the column is placed inside the bore of our HTS magnet at fields of up to 1.9 tesla, the magnetic gradients generated at the surface of the matrix act as a filter to remove the ferrites, while the "cleaned" effluent flows through and is collected. Because the matrix has a maximum capacity, it must be backflushed periodically to remove the collected ferrites before re-use.

Fig. 107. Photographs of HGMS apparatus. on the left is a view of the magnet power supply In the center is the HTS magnet and other apparatus. The column in which the separations occur is shown on the right. It fits in the warm bore of the magnet.

The efficacy of metal removal has been examined for many experiments using ICP (inductively coupled plasma spectroscopy). Results of these experiments demonstrate that residual metal concentrations after the seeded GR treatment meet the NPDES (National Pollution Discharge and Elimination System) limits for discharge to the environment. An example of the ICP results is shown in Fig. 108 where iron, manganese and zinc were effectively removed from a feed solution of mine drainage water. This process also works well for other metals of current interest, such as arsenic, lead, and cadmium.
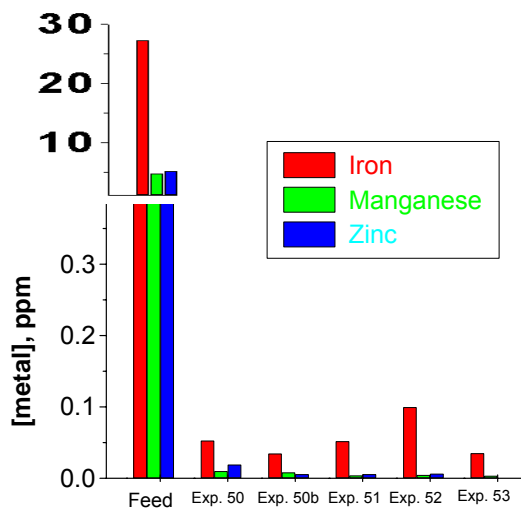
Fig. 108. Removal of typical metal species from water using the magnetite seed process.

There are a number of separator parameters that affect performance of the HGMS and need to be addressed. These include particle size, particle concentration, wastewater pH, type of stainless steel wool (ultra-fine to coarse) for the matrix, the applied magnetic field strength, the flow velocity in the column, and the residence time in the column.

For most experiments, the performance of the HGMS procedure was measured by recording the breakthrough volume for each experiment. This occurs when the capacity of the separator is reached and particles begin to escape. Breakthrough was defined as 1 ppm of particles collected in a 20 mL effluent vial as measured by a turbidimeter. In the experiments that follow, the breakthrough volume was limited by GR shearing from the seed during the magnetic separation and percolating through the separator. Developing ways to increase the seed/GR stability should increase the breakthrough volume.

In one set of experiments, with results shown in Fig. 109a, the rate of air bubbling during synthesis was varied. It is clear that this process needs to be controlled to achieve optimum breakthrough volumes. This process influences the quality of the seed/GR particle as well as the final ferrite product. In another experiment, the slurry is aged in and out of a magnetic field prior to HGMS. Aging in the absence of a field (Fig. 109b) has no affect, while aging in a small field dramatically increases the breakthrough volume. It is believed that magnetic aging increases the stability of the seed/GR particle. Fig. 110a illustrates the effect of varying the applied magnetic field during the separation process. It was found that the higher magnetic fields result in larger breakthrough volumes. This is expected since the magnetic field gradients increase with increasing field strength. Finally, Fig. 110b shows that breakthrough volumes increase with decreasing flow velocities in the column. Decreased flow velocities reduce the shear forces on the seed/GR particle, thereby increasing its stability. However, this does make for a slower process.
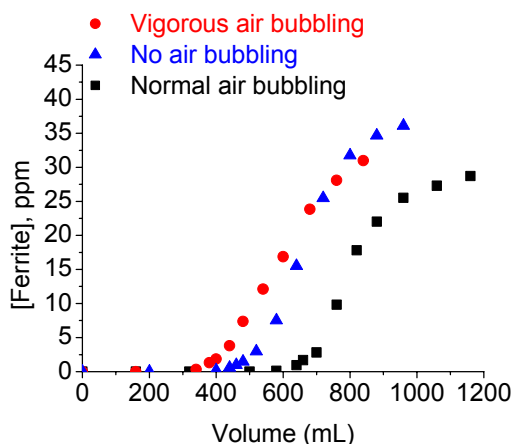
Fig. 109a. Breakthrough volume as a function of ferrite concentration for different levels of air flow.
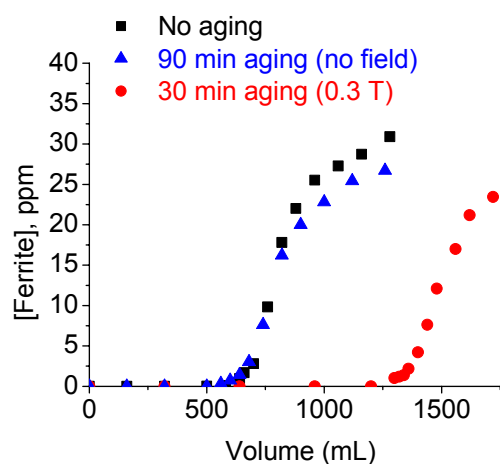
Fig. 109b. Breakthrough volume as a function of slurry aging time.
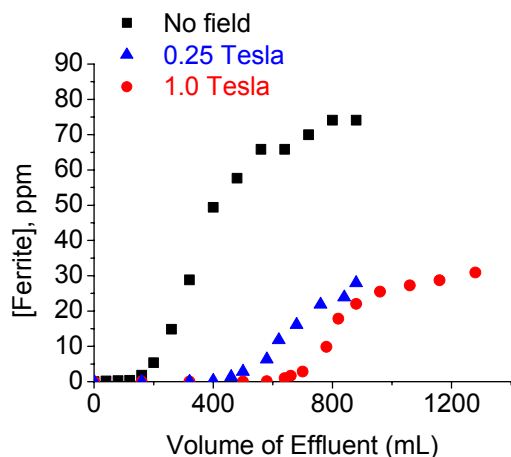
Fig. 110a. Breakthrough volume as a function of ferrite concentration for different levels of applied magnetic field.
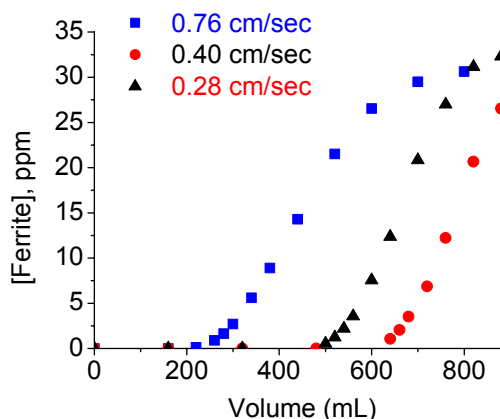
Fig. 110b. Breakthrough volume as a function of flow velocity.

In summary, two steps are necessary for effective removal of metals from wastewater. In step 1, metals are removed by synthesizing them into a ferrite. The seeded ferrite process makes it possible to do the HGMS before the conversion of green rust to ferrite. The ferrites are environmentally stable and can be disposed of inexpensively, and the effluent water can be released to the environment.

Future plans include a parameter sensitivity analysis for the ferrite process, optimizing the ferrite and HGMS process for a specific application and site, determining the scaling issues from laboratory to pilot plant, and establishing a pilot plant partner to demonstrate the technology in the field.

2.2.3 Cost effective, open geometry HTS MRI system SPI project

T.G. Holesinger, J.A. Kennison, J. Gallegos, J.O. Willis; (Oxford Superconducting Technology): K. Marken, H.P. Miao, M. Meinesz, S. Hong, (National Renewable Energy Laboratory): R.N. Bhattacharya

Magnetic resonance imaging (MRI) is the largest existing commercial application of superconductors. MRI provides a greatly expanded medical diagnostic capability while eliminating the need for harmful x-ray examinations. The largest obstacle to the wider use of MRI is the capital cost of the equipment. Oxford Instruments, the parent company of OST, has proposed to substantially reduce the capital cost for low field, open MRI magnet systems using dip coated Bi-2212. This lower cost end of the market is growing rapidly, and it is expected that high temperature superconductor (HTS) technology can have a substantial impact. Oxford and Siemens have constructed a 0.2 T open MRI system using water-cooled aluminum tape coils. Bi-based HTS materials are well suited to moderate field magnets in the 20-25 K range. The above two companies have done an initial demonstration using multifilament Bi-2223 coils. The project builds on this technical success but with a lower cost ($5-10/kA-m) conductor. The goal is to build a 0.2 T system operating in the 20-25 K range, with the ultimate commercial goal of 0.5 T or higher magnetic field.

This project is a collaboration among many organizations. Oxford Superconducting Technology is leading the project and developing the methods of producing commercial dip coated tape. SCI Engineered Materials is supporting the project by supplying the superconductor powder and optimizing, scaling and reducing costs in this area. Oxford Magnet Technology is designing and building the HTS MRI magnet and cryogenics. Siemens Medical Solutions will integrate the final system and perform imaging trials. , The National Renewable Energy Laboratory (NREL) is supporting conductor development, particularly through the use of alternative coating methods for higher performance. LANL supports conductor development, persistent joint development, and YBCO impact assessment.

To date, work at LANL has focused on superconducting properties, phase chemistry, and microstructural characterization of various conductor materials.

Fig. 111 shows the results of dc transport critical current (I_c) measurements on a bare (double sided surface coated) Bi-2212 with the sample immersed in boiling liquid neon at 26.4 K. Fig. 111a shows the angular dependence of the tape for several magnetic fields in the range 1-7 T. The current voltage I-V curves were fit to a power law $V/V_c = (I/I_c)^n$, where V_c is the voltage criterion (1 μV @ 1 cm). Values ranged from 6-9 at 1 T, 4-7 at 2 T, 2-7 at 3 T, and 3-10 at 6.9 T, for the angular ranges of I_c data shown in Fig. 111a. There is always a strong, direct correlation between n and I_c for these Bi-2212 tapes. Fig. 111b shows I_c and n as a function of magnetic field for field direction along the c axis (parallel to the tape normal). The dependence is power law like, and can be extrapolated to a zero field value of about 370 A. This is to be compared to the self-field I_c value at 4.2 K, determined by Oxford, of greater than 900 A for this high performance conductor.
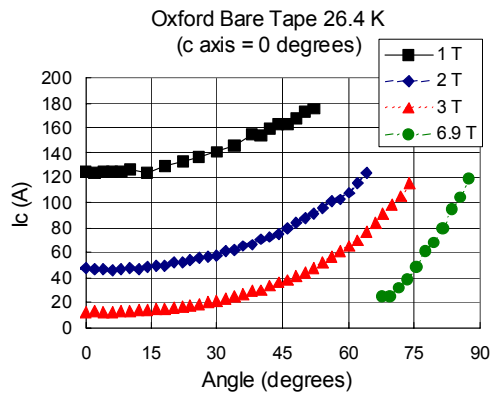
Fig. 111A. Angular dependence of an Oxford bare tape at liquid Ne temperature with applied magnetic field magnitude as a parameter.
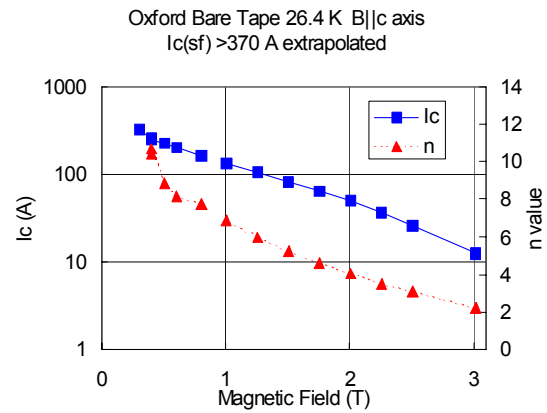
Fig. 111B. Magnetic field dependence of Ic and n for field parallel to the c axis of a bare tape at 26.4 K.

For accurate magnetic field generation, it is necessary for the current distribution across the tape width to be uniform. Oxford was concerned, based on I_c measurements of tapes cut into narrow strips, that this might be true. To investigate this possibility further by a different technique, tapes were patterned at LANL by coating the regions of interest with wax, immersing the tape in dilute HNO_3/H_2O and holding until uncoated regions were removed. Time in the etch was approximately 2-3 minutes. This is a relatively quick, convenient process to pattern regions 1-2 mm wide. Fig. 112 indicates schematically widths of the superconductor and bare Ag regions on the tape. The sample was measured in a bath of pumped liquid nitrogen (LN2) near 65 K and in liquid helium at 4.0 K. The BSCCO widths for the various sections are shown in Table 1. The I_c was calculated per unit width to make the results comparable; these and the n values $[(V/V_c) = A(I/I_c)^n]$.are collected in Table 1. The conclusion is that the current densities were found to be higher in the center of the tape than at the edges at both 4 K and at 64 K. Another tape patterned with somewhat wider segments showed similar center/edge dependencies when measured at 64 K only. The ratios of critical currents $K_c(4\ K)/K_c(26\ K)$ was found to be on the order of 50-60 for the good regions.
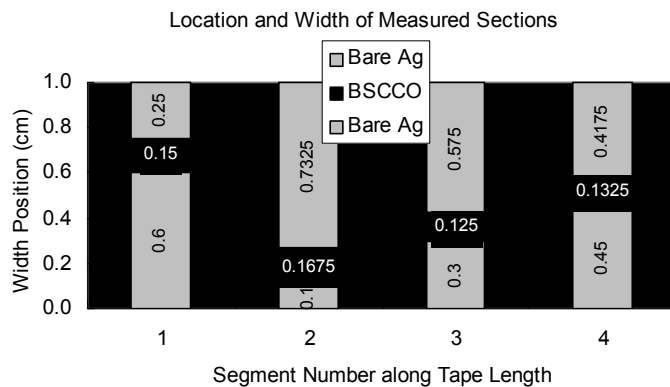
Fig. 112. Schematic of centimeter long patterned superconductor tape widths along the length of a Bi-2212 tape.

Table 1. Critical currents of patterned Bi-2212 tape

Segment #	1	2	3	4
Location	Midwidth	Near edge	Midwidth	Center
Width (cm)	0.15	0.1675	0.125	0.133
K_c(64K) (A/cm)	9.67	0.81	11.76	8.38
K_c(4K) (A/cm)	493.3	30.4	549.6	558.5
K_c(4K)/K_c(64K)	51.03	37.78	46.73	66.67

Electron microscopy, both SEM and TEM, were used to investigate all aspects of the conductor, beginning with substrate interactions, and ending with final phase assemblages and microstructure. Fig. 113 shows a bare tape of Bi-2212 on a low cost, silver clad Ni substrate. The micrograph shows an oxidation layer $\sim$ 10 μm thick on the Ni surface and the presence of Ag precipitates in the BSCCO.
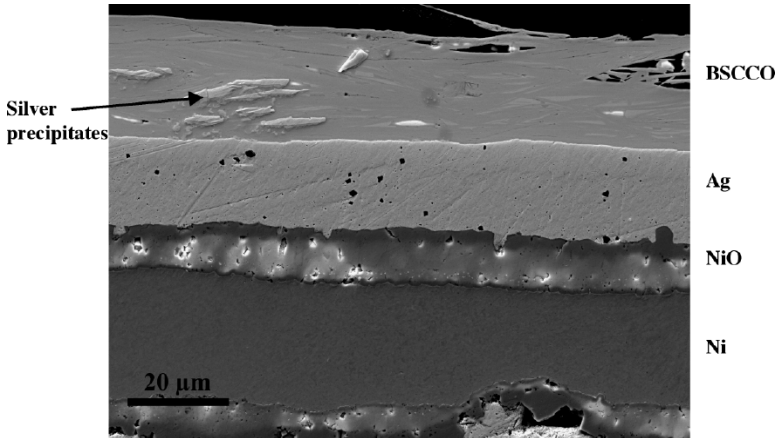
Fig. 113. SEM image of a bare Bi-2212 film on an Ag-clad Ni substrate. This 1 cm wide film had 4.2 K, self field performance of 746 A and 4234 A/mm^2.

Examination of sheathed tapes showed variation in the phase assemblage of the films. This suggests that there may also be spatial variations in the film stoichiometry. Fig. 114a shows an SEM image of the full transverse cross section of a sheathed tape with 4.2 K performance of 750 A and 3814 A/mm^2. With a Ag-clad Ni core. Fig. 114b shows a region with Bi-2212, Bi-2201 and a few alkaline earth cuprates (AECs). Fig. 114c shows a different region of the same tape with Bi-2212, AECs, copper free phases, and little Bi-2201. In either case, the measured composition of the Bi-2212 phase is the same.
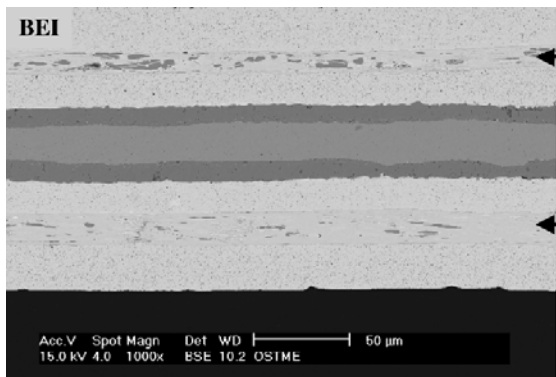
Fig. 114a. Backscattered electron image (BEI) of a sheathed Bi-2212 tape. The arrows at the right point to the location of the HTS layer. The micron bar at bottom indicates 50 μm.
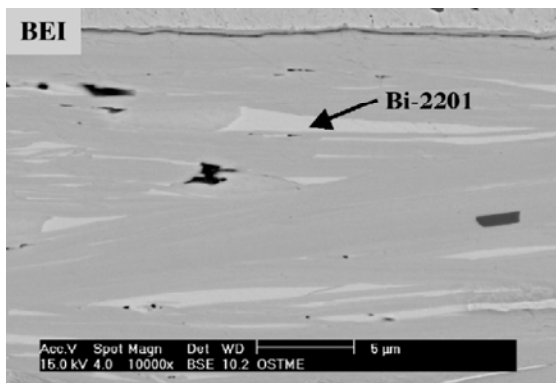
Fig. 114b. Expanded view of the sheathed tape showing a region with primarily Bi-2212 and Bi-2201 phases.
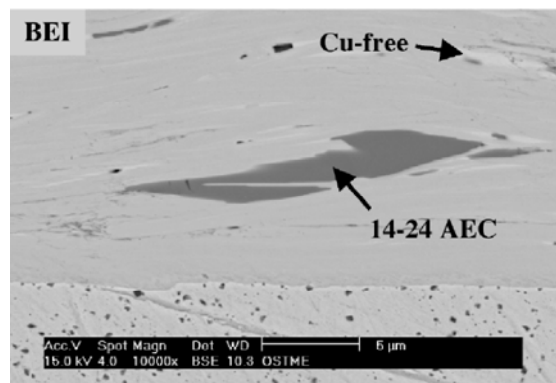
Fig. 114c. Expanded view of the sheathed tape showing a region with Bi-2212, alkaline earth cuprates, and copper free phase.

Substrate defects and their effects on film development and substrate/film interactions were also examined. Fig. 115a shows a region where a liquid phase from the film forms a "pipe" (indicated by the arrows) through the Ag layer down to the NiO interface. These pathways are relatively rare, suggesting point breakthroughs. The liquid phase penetration results in grain liftoff and densification of the NiO layer. The material in the "pipe" is similar in composition to Bi-2201 (Fig. 115b).
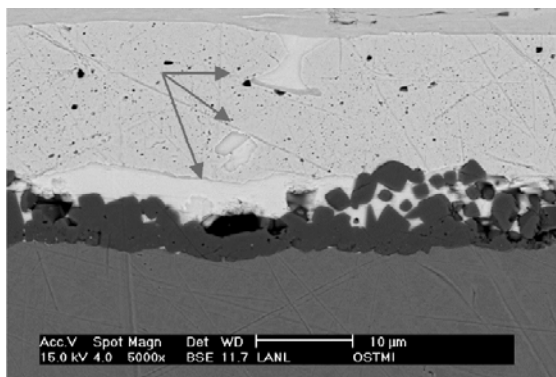
Fig. 115a. Liquid phase penetration of the NiO layer resulted here in grain liftoff and densification of the NiO layer.
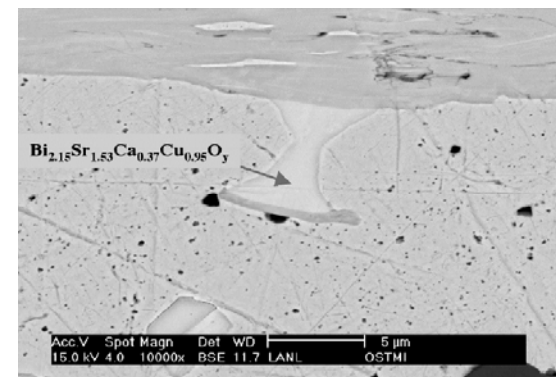
Fig. 115b. Material in the "pipe" region is similar in composition to Bi-2212

90

Transmission electron microscopy (TEM) is used to examine the fine-grain defect structure and identify potential current limiting mechanisms. Figs. 116a and 116b show TEM images of a high performance bare Bi-2212 tape. A number of amorphous phase are observed to penetrate grains or to coat basal plane grain boundaries. However, the Bi-2212 grains are mostly free of intergrowths. This could be a residual effect of the solidification process.
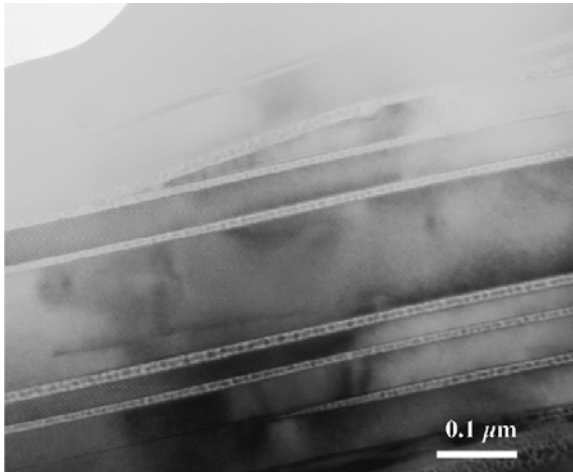
Fig. 116a. High-resolution image of the superconductor core of a tape with 4.2 K, self field performance of >1048 A, and >6334 A/mm^2.
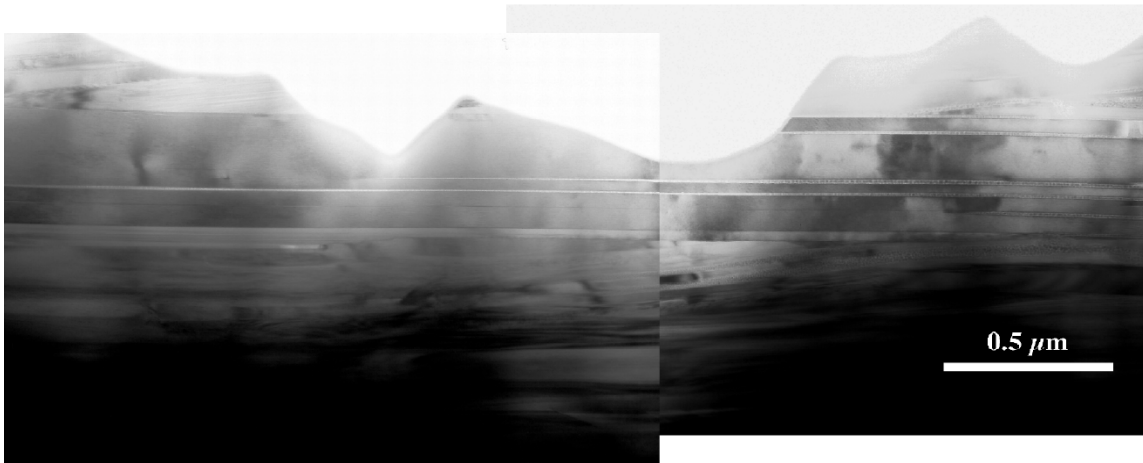
Fig. 116b. TEM image of Bi-2212 grains, mostly free of intergrowths for the same tape as in 6a.

To summarize, work at LANL on the MRI project has largely focused on superconductor and microstructural characterization. The results of this work have been used to help in the optimization of the conductor fabrication process and as reference data for the design of the magnet for the MRI.

3. Fiscal Year 2003 Publications

3.1. Journal Articles Published

"Role of $SrRuO_3$ buffer layers on the superconducting properties of $YBa_2Cu_3O_7$ films grown on polycrystalline metal alloy using a biaxially oriented MgO template,"
Q.X. Jia, S.R. Foltyn, P.N. Arendt, J.R. Groves, T.G. Holesinger, M.E. Hawley, and P. Lu,
Applied Physics Letters **81**, 4571 (2002).

"Flux pinning enhancement in ferromagnetic and superconducting thin film multilayers,"
D.B. Jan, J.Y. Coulter, M. Hawley, L. Bulaevskii, M.P. Maley, Q.X. Jia, B.B. Maranville, F. Hellman, X.Q. Pan,
Applied Physics Letters **82**, 778 (2003).

"Microstructure and high critical current of powder-in-tube MgB_2,
A.C. Serquis, L. Civale, D.L. Hammon, X.Z. Liao, J.Y. Coulter, Y.T. Zhu, D.E. Peterson, F.M. Mueller,
Applied Physics Letters **82**, 1754 (2003)

"Hot isostatic pressing of powder in tube MgB_2 wires,"
A. Serquis, L. Civale, D.L. Hammon, X.Z. Liao, Y.T. Zhu, D.E. Peterson, F.M. Mueller, M. Jaime, V.F. Nesterenko, Y. Gu,
Applied Physics Letters **82**, 2847 (2003).

"Strongly coupled critical current density values achieved in $YBa_2Cu_3O_{7-d}$ coated conductors with near-single crystal texture,"
S.R. Foltyn, Q.X. Jia, H. Wang, J.L. Driscoll, S. Kreiskott, R.F. DePaula, L. Stan, J.R. Groves, P.C. Dowden,
Applied Physics Letters **82**, 4519 (2003)

"Microwave performance of high-density bulk MgB_2,"
A.T. Findikoglu, A. Serquis, L. Civale, X.Z. Liao, M.E. Hawley, F.M. Mueller, V.F. Nesterenko, Y. Gu,
Applied Physics Letters **83**, 108 (2003)

"The role of a superconducting seed layer in the structural and transport properties of $EuBa_2Cu_3O_{7-x}$ films,"
Q.X. Jia, S.R. Foltyn, P.N. Arendt, H. Wang, J.L. MacManus-Driscoll, J.Y. Coulter, Y. Lin, M.P. Maley, M.E. Hawley, K. Venkataraman and V.A. Maroni,
Applied Physics Letters **83**, 1388 (2003).

"Reflection high energy electron diffraction experimental analysis of polycrystalline MgO films with grain size and orientation distributions,"
R.T. Brewer, H.A. Atwater, J.R. Groves, and P.N. Arendt,
Journal of Applied Physics **93**, 205 (2003).

"Mg(B,O)$_2$ precipitation in MgB$_2$,"
 X.Z. Liao, A.C. Serquis, Y.T. Zhu, J.Y. Huang, L. Civale, D.E. Peterson, F.M. Mueller, H.F. Xu,
 Journal of Applied Physics **93**, 6208 (2003).

"Role of excess Mg and heat treatments on microstructure and critical current of PIT MgB$_2$ wires,"
 A. Serquis, L. Civale, D.L. Hammon, X.Z. Liao, J.Y. Coulter, Y.T. Zhu, D.E. Peterson, and F.M. Mueller,
 Journal of Applied Physics **94**, 4024 (2003).

"Characterization of superconducting SmBa$_2$Cu$_3$O$_7$ films grown by pulsed laser deposition,"
 Q.X. Jia, S.R. Foltyn, J.Y. Coulter, J.F. Smith, M.P. Maley,
 Journal of Materials Research **17**, 2599 (2003).

"Growth of thick YBa$_2$Cu$_3$O$_{7-d}$ films carrying a critical current over 230 A/cm on single LaMnO$_3$-buffered ion-beam assisted deposition MgO substrates,"
 M. Paranthaman, T. Aytug, D.K. Christen, P.N. Arendt, S.R. Foltyn, J.R. Groves, L. Stan, R.F. DePaula, H. Wang, T.G. Holesinger,
 Journal of Materials Research **18**, 2055 (2003).

"AC losses in prototype multistrand conductors for warm dielectric cable design,"
 J.O. Willis, M.P. Maley, H.J. Boenig, G. Coletta, R. Mele, and M. Nassi,
 IEEE Transactions on Applied Superconductivity **13**, 1960 (2003).

"Restoration and testing of an HTS fault current controller,"
 J.A. Waynert, H.J. Boenig, C.H. Mielke, J.O. Willis, and B.L. Burley
 IEEE Transactions on Applied Superconductivity **13**, 1984 (2003).

"Fabrication of high J$_c$ YBa$_2$Cu$_3$O$_{7-d}$ tapes using the newly developed lanthanum manganate single buffer layers,"
 M.P. Paranthanam, T. Aytug, S. Kang, R. Feenstra, J.D. Budai, D.K Christen, P.N. Arendt, L. Stan, R.F. DePaula, S.R. Foltyn, T.G. Holesinger, J.R. Groves,
 IEEE Transactions on Applied Superconductivity **13**, 2481 (2003).

"Accelerated coated conductor program at Los Alamos National Laboratory,"
 V. Matias, B.J. Gibbons, S. Kreiskott, L.N. Bronisz, D.E. Peterson,
 IEEE Transactions on Applied Superconductivity **13**, 2488 (2003).

"Variable temperature scanning laser microscopy of wider width high temperature superconducting films,"
 L.B. Wang, M.B. Price, C. Kwon, Q.X. Jia,
 IEEE Transactions on Applied Superconductivity **13**, 2611 (2003).

"Improvement of IBAD MgO template layers on metallic substrates for YBCO HTS deposition,"
J.R. Groves, P.N. Arendt, S.R. Foltyn, Q.X. Jia, T.G. Holesinger, L.A. Emmert, R.F. DePaula, P.C. Dowden, L. Stan,
IEEE Transactions on Applied Superconductivity **13**, 2651 (2003).

"Growth and characterization of $SrRuO_3$ buffer layer on MgO template for coated conductors,"
Q.X. Jia, S.R. Foltyn, P.N. Arendt, T.G. Holesinger, J.R. Groves, M. Hawley,
IEEE Transactions on Applied Superconductivity **13**, 2655 (2003).

"Spatial distribution analyses of critical temperature in epitaxial Y-Ba-Cu-O film using variable temperature scanning laser microscopy,"
C. Kwon, L.B. Wang, S. Seo, B.H. Park, Q.X. Jia,
IEEE Transactions on Applied Superconductivity **13**, 2894 (2003).

"The influence of structural defects on intragranular critical currents of bulk MgB_2,"
A.C. Serquis, X.Z. Liao, L. Civale, Y. T. Zhu, J.Y. Coulter, D. E. Peterson, F. M. Mueller,
IEEE Transactions on Applied Superconductivity **13**, 3068 (2003).

"High critical currents in powder in tube MgB_2 wires: influence of microstructure and heat treatments,"
L. Civale, A.C. Serquis, D.L. Hammon, X.Z. Liao, J.Y. Coulter, Y.T. Zhu, T.G. Holesinger, D.E. Peterson, F.M. Mueller,
IEEE Transactions on Applied Superconductivity **13**, 3347 (2003).

"Bridge-type fault current controller-A new FACTS controller,"
H.J. Boenig, C.H. Mielke, B.L. Burley, J.A. Waynert, J.O. Willis,"
IEEE 2002 Power Engineering Society Meeting Proceedings, IEEE, Piscataway, NJ, Vol. 1, pp. 455-560, 2002.

"Imaging transport current distribution in high temperature superconductors using room temperature scanning laser microscope,"
B.E. Klein, S. Seo, C. Kwon, B.H. Park, Q.X. Jia,
Reviews of Scientific Instruments **73**, 3692 (2002).

"Defect structures in MgB_2 wires introduced by hot isostatic pressing,"
X.Z Liao, A. Serquis, Y.T. Zhu, L. Civale, D.L. Hammon, D.E. Peterson, F.M. Mueller, V.F. Nesterenko and Y. Gu,
Superconductor Science and Technology **16**, 799 (2003).

"Continuous electropolishing of Hastelloy substrates for ion-beam assisted deposition of MgO,"
S. Kreiskott, P. Arendt, L. Bronisz, S. Foltyn, V. Matias,
Superconductor Science and Technology **16**, 2055 (2003).

"Recent progress in continuously processed IBAD MgO template meters for HTS
applications,"
J.R. Groves, P.N. Arendt, S.R. Foltyn, Q.X. Jia, T.G. Holesinger, H. Kung, R.F.
DePaula, P.C. Dowden, E.J. Peterson,
Physica C **382**, 43 (2002).

"High critical current MOD ex situ YBCO films on RABiTS and MgO-IBAD templates,"
X. Li, M.W. Rupich, W. Zhang, N. Nguyen, T. Kodenkandath, U. Schoop, D.T.
Verbelyi, C. Thieme, M. Jowett, P.N. Arendt,
Physica C **390**, 249 (2003)

"Lateral epitaxial growth of $Ba_{0.6}Sr_{0.4}TiO_3$ thin films,"
J.-S. Lee, S.Y. Lee, Q.X. Jia,
Integrated Ferroelectrics **55**, 933 (2003).

"Microstructural properties of $Ba_{0.5}\,Sr_{0.4}TiO_3/RuO_2$ multilayers grown on MgO and YSZ
by pulsed laser deposition,"
P.Lu, J.-S. Lee, Q.X. Jia,
Integrated Ferroelectrics **55**, 965 (2003).

"Conductive metal oxide thin films,"
Q.X. Jia,
Handbook of Thin Films, Vol. 4, Chapt. 13, ed. H. Nalwa, Academic Press, (2002).

"IBAD template films for HTS coated conductors,"
Paul N. Arendt,
Book Chapter for **Next Generation High Temperature Superconducting Wires**,
Plenum Press, ed. A. Goyal, New York, 2003.

3.2. Journal Articles Submitted for Publication

"Thickness dependence of AC losses in circular disks of $YBa_2\,Cu_3\,O_7$ films in
perpendicular magnetic fields,"
S.R. Foltyn, H. Wang, M. Suenaga, Q. Li, Z. Ye; M. Iwakuma, K. Toyota, F. Funaki,
J. Clem,
Submitted to *Applied Physics Letters*.

"Lateral epitaxial growth of (Ba,Sr)TiO_3 thin films,"
J.-S. Lee, H. Wang, S.R. Foltyn, Q.X. Jia,
Submitted to *Applied Physics Letters*.

"Effect of crystallinity on the transport properties of $Nd_{0.67}Sr_{0.33}MnO_3$ thin films,"
H. Wang, L. Zhang, B.J. Gibbons, Y. Lin, J. MacManus-Driscoll, P.N. Arendt, S.R.
Foltyn, Q.X. Jia, M. Hundley, J.D. Thompson,
Submitted to *Applied Physics Letters*.

"Role of beam divergence and ion-to-molecule flux ratio in ion-beam assisted deposition texturing of MgO,"
   A.T. Findikoglu, S. Kreiskott, P.M. TeRiele, V. Matias,
   Paper submitted to *Journal of Materials Research*.

"Microstructural characterization of high J_c YBCO thick films grown at very high rates and high temperatures by PLD,"
   A. Berenov, N. Malde, Y. Bugoslavsky, L.F. Cohen, S. Foltyn, P. Dowden, J. Ramirez-Castellanos, J.M. Gonzales-Calbert, M. Vallet-Regi, J.L. MacManus-Driscoll,
   Paper submitted to *Journal of Materials Research.*

"Underground wireless communications using high-temperature superconducting receivers,"
   J. Vasquez, V. Rodriguez, D. Reagor,
   Submitted to *IEEE Transactions on Applied Superconductivity*.

"Strain effect on the critical superconducting temperature of MgB_2,"
   X.Z. Liao, A.C. Serquis, YT. Zhu, D.E. Peterson, F.M. Mueller, H.F. Xu,
   Submitted to *Superconductor Science and Technology*.

"Reel-to-reel preparation of ion-beam assisted deposition (IBAD) MgO based coated conductors,"
   S. Kreiskott, V. Matias, S.R. Foltyn, P.N. Arendt, B.J. Gibbons, J.Y. Coulter, P.C. Dowden, C. Sheehan,
   Submitted to *Superconductor Science and Technology*.

"Anistropic scaling in $YBa_2Cu_3O_7$ crystals with columnar defects,"
   L. Civale, A. Silhanek,
   Submitted to *Journal of Low Temperature Physics*.

"Understanding high critical currents in $YBa_2Cu_3O_7$ thin films and coated conductors,"
   L. Civale, B. Maiorov, A. Serquis, J.O. Willis, J.Y. Coulter, H. Wang, Q.X. Jia, P.N. Arendt, J. MacManus, M.P. Maley, S.R. Foltyn, M. Jaime,
   Submitted to *Journal of Low Temperature Physics*.

"Bose-glass like phases in oriented-twin $YBa_2Cu_3O_7$ crystals,"
   B. Maiorov, E. Osquiguil,
   Submitted to *Journal of Low Temperature Physics*.

"Low temperature elastic constants of polycrystalline MgB_2,"
   U. Harms, A. Serquis, R.B. Schwarz,
   Paper submitted to *Journal of Superconductivity*.

"Microstructural properties of $Ba_{0.6}Sr_{0.4}TiO_3$ films doped with TiO_2,"
   P. Lu, M. Tang, Q.X. Jia,
   Paper submitted to *Journal of Thin Solid Films*.

"Angular dependent vortex dynamics in superconductors with columnar defects,"
    L. Civale, A. Silhanek, G. Pasquini,
    Submitted to **Frontiers in Superconductivity Research**, Nova Science Publishers..

"Processing and characterization of MgB_2,"
    A. Serquis, X.Z. Liao,
    Submitted to **Frontiers in Superconductivity Research**, Nova Science Publishers.

3.3. Other Publications and Conference Abstracts

"2003 DOE Wire Workshop Summary,"
    T.G. Holesinger, M. Parathaman, S. Dorris,
    Submitted to the Energetics Review and DOE/Jim Daley.

"Superconductivity Program for Electric Systems Annual Progress Report for Fiscal Year 2001,"
    D.E Peterson, J.O. Willis,
    Submitted to US Department of Energy, Energy Efficiency & Renewable Energy.

"Superconductivity Program for Electric Systems Annual Progress Report for Fiscal Year 2002,"
    D.E. Peterson, J.O. Willis,
    Submitted to US Department of Energy, Energy Efficiency & Renewable Energy.

"Intergrain J_c changes in YBCO tapes with elevated temperature proton irradiation,"
    E. Ibragimova, M. Kirk, S. Foltyn, S. Ferguson, B. Fisher,
    Abstract for the MRS 2002 Fall Meeting, Boston, MA, December 1-6, 2002.

"Phase equilibria in the $SrO-CuO-TiO_2$ system: potential application to high temperature superconductors (HTS)"
    Alicia Ayala, T.G. Holesinger,
    Abstract for the MRS 2002 Fall Meeting, Boston, MA, December 1-6, 2002.

"High critical current MOD-YBCO films on MgO-IBAD substrates,"
    X. Li, W. Zhang, T. Kodenkandath, N. Nguyen, U. Schoop, M.W. Rupich, S.R. Foltyn, P.N. Arendt, M.P. Paranthaman, T. Aytug,
    Abstract for the MRS 2002 Fall Meeting, Boston, MA, December 1-6, 2002.

"Anisotropic Scaling Analysis of Critical Currents in RBCO Coated Conductors,"
    L. Civale, J.Y. Coulter, J.O. Willis, A. Serquis, Q.X. Jia, S.R. Foltyn, P.N. Arendt, D.E. Peterson,
    Abstract for the March Meeting of the American Physical Society, Austin, TX, March 3-7, 2003.

"Critical Currents, Vortex Dynamics and Microstructure in MgB_2,"
    A. Serquis, L. Civale, X.Z. Liao, M.P. Maley, Y.T. Zhu, D.E. Peterson, F.M. Mueller, S.S. Indrakanti, V.F. Nesterenko,
    Abstract for the March Meeting of the American Physical Society, Austin, TX, March 3-7, 2003.

"Spin Density Wave Excitations in the Specific Hear of $La_2CuO_{4.11}$ Single Crystals,"
G. Jorge, M. Jaime, L. Civale, B. Zink, F. Hellman, B. Khaykovich, Y.S. Kastner, Y.S. Lee, R.J. Birgeneau,
Abstract for the March Meeting of the American Physical Society, Austin, TX, March 3-7, 2003.

"Lateral Epitaxial Growth of $(Ba,Sr)TiO_3$ Thin Films,"
J.-S. Lee, Q.X. Jia,
Abstract for the International Symposium on Integrated Ferroelectrics 2003, Colorado Springs, CO, March 9-12, 2003.

"Modulation of Energy Bandgap of ZNO Thin Films Grown by Pulsed Laser Deposition,"
S.Y. Lee, Y. Li, Q.X. Jia,
Abstract for the Spring MRS Meeting, San Francisco, CA, April 21-25, 2003.

"Current progress in YBCO coated conductors using IBAD MgO template layers,"
J. R. Groves, P.N. Arendt, S.R. Foltyn, Q.X. Jia, T.G. Holesinger, L.A. Emmert, R.F. DePaula, P.C. Dowden, L. Stan, Rhett T. Brewer, Harry Atwater,
Abstract for the 105th Annual Meeting & Exposition of the American Ceramic Society, Nashville, TN, April 27-30, 2003.

"YBCO/Nd_2CuO_4/NiO/Ni Coated Conductors Fabricated by a Fast All-Liquid-Phase Processing Route,"
X.Qi, Z. Lockman, R. Tomov, A. Kursumovic, R. Huehne, B.A. Glowacki, J.E.Evetts, J.L. MacManus-Driscoll,
Abstract for the American Ceramic Society, 105th Annual Meeting, Nashville, TN April 27-30, 2003.

"Growth and Characterization of Barium Stontium Titanate-Based Thin Films for Tunable Microwave Devices,"
Q.X. Jia, B.H. Park, B.J. Gibbons, P. Lu,
Abstract for the American Ceramic Society, 105th Annual Meeting, Nashville, TN April 27-30, 2003.

"Growth and Characterization of Superconducting Films for Coated Conductors,"
Q.X. Jia, S.R. Foltyn, P.N. Arendt, T.G. Holesinger,
Abstract for the American Ceramic Society, 105th Annual Meeting, Nashville, TN April 27-30, 2003.

"Wire Development Group (WDG) Research towards Advanced HTS Wire Technologies,"
T.G. Holesinger, A. Malozemoff, E.E. Hellstrom, D. Larbalestier, V. Maroni,
Abstract for USDOE Superconductivity for Electric Systems 2003 Annual Peer Review, July 2003.

"Cost Effective. Open Geometry HTS MRI System,"
    T.G. Holesinger, K. Marken, F. Davis, Scott Campbell, Raghu Bhattacharya,
    Abstract for USDOE Superconductivity for Electric Systems 2003 Annual Peer
    Review, July 2003.

"Materials and Intrinsic Properties in the J_c Dependence on Thickness of Ex Situ YBCO
    Coated Conductors,"
    T.G. Holesinger, R. Feenstra, M. Feldmann,
    Abstract for USDOE Superconductivity for Electric Systems 2003 Annual Peer
    Review, July 2003.

"$(Bi,Pb)_2Sr_2Ca_2Cu_3O_y$ Superconductors: Novel Powder Processing for Liquid Phase
    Sintering of Practical Conductors,"
    M. Archuleta, T.G. Holesinger, A. Ayala, J.A. Kennison, J. Gallegos,
    Abstract for the Symposium 2003-Highlighting Student and Postdoctoral Research,
    Los Alamos, August 2003.

"$Bi_2Sr_2CaCu_2O_y$ Superconductors: Powder Synthesis and Conductor Fabrication,"
    J. Gallegos, T.G. Holesinger, A. Ayala, J.A. Kennison, M. Archuleta,
    Abstract for the Symposium 2003-Highlighting Student and Postdoctoral Research,
    Los Alamos, August 2003.

"Reel-to-Reel Preparation of Ion-Beam Assisted Deposition (IBAD) MgO Based Coated
    Conductors,"
    S. Kreiskott, V. Matias, S.R. Foltyn, P.N. Arendt, B.J. Gibbons, J.Y. Coulter, P.C.
    Dowden, C. Sheehan,
    Abstract for EUCAS 2003, Sorrento, Italy, Sept. 15-18, 2003.

"Understanding High Critical Currents in $YBa_2Cu_3O_7$ Thin Films,"
    L. Civale, A. Serquis, B. Maiorov, J.O. Willis, J.Y. Coulter,
    Abstract for the International Workshop Pushing Physics at Low Temperatures,
    Bariloche, Argentina, September 25-26, 2003.

"Microstructural Development in $YBa_2Cu_3O_7$ Coated Conductors Based on Ex-Situ
    YBCO Conversion Processes,"
    T.G. Holesinger, R. Feenstra, A. Gappud, E. Specht, S. Kim, M Feldmann, D.
    Larbalestier, D. Verebelyi, W. Zhang, S. Li, M. Rupich,
    Abstract for the 204th Meeting of the Electrochemical Society, Orlando, FL, Oct. 3-8,
    2004.

"TEM Studies of Interfacial Microstructures in $YBa_2Cu_3O_7$ Coated Conductors,"
    T.G. Holesinger, B.J. Gibbons, S.R. Foltyn, P.N. Arendt, V. Matias, Q.X. Jia, R.
    Feenstra, A.A. Gapud, E. Specht, W. Zhang, X. Li, M. Rupich,
    Abstract for the 204th Meeting of the Electrochemical Society, Orlando, FL, Oct. 3-8,
    2004.

"Effect of the Surface and Interface on the Superconducting Properties of $REBa_2Cu_3O_7$ Films,"
Q.X. Jia, S.R. Foltyn, J. MacManus-Driscoll, H. Wang, P.N. Arendt, V. Maroni,
Abstract for the 204th Meeting of the Electrochemical Society, Orlando, FL, Oct. 3-8, 2004.

"Chemical Routes to Increasing Low Field and High Field Pinning in Epitaxial $REBa_2Cu_3O_7$ Films,"
J. McManus-Driscoll, S.R. Foltyn, Q.X. Jia, H. Wang, D.E. Peterson,
Abstract for the 204th Meeting of the Electrochemical Society, Orlando, FL, Oct. 3-8, 2004.

"Angular Dependent Vortex Pinning Mechanisms in $YBa_2Cu_3O_7$ Coated Conductors,"
L. Civale, J.O. Willis, J.Y. Coulter, A. Serquis, B. Mairorov, Q.X. Jia, H. Wang, S.R. Foltyn, J. MacManus-Driscoll, P.N. Arendt, M.P. Maley,
Abstract for the 16th International Symposium on Superconductivity (ISS 2003), Tsukuba, Japan, October 27-29, 2003.

"Improved Critical Currents in a Bi-2223/Silver Coil Using Splayed Columnar Defects,"
J.O Willis, J.Y. Coulter, M.P Maley, J.U. Ullmann,
Abstract for the 16th International Symposium on Superconductivity (ISS 2003), Tsukuba, Japan, October 27-29, 2003.

"YBCO Coated Conductors based on IBAD MgO Templates,"
P.N. Arendt, S.R. Foltyn, Q.X. Jia, L. Civale, R. DePaula, L. Stan, H. Wang, J.R. Graoves, P. Dowden, S. Kreiskott, J.Y. Coulter,
Abstract for the 16th International Symposium on Superconductivity (ISS 2003), Tsukuba, Japan, October 27-29, 2003.

"Magnesium Oxide Templates for YBCO Coated Conductors,"
P.N. Arendt, J.R. Groves, S.R. Foltyn, Q.X. Jia, T.G. Holesinger, L.A. Emmert, R. DePaula, P.C. Dowden L. Stan, J.Y. Coulter,
Abstract for the 11th Japan-US Workshop on High-Tc Superconductors, Shonan Village Center, Kanagawa, Japan, October 31-November 2, 2003.

"Critical current anisotropy of YBCO Coated Conductors,"
J.O. Willis, L. Civale, B. Maiorov, A. Serquis, J. Y. Coulter, J. L. MacManus-Driscoll, P. N. Arendt, and S. R. Foltyn
Abstract for the 11th Japan-US Workshop on High-Tc Superconductors, Shonan Village Center, Kanagawa, Japan, October 31-November 2, 2003.

"Nanoparticle incorporated superconductor Bi-2212 Films,"
R.N. Bhattacharya, P. Spagnol, J. Chen, M. Hanping, K. Marken, and J.O. Willis,
Abstract for the 11th Japan-US Workshop on High-Tc Superconductors, Shonan Village Center, Kanagawa, Japan, October 31-November 2, 2003.

100

"Processing and Characterization of Powder in Tube MgB_2 Wires,"
A. Serquis, L. Civale, X.Z. Liao, Y.T. Zhu, D.E. Peterson, F.M. Mueller, D.L. Hammon, V.F. Nesterenko
Abstract for the MRS 2003 Fall Meeting, Boston, MA, Dec. 1-5, 2003.

"Angular Dependence of Critical Current in $DyBa_2Cu_3O_7$ Films with Naturally Grown Inclined Correlated Defects,"
B. Maiorov, J.Y. Coulter, J.O. Willis, A. Serquis, L. Civale,
Abstract for the MRS 2003 Fall Meeting, Boston, MA, Dec. 1-5, 2003.

"Power Law Analysis of Critical Current Measurements of YBCO Coated Conductors,"
J.Y. Coulter, L. Civale, B. Maiorov, A. Serquis, J.O. Willis,
Abstract for the MRS 2003 Fall Meeting, Boston, MA, Dec. 1-5, 2003.

"Identification of Pinning Mechanisms in $YBa_2Cu_3O_7$ Coated Conductors,"
L. Civale, J.O. Willis, J.Y. Coulter, A. Serquis, B. Maiorov, Q.X. Jia, Haiyan Wang, S.T. Foltyn, J.L. MacManus-Driscoll, P.N. Arendt, M.P. Maley,
Abstract for the MRS 2003 Fall Meeting, Boston, MA, Dec. 1-5, 2003.

"Comparative Study of the Through-Thickness Jc in Two In-situ MOD YBCO Coated Conductors, One with Exceptional Performance,"
T.G. Holesinger; S. Kim, D. Feldmann, D. Larbalestier, D. Verebelyi,
Abstract for the MRS 2003 Fall Meeting, Boston, MA, Dec. 1-5, 2003.

"Magneto-Optical Imaging of Flux Pinning Characteristics in YBCO Thick Films Grown by PLD and BaF_2 Ex-Situ Process,"
S.R. Foltyn, Q. Li, Z. Ye, M. Suenaga, Y. Zhu, W.D. Si,
Abstract for the MRS 2003 Fall Meeting, Boston, MA, Dec. 1-5, 2003.

"Continuous Preparation of IBAD-MgO Templates for YBCO Coated Conductor Applications,
S. Kreiskott, B.J. Gibbons, C. Sheehan, V. Matias,
Abstract for the MRS 2003 Fall Meeting, Boston, MA, Dec. 1-5, 2003.

"Continuous Preparation of Pulsed Laser Deposited Oxide Buffer Layers and YBCO for Coated Conductor Applications,"
B.J. Gibbons, S. Kreiskott, C. Sheehan, V. Matias,
Abstract for the MRS 2003 Fall Meeting, Boston, MA, Dec. 1-5, 2003.

"Phase Equilibria in the $SrO-CuO-TiO_2$ System: Application to High-Temperature Superconductors (HTS) via Chemical Solution Deposition (CSD),"
A. Ayala, T.G. Holesinger,
Abstract for the MRS 2003 Fall Meeting, Boston, MA, Dec. 1-5, 2003.

"Intrinsic and Materials Related Effects on the Thickness Dependence of J_c in YBCO Coated Conductors,"
T.G. Holesinger, P.N. Arendt, R. Feenstra, A. Gapud, D. Christen, E. Specht, L. Heatherly, A. Goyal, D. Feldmann, S. Kim, D. Larbalestier,
Abstract for the MRS 2003 Fall Meeting, Boston, MA, Dec. 1-5, 2003.

"Through-Thickness Superconducting and Normal State Transport Properties Revealed by Thinning of Thick Film *ex-situ* $Yba_2Cu_3O_{7-x}$,"
T.G. Holesinger, P.N. Arendt, D. Feldmann, S. Kim. D.C. Larbalestier, R. Feenstra,
Abstract for the MRS 2003 Fall Meeting, Boston, MA, Dec. 1-5, 2003.

"Chemical Routes to Increasing Low Field and High Field Pinning in Epitaxial $REBa_2Cu_3O_7$ Films,"
J. MacManus-Driscoll, S.R. Foltyn, Q.X. Jia, H. Wang, A. Serquis, L. Civale, B. Maiorov, D.E. Peterson,
Abstract for the MRS 2003 Fall Meeting, Boston, MA, Dec. 1-5, 2003.

4. Patent and License Activity (April 1988 to September 2003)

4a. Invention Disclosures and Patent Applications

Designation	Date	Subject	Submitted by
DOE S-91,761 S.N. 60/213,111 S.N. 09/867,842	Filed 6/21/00 Filed 5/29/01	Architecture for High Critical Current Superconducting Thick Films	Q.X. Jia S.R. Foltyn T.G. Holesinger
DOE S-94,668 S.N. 60/170,968 S.N. 09/616,570	Filed 12/15/99 Filed 7/14/00	Surface Control of Alloy Substrates and Methods of Manufacture Thereof	L.G Fritzmeier, Q. Li, M.W. Rupich, E. Thompson, E. Siegel, C. Thieme, S. Annavurapu, P.N. Arendt, S.R. Foltyn
DOE 94,720	7/13/00	Apparatus for Heating a Moving Tape	S. R. Foltyn, P.C. Dowden
DOE 94,734 S.N. 60/333,917 S.N. 10/113,475	Filed 11/21/01 Filed 3/28/02	Composition of Matter for Superconducting Composite Conductors and Manufacturing of Same	T.G. Holesinger, S.R. Foltyn, P.N. Arendt, J.R. Groves, Q.X Jia, A. Ayala
DOE S-97,725 S.N. 10/113,476	Filed 3/28/02	Buffer Layer on Metal Alloy Substrates for Superconducting Tapes	Q.X. Jia, S.R. Foltyn, P.N. Arendt, J.R. Groves
DOE S-97,787 S.N. 10/208,086	Filed 7/29/02	Dual Ion Beam Assisted Deposition of Biaxially Textured Template Layers	James Groves Paul N. Arendt
DOE S-97,795 S.N. 10/209,391	Filed 7/31/02	Multilayer Composites and Manufacture of Same	T.G. Holesinger, Q.X. Jia
DOE S-97,803 S.N. 10/161,132	Filed 5/29/02	Reduced AC Losses in HTS Coated Conductors	S.P. Ashworth
DOE S-99,943 S.N. 10/242,895	Filed 9/11/02	Buffer Layers on Metal Alloy Substrates for Superconducting Tapes	Q.X. Jia, S.R. Foltyn, P.N. Arendt, J.R. Groves
DOE S-99.947 **S.N. 10/456,639**	**Disclosed 9/10/02** **Filed 6/5/03**	**Processing of High Density MgB$_2$ Wires by Hot Isostatic Pressing**	**Y.T. Zhu, A. Serquis, D. Hammon, L. Civale, X.Z. Liao, F.M. Mueller, D.E. Peterson, V. Nesterenko, Y. Gu**
DOE S-99.952 **S.N. 10/624,350**	**Disclosed 9/16/02** **Filed 7/21/03**	**Use of High Current Density Electropolishing for the Preparation of Very Smooth Substrate Tapes for Coated Conductor Applications**	**S. Kreiskott, V. Matias, P.N. Arendt. S.R. Foltyn**
DOE S-100,536 **S.N. 10/624,348**	**Filed 7/21/03**	**Simplified Biaxially Textured Composite Substrates**	**James Groves, Paul Arendt, Stephen Foltyn, Sankar Sambasivan**
DOE S-100,550 **S.N. 10/321,156**	**Filed 12/17/02**	**Superconducting Structure**	**Chuhee Kwon, Quanxi Jia, Stephen R. Foltyn**

Designation	Date	Subject	Submitted by
DOE S-100,556 **S.N. 60/483,146**	**Filed 6/26/03**	**Underground Radio**	**David Reagor, Jose Vasquez-Dominquez**
DOE S-100,564 **S.N. 10/624,855**	**Filed 7/21/03**	**Buffer Layer for Thin Film Structures**	**Stephen Foltyn, Quanxi Jia, Paul Arendt, Haiyan Wang**
DOE S-100,569 **S.N. 10/359,808**	**Filed 2/7/03**	**Substrate Structure for Growth of Highly Oriented and/or Epitaxial Layers**	**Paul Arendt, Stephen Foltyn, James Groves, Quanxi Jia**
DOE S-100,586 **S.N. 10/387,952**	**Filed 3/13/03**	**High Temperature Superconducting Thick Films**	**Paul N. Arendt, Stephen R. Foltyn, James R. Groves, Terry G. Holesinger, Quanxi Jia**
DOE S-100,600	**Disclosed 4/8/03**	**Magnetic Infrasound Sensor**	**Frederick Mueller, Lawrence Bronisz, Holger Grube, David Nelson, Jonathon Mace**
DOE S-100,663	**Disclosed 9/5/03**	**Enhanced Pinning in Mixed RE-123 Films with Low Variance and Specific Ionic Radius**	**Judith Driscoll Stephen Foltyn**
DOE S-100,664	**Disclosed 9/5/03**	**Balanced Inductance Current Limiter**	**Stephen Ashworth**
DOE S-100,667	**Disclosed 9/5/03**	**Enhanced Pinning in YBCO Films with BaZrO3 Nanoparticles**	**Judith Driscoll Stephen Foltyn**

4b. Patents Granted

Designation	Date	Subject	Issued to	Status
DOE S-63,245 S.N. 07/041,950 US Pat.4,784,686	Filed 04/24/87 Issued 11/15/88	Synthesis of Ultrafine Powders by Microwave Heating	T.T. Meek H. Sheinberg R.D. Blake	Expired 05/15/00
DOE S-68,033 S.N. 07/454,607 US Pat. 5,008,622	Filed 12/21/89 Issued 04/16/91	Superconductive Imaging Surface Magnetometer	W.C. Overton, Jr D. van Hulsteyn E.R. Flynn	Expired 10/16/98
DOE S-68,041 S.N. 07/330,329 US Pat 5,006,672	Filed 03/29/89 Issued 04/09/91	Apparatus for Storing High Magnetic Fields Having Reduced Mechanical Forces and Reduced Magnetic Pollution	M.L. Prueitt F.M. Mueller J.L. Smith	Maint. Fee 3 paid 10/09/02

Designation	Date	Subject	Issued to	Status
DOE S-68,042 S.N. 07/276,188 US Pat 4,873,444	Filed 11/23/88 Issued 10/10/89	Detection of Surface Impurity Phases in HTS Using Thermally Stimulated Luminescence	D.W. Cooke M.S. Jahan	Expired 10/10/97
DOE S-68,086 S.N. 07/311,998 US Pat 4,992,696	Filed 02/17/89 Issued 02/12/91	Apparatus Having Reduced Mechanical Forces for Supporting High Magnetic Fields	M.L. Prueitt F.M. Mueller J.L. Smith	Maint. Fee 3 paid 08/12/02
DOE S-68,098 S.N. 07/324,264 US Pat 5,015,952	Filed 03/14/89 Issued 05/14/91	Apparatus for Characterizing Conductivity of Materials by Measuring the Effect of Induced Shielding Currents Therein	J.D. Doss	Expired 05/14/99
DOE S-71,082 S.N. 07/671,231 US Pat 5,102,863	Filed 03/19/91 Issued 04/07/92	Process for Producing Clad Superconducting Materials	R.B. Cass K.C. Ott D.E. Peterson	Expired 10/07/99
DOE S-71,084 S.N. 07/670,111 US Pat 5,134,360	Filed 03/15/91 Issued 07/28/92	Apparatus and Method for Critical Current Measurements	J.A. Martin R.C. Dye	Expired 01/28/00
DOE S-72,816 S.N. 07/690,725 US Pat 5,268,646	Filed 04/24/91 Issued 12/07/93	Apparatus & Method for Characterizing Conductivity of Materials	J.D. Doss	Maint. Fee 2 due 06/07/05
DOE S-72,851 S.N. 07/860,337 US Pat. 5,238,913	Filed 03/30/92 Issued 08/24/93	Superconducting Microcircuitry by the Microlithographic Patterning of Superconducting Compounds and Related Materials	N.V. Coppa	Expired 08/24/01
DOE S-72,861 S.N. 813,726 US Pat 5,262,394	Filed 12/27/91 Issued 11/16/93	Superconductive Compositions Including Cerium Oxide Layer	X.D. Wu R. Muenchausen	Maint. Fee due 05/16/05
DOE S-72,880 S.N. 07/774,748 US Pat 5,278,138	Filed 10/11/91 Issued 01/11/94	Aerosol Chemical Vapor Deposition of Metal Oxide Films	K.C. Ott T.T. Kodas	Maint. Fee due 07/11/05
DOE S-72,898 S.N. 814,355 US Pat 5,252,551	Filed 12/27/91 Issued 10/12/93	Superconductive Articles	X.D. Wu, R.E. Muenchausen	Maint. Fee due 04/12/05
DOE S-72,899 S.N. 813,727 US Pat 5,270,294	Filed 12/27/91 Issued 12/14/93	Free-Standing Superconductive Articles	X.D. Wu, R.E. Muenchausen	Maint. Fee due 06/14/05

Designation	Date	Subject	Issued to	Status
DOE S-75,023 S.N. 08/419,485 US. Pat 5,554,224	Filed 03/31/94 Issued 09/10/96	Substrate Heater for Thin Film Deposition	S.R. Foltyn	Maint. Fee due 03/10/04
DOE S-75,081 S.N. 08/067,911 US Pat 5,300,486	Filed 05/27/93 Issued 04/06/94	Synthesis of BiPbSrCaCuO Superconductor	W.L. Hults, K.A Kubat-Martin, K.V. Salazar, D.S. Phillips, D.E. Peterson	Maint. Fee due 10/05/05
DOE S-78,394 S.N. 08/419,485 US Pat. 5,569,641	Filed 04/10/95 Issued 10/29/96	Preparation of Superconducting Bi-2223 Wire	M.G. Smith J.O. Willis D.E. Peterson	Maint. Fee due 04/29/04
DOE S-80,400 S.N. 08/168,331 US Pat 5,434,128	Filed 12/17/93 Issued 07/18/95	Superconducting Wire	D.A. Korzekwa J.F. Bingert D.E. Peterson H. Sheinberg	Maint. Fee due 01/18/07
DOE S-82,620, S.N. 08/425,752 US Pat. 5,872,080	Filed 04/19/95 Issued 02/16/99	High Temperature Superconducting Thick Films	P.N. Arendt X.D. Wu S.R. Foltyn	Maint. Fee 1 due 08/16/06
DOE S-82,623 S.N. 08/608,069 US Pat. 5,958,842	Filed 02/28/96 Issued 09/28/99	Melt Processing of Superconductors Using Alumina	T.G. Holesinger	Maint. Fee 1 due 03/28/07
DOE S-82,633 US Pat. 5,726,848	Filed 05/8/96 Issued 3/10/98	Fault Current Limiter and Alternating Current Circuit Breaker	H.J. Boenig	Maint. Fee due 09/10/05
DOE S-84,942 S.N. 08/597,061 US Pat. 5,908,812	Filed 02/05/96 Issued 06/01/99	Structure for HTS Composite Conductors & Manufacture of Same	J.D. Cotton G.N. Riley	Maint. Fee due 12/01/06
DOE S-84,965 S.N. 08/865,827 US Pat.5,820,678	Filed 09/23/96 Issued 10/13/98	Solid Source MOCVD Delivery System	B.N. Hubert X.D. Wu	Maint. Fee due 04/13/06
DOE S-89,600 S.N. 60/074,717 S.N. 09/249,476	Filed 2/13/98 Filed 02/12/99 Issued 3/6/01	Compressive Annealing of BSCCO-2223 Superconductive Tapes	Y.T. Zhu, P.S. Baldonado, J.F. Bingert, T.G. Holesinger, D.E. Peterson	Maint. Fee due 3/06/04
DOE S-89,624 S.N. 08/942,038 US Pat. 6,428,635	Filed 10/1/97 Issued 8/6/02	Substrates for Superconductors	L.G. Fritzmeier, E. Thompson, E. Siegel, C. Thieme, R.D. Cameron, J.L. Smith, W.L. Hults	Maint. Fee due 8/6/05

Designation	Date	Subject	Issued to	Status
DOE S-89,678 **S.N. 09/152,813** **US Pat. 6,541,136**	**Filed 9/14/98** **Issued 4/1/03**	**Superconducting Structure**	**C. Kwon, Q.X. Jia, and S.R. Foltyn**	**Maint. Fee due 10/1/06**
DOE S-89,679 **S.N. 60/100,215** **S.N. 09/787,224** **US Pat. 6,602,588**	**Filed 9/14/98** **Filed 3/14/01** **Issued 8/5/03**	**Superconducting Structure Including Mixed Rare-Earth Barium Copper Oxide Compositions**	**C. Kwon, Q.X. Jia, S.R. Foltyn, J.L. Smith, W.L. Hults, E.J. Peterson**	**Maint. Fee due 2/5/07**
DOE S-91,736 S.N. 60/138,326 S.N. 09/615,640 US Pat. 6,451,742	Filed 06/09/99 Filed 7/13/00 Issued 9/17/02	High Temperature Superconducting Composite Conductor & Method for Manufacturing the Same	T.G. Holesinger and J.F. Bingert	Maint. Fee due 9/17/05
DOE S-91,748 S.N. 60/143,781 S.N. 09/615,640 US Pat. 6,452,375	Filed 7/13/99 Filed 7/13/00 Issued 9/17/02	Apparatus for Measurement of Critical Current in Superconductive Tapes	J. Y. Coulter R.F. DePaula	Maint. Fee due 9/17/05
DOE S-91,761 S.N. 60/213,111 S.N. 09/867,842 US Pat. 6,383,989	Filed 6/21/00 Filed 5/29/01 Issued 5/7/01	Architecture for High Critical Current Superconducting Thick Films	Q.X. Jia S.R. Foltyn T.G. Holesinger	Maint. Fee due 11/7/05
DOE 94,732 **S.N. 09/721,834** **US Pat. 6,624,993**	**Filed 11/22/00** **Issued 9/23/03**	**Adjustable Direct Current and Pulsed Fault Current Limiter**	**H.J. Boenig** **J.B. Schillig**	**Maint. Fee due 3/23/07**
DOE S-97,723 **S.N. 10/113,476** **US Pat. 6,124,122**	**Filed 5/30/01** **Issued 9/23/03**	**High Critical Current Superconducting Tapes**	**T G. Holesinger,** **Q.X. Jia** **S.R. Foltyn**	**Maint. Fee due 3/27/07**
DOE S-97,804 **S.N. 10/096,774** **US Pat. 6,511,943**	**Filed 3/13/02** **Issued 1/28/03**	**Synthesis of Magnesium Diboride by Magnesium Vapor Infiltration**	**A. Serquis, Y.T. Zhu, F.M. Mueller, D.E. Peterson, X.Z. Liao**	**Maint. Fee due**

4c. Licenses Granted

License Number	Date	Subject	Issued to
89-41-0000-1	12/28/88 (Terminated 11/94)	Apparatus for Characterizing Conductivity of Materials by Measuring the Effect of Induced Shielding Currents Therein	Lakeshore Cryotronics
99-C00510.1	11/11/98	Superconductive Article including Cerium Oxide Layer	DuPont Superconductivity
01-C01080.0	05/29/01	High Temperature Superconductor Material	IGC-SuperPower, LLC

| 01-C01081.0 | 05/29/01 | High Temperature Superconductor Material | IGC-SuperPower, LLC |
| 01-C01082.0 | 05/29/01 | Fault Current Limiter and Alternating Current Circuit Breaker Device | IGC-SuperPower, LLC |

5. Agreements in Progress (14 Active, all types)

5a. Superconductivity Pilot Center Agreements – Active
None

5b. CRADA Agreements - Active

Organization	Topic	PI	Funding,$K DOE	Funding,$K Partner	Dates
Oxford Superconducting Technology	Bi-2212 HTS Tapes	Smith Holesinger Holesinger	290 55 700	290 100 730	11/93 -11/96 10/97–10/98 5/99-10/05
3M Corporation	Coated Conductors	Peterson	960 720 400	1375 720 150	3/97-3/99 3/99-5/00 5/00-1/02
American Superconductor Corp.	Bi-2223 Wire Development	Holesinger	450	450	5/02-5/04
General Electric	HTS Generator	Waynert	860	860	4/02-4/04
DuPont	HGMS Magnetic Separation	Waynert	120 LANL 300 FI Dupont	200	6/02-6/04
Hyper Tech Research, Inc.	MgB$_2$ Wire Development	Mueller	400	400	9/02-9/04
IGC-SuperPower	**Coated Conductors**	**Foltyn Balachandran** **Foltyn**	**700, LANL 500, ANL** **1700**	**1300** **1700**	**1/00-1/03** **3/03-3/05**

5c. Funds In / Funds Out Agreements – Active
None

5d. Other Collaborations - Active

Organization	Topic	PI	Dates
ASC/ ANL/ ORNL/ U. Wisconsin/ (previously, NIST-Gaithersburg)	Bi-2223 Wire Development (Wire Development Group)	J. Willis Holesinger	11/91-11/00 11/00-
3M/ORNL/ Southwire / Stanford University	Coated Conductor Group	E. Peterson	3/97-

ASC/ ORNL/ LBNL/U. Wisconsin/ Stanford U./MIT/ Wright-Patterson AFB/ EPRI (previously, TCSUH)	Coated Conductor Development Group	J. Willis Holesinger	2/96-11/00-
Oak Ridge National Laboratory	HTS Information Exchange	D. Peterson	In Progress
Argonne National Laboratory	HTS Information Exchange	D. Peterson	In Progress
Sandia National Laboratories	HTS Information Exchange	D. Peterson	In Progress
Brookhaven National Lab.	HTS Information Exchange	D. Peterson	In Progress

6. Completed Agreements

6a. Superconductivity Pilot Center Agreements - Completed

Organization	Topic	PI	Funding,$K DOE	Funding,$K Partner	Dates
CPS Superconductor	Metal-Ceramic Interfaces	Mitchell	102.6	80.8	9/89 - 9/90
DuPont / Hewlett-Packard	HTS Electronic Components	Peterson	3777	7200	10/89 - 10/92
Space Industries, Inc.	Microgravity Processing	Peterson	205	247	4/90 - 4/91
Cryopower Associates	Improvement of Bulk HTS Materials	Maley Maley	45.2 199.4	60 485.9	Ph 1: 2/90 Ph 2: 1/92 1/94
HiTc Superconco	Optimizing Performance of HTS Cavities and Targets	Wu Wu	136.6 101.9	125 100	Ph 1: 9/89 Phase 2: 12/91
Ceracon, Inc	Bulk HTS Consolidation	Foltyn	237.5	300	Phase 1: 6/91
Nuclear Metals/ SNL/AT&T	HTS Co-extrusion	Wallace Bingert	239.2 239.2	760.5 285 NM 190 ATT	Ph 1: 8/90-8/93 Ph. 2: 10/93-10/96
The Boeing Company	Superconducting Electromagnetic Devices	Peterson	240	240	4/97 - 4/98
Power Superconduct-ing Devices, Inc	Development of HTS Fault Current Limiter	Peterson	250	250	7/96-7/98
American Superconductor Corporation	Bi-2223 Conductors HTS Composite Conductors	Peterson Peterson Willis Willis Willis Holesinger	170.5 587.1 1500 2300 1800	179 350 950 1100 1800	Ph 1: 6/89-Ph 2: 11/91-Ph 3: 2/94-Ph 4: 3/96-Ph.5: 7/98-3/01

6b. CRADA Agreements - Completed

Organization	Topic	PI	Funding,$K DOE	Funding,$K Partner	Dates
Lockheed Martin	Coil Development	Peterson	330	210	7/93 - 7/96
Plastronic, Inc.	Liquid Cryogen Free HTS Magnet System	Daugherty	100 +33k funds in	67	6/95 - 5/96
The BOC Group, Inc.	Superconducting Coated Materials	Peterson	70	70	2/23/96-11/22/96
EURUS Technologies, Inc.	Development of HTS Current Leads & Solders	Peterson	80	140	2/6/96-2/5/97
Eriez Magnetics	HTS Magnetic Separation	Daugherty	70	52	4/2/96-4/1/97
Lockheed Martin	HTS Current Limiter	Peterson	400	400	11/95-10/97
Lockheed Martin	Bridge-Type Fault Current Limiter	Boenig	700	1400	11/95-9/98
General Atomics (assumed LM activity)	Bridge-Type Fault Current Limiter	Peterson	Remainder of 700 from above	Remainder of 1400 from above	9/98-5/99, 5/99-11/99
Astronautics Corp. of America	Active HTS Magnetic Refrigerator	Peterson	200	200	4/98-7/00
ABB Power T&D Co., Inc.	HTS Transformer	Maley	95	70	7/99-7/00

6c. Funds In / Funds Out Agreements - Completed

Organization	Topic	PI	Type	Value $K	Dates
Superconductor Technologies, Inc.	Rutherford Backscattering	Maggiore	Funds In	1.0	5/88 - 5/89
Public Service Co. of New Mexico	HTS Theory	Parkin	Funds In	357.1	6/88 - 6/90
EPRI	Assessments for Utilities	Newkirk	Funds In	99.8	6/88 - 6/89
AMP, Inc.	RF Characterization of TI-Based HTS Films	Wallace	Funds In	102.9	1/89 - 5/89
EPRI	Heat Pipe Switch	Merrigan	Funds In	150	1/89 - 1/90
Univ. Missouri, Rolla	HTSC Fibers	Maestas	Funds Out	111	1/89 - 1/90

Bechtel	SMES Systems/ Hot-to-Cold Transitions	Maestas	Funds Out	10	2/89 - 2/90
Rocketdyne Corp., Rockwell, Intl.	Synthesis of Tl HTS	Peterson	Funds Out	95.3	5/89 - 5/90
EPRI	New Families of HTS	Smith	Funds In	120	2/90 - 2/92
Underground Systems	Transmission Systems	Stewart	Funds In	48	5/91 - 5/92
W.J. Schafer Assoc.	SMES Assessment	Peterson	Funds Out	89.9	5/92 - 5/93
Univ. Calif.-San Diego	Hydrocode Models	Peterson	Funds Out	63 57	12/92 -12/93 6/94 - 5/95
Intermagnetics General Corporation	Tl-Based HTS Coils	Peterson	Funds Out	400	10/92 - 10/96
MIT	Bitter Magnets	Peterson	Funds In	50	5/93 - 4/96
Midwest Super-conductivity, Inc.	IBAD-Coated Flexible Substrates	Peterson	SBI Tech Consulting Agreement	5	3/95 - 3/96
EPRI	Ac Loss Measurements in HTS Cables	Maley	Funds In	150	9/5/95- 9/4/96
EPRI	Thick Films on Flexible Substrates	Wu	Funds In	25 200	7/95-9/95 10/95-10/96
Pirelli Cable & Systems	Ac Losses on HTS Cables	Peterson Willis	Funds In	55 63	11/97 – 6/98 1/99 – 9/99

6d. Other Collaborations - Completed

Organization	Topic	PI	Dates
Tektronix, Inc.	Cryogenic Materials Characterization	J. Smith	11/89-5/94